7-26-2021

Regional Characteristics and Variability of Extreme Precipitation and Atmospheric Rivers in Past, Present, and Future Climates Over the Contiguous United States

Emily Anne Slinskey
Portland State University

Recommended Citation
Slinskey, Emily Anne, "Regional Characteristics and Variability of Extreme Precipitation and Atmospheric Rivers in Past, Present, and Future Climates Over the Contiguous United States" (2021). *Dissertations and Theses.* Paper 5760.
https://doi.org/10.15760/etd.7631

Regional Characteristics and Variability of Extreme Precipitation and Atmospheric Rivers in Past, Present, and Future Climates over the Contiguous United States

by

Emily Anne Slinskey

A dissertation submitted in partial fulfillment of the
requirements for the degree of

Doctor of Philosophy
in
Earth, Environment and Society

Dissertation Committee:
Paul Loikith, Chair
Andrew Martin
Kelly Gleason
Duane Waliser
Andrew Rice

Portland State University
2021

Abstract

This dissertation examines the regional and seasonal variability of extreme precipitation and atmospheric rivers (ARs) across the contiguous United States (CONUS) in past, present, and future climates. An extreme precipitation categorization scheme, designed to monitor and track the multi-scale variability of extreme precipitation, is applied to a range of precipitation measurement products as an assessment of observational uncertainty. To investigate the importance of ARs across the CONUS, an objective AR identification algorithm is applied to global reanalysis to identify and characterize AR characteristics regionally over the observational record. Projected change in AR day frequency, geometry, intensity, and associated precipitation is quantified in Phase 6 of the Coupled Model Intercomparison Project (CMIP6) under the Shared Socioeconomic Pathway 585 (SSP 585) high-end emissions warming scenario.

Extreme precipitation most commonly occurs across the mountains of the western US in the winter and over the southeastern US in the summer and fall, associated with ARs and tropical systems, respectively. Observational uncertainty assessment results reveal historical precipitation measurement approaches, including in situ, satellite-derived, gridded in situ, and reanalysis, capture the principal spatial patterns of extreme precipitation climatology, with considerable variability in event frequency, spatial extent, and magnitude. Higher native resolution products most closely resemble in-situ observations, capturing a greater frequency of high-end multi-day totals relative to lower resolution products, even after rescaling, implying a systematic resolution-related bias.

Within the observational record, ARs are most frequent in the fall and winter in the West, spring in the Great Plains, and fall in the Midwest and Northeast, showing regional and seasonal variability in basic geometry and IVT. Linked AR precipitation characteristics suggest that a substantial proportion of extreme events are associated with ARs over many parts of the CONUS, including the eastern US, characterized by seasonally-varying moisture transport patterns and lifting mechanisms. Analysis of change between five CMIP6 model historical simulations and future projections, under the SSP585 warming scenario, suggests notable increases in AR day frequency, intensity, and geometry by the end of the 21st century (2071-2100). Projections indicate ARs will comprise a greater share of the total climatological precipitation that falls CONUS-wide, as well as an increasing percentage of the occurrence of the top 5% of multi-day extremes.

The findings from this dissertation aim to identify and quantify uncertainty in the regional-scale variability of extreme precipitation and associated meteorological mechanisms among observations and global climate model projections. Future climate change impacts studies require an improved dynamical and physical process-based understanding of extreme precipitation. Results from this dissertation can further support future investigation into the spatiotemporal variability of the underlying synoptic scale weather patterns (i.e., meteorological characteristics and dynamical processes) associated with enhanced precipitation formation during an AR.

Acknowledgements

This work would not have been possible without the insight, guidance, and encouragement of my advisor, Dr. Paul Loikith. As a mentor and friend, Dr. Loikith has been instrumental in my growth and success as a scientist. His ceaseless support for his students and devotion to science will have an everlasting effect on my career.

I would like to thank Dr. Andrew Martin for his patience, support, and overall involvement in my education and research aspirations. I would also like to thank Dr. Duane Waliser for his mentorship, ability to always make time to help and support my work, as well as provide me with the most incredible opportunities. My time as a JPL intern was a defining moment in my graduate education and has greatly influenced my career goals.

I would also like to thank the remaining members of my committee, including Dr. Kelly Gleason and Dr. Andrew Rice, for their commitment and guidance throughout my PhD. Thank you to the members of the RCMES group, past and present, for your feedback, collaboration, and contributions, which have greatly improved the quality of my work. I would like to especially thank Alex Goodman for collecting and processing data used in all the analyses in this dissertation. Thank you Dr. Kyo Lee and Dr. Bin Guan for your help and support.

A tremendous thanks to the members, past and present, of the PSU Climate Science Lab for your friendship and moral support. I would also like thank the Geography Department faculty and staff for their guidance and service toward making this achievement possible.

Finally, I owe an immense amount of gratitude to my family, for their support and unwavering confidence in me. Thank you, Zachary Kane-Seitz, for your patience, kindness, and unyielding support from the beginning, you were indispensable to this achievement. I am also deeply grateful for the support of my parents. They have instilled in me a desire to learn and persevere, without which this work would not have been possible.

This work was carried out, in part, at the Jet Propulsion Laboratory, California Institute of Technology and at Portland State University, under a contract from National Aeronautics and Space Administration (NASA). Support for this project was provided by the NASA Indicators for the National Climate Assessment (NCA) Program. Partial support was also provided by a JPL student summer internship.

Table of Contents

List of Tables

List of Figures

Chapter 1: Introduction

1.1 Motivation

According to the United States (US) Fourth National Climate Assessment (NCA) Climate Science Special Report (CSSR; USGCRP 2017), and references therein, an increase in the intensity and frequency of heavy precipitation is evident over many regions of the contiguous United States (CONUS; Easterling et al. 2017), especially over the last several decades. This report further states with 'high confidence' that increases in heavy precipitation are projected to continue with regional-scale variability in the sign and magnitude of projected change (Janssen et al. 2014, 2016). Given the severity of extreme precipitation impacts (e.g., flooding, landslides, debris flows) and the associated importance to both human and natural systems (e.g., life, property, ecosystems), realizing potential variability and change at local through regional scales under warming is critical.

A growing body of evidence, informed by both the observed record and future projections, attribute increases in the atmosphere's water holding capacity with warming, governed by the Clausius-Clapeyron relationship, as the primary cause of intensification within the hydrologic cycle (e.g., Wehner et al. 2013; Kunkel et al. 2013a, 2013b). However, due to the complex nature and diverse interacting drivers of extreme precipitation (e.g., extratropical cyclones, tropical cyclones, mesoscale convective systems, the North American monsoon system; Kunkel et al. 2012), change is not uniform in space and varies by region (Tabari et al. 2019). Constraining uncertainty surrounding changes in extreme precipitation requires an improved understanding of the

driving meteorological mechanisms and processes as opposed to the associated statistics alone.

The World Climate Research Programme (WCRP) has identified "Weather and Climate Extremes" as one of seven Grand Challenges[1] representing areas of emphasis in scientific research. Two key questions are raised as essential to addressing this challenge, specifically regarding the sufficiency of observations for studying extremes, as well as the roles of local through synoptic scale processes in the formation of extremes. Towards this end, the recurrent theme of this dissertation is to provide a thorough assessment of regional variability in extreme precipitation and associated meteorological mechanisms across the CONUS among observations and future projections. As a basis for understanding extreme precipitation distribution and variability across the CONUS, in *Chapter 2* an extreme precipitation categorization scheme is developed and applied to a suite of diverse precipitation measurement products as a measure of observational uncertainty. As the dominant meteorological mechanism for producing precipitation across the West, a systematic and uniform investigation of atmospheric river (AR) characteristics and impacts is carried out for all regions across the CONUS in past, present, and future climates. As a benchmark for future change, *Chapter 3* presents a robust observational assessment of AR occurrence, geometry, magnitude, and associated precipitation across seasons and regions over the CONUS. Projected change in AR characteristics and impacts is subsequently quantified in *Chapter 4*, based on a detailed

[1] https://www.wcrp-climate.org/component/content/article/63-gc-extremes?catid=32&Itemid=266

comparison between the historical simulation and future projections of five global climate models (GCMs) from the Coupled Model Intercomparison Project Phase 6 (CMIP6) database. *Chapter 5* summarizes each chapter's key findings and implications for future work surrounding an improved dynamical and physical process-based understanding of extreme precipitation formation in ARs.

While some of the findings documented here complement existing research, the combination of each individual chapter within this dissertation serves to provide a more holistic and complete understanding of the regional and seasonal variability of extreme precipitation and AR characteristics and co-occurrence across the CONUS in past, present, and future climates. As a contribution to the continuing efforts of the NCA, all chapters provide intuitive and interpretable results at regionally-relevant scales, computed at each grid point as well as summarized over the seven NCA regions across the CONUS. This chapter serves to summarize and identify gaps in the relevant scientific literature as well as outline the recurring theme, individual aims, and structure of this dissertation.

1.2 Background

1.2.1 Extreme Precipitation: Climate Change, Mechanisms, and Monitoring

A number of studies have documented a significant increase in the frequency and intensity of extreme precipitation events across the CONUS (e.g., Karl et al. 1996; Karl and Knight 1998; Groisman et al. 2004, 2005, 2012, Kunkel et al., 2003, 2007;

Alexander et al. 2006). Occurring when the air is nearly completely saturated, projections of extreme precipitation intensification across the globe are strongly linked to increases in atmospheric water vapor with warming at the rate of Clausius-Clapeyron (CC) scaling. The CC relationship states that, given constant relative humidity, the water holding capacity of the atmosphere will increase exponentially with temperature T at a rate of ~7% per degree Celsius of warming, yielding

$$\frac{de_s}{dT} = \frac{L_v\, e_s}{R_v\, T^2} \tag{1}$$

where e_s is saturation vapor pressure, L_v is the latent heat of vaporization, and R_v the gas constant of water vapor (Bolton 1980; Iribarne and Godson 1981).

Reasoning around CC scaling is strongest at higher latitudes where air tends to be closer to saturation, and relative humidity is roughly constant through seasonal changes in temperature (Allen and Ingram 2002), suggesting the response may be different at lower latitudes. While CC scaling has been widely used to explain the intensification of extreme precipitation across the mid-latitudes (e.g., Frich et al. 2002; Christensen and Christensen 2003; Sherwood et al. 2010; Donat et al. 2016; Lu et al. 2018; Nayak et al. 208; Giorgi et al. 2019; Morrison et al. 2019; Oh et al. 2020 Sousa et al. 2020), rates of change are expected to vary regionally (Ivancic and Shaw 2016). At local to regional scales, departures from the CC relationship, so called super-CC scaling (greater than 7%) and sub-CC scaling (less than 7%), can be consequences of different factors (e.g.,

moisture availability, type of precipitation, annual cycle, percentile of precipitation intensity, and regional weather patterns). Across the CONUS, several studies have documented super-CC rates across the East (Lepore et al. 2014), including across the interior of New York (Shaw et al. 2011), with the largest rates found in the North Central US (Mishra et al. 2012; Lepore et al. 2014). While in the West, sub-CC conditions have been identified as a result of regionally variable threshold temperatures due to seasonal moisture availability (i.e., wet winters and dry summers; Ivancic and Shaw 2016). The applicability of the CC equation to extreme precipitation intensity assumes that fully saturated atmospheric conditions are attainable with some regularity across a given temperature range, however this is not necessarily the case for all regions across the CONUS.

Given CC scaling will affect precipitation asymmetrically across the CONUS, uncertainty in the changing distribution and character of precipitation extremes is further driven by a wide range of associated regionally variable mechanisms and processes. While all extremes share some environmental commonalities, such as anomalous moisture availability and a lifting mechanism, the meso- through synoptic scale patterns and conditions vary regionally with strong seasonality and inter-annual variability. Tropical cyclones and hurricanes have generated extensive, devastating and costly impacts across the Southeast. Extratropical cyclones (ETC's), often associated with other key mechanisms, including ARs (Dacre et al. 2015) and warm/cold fronts (Catto and Pfahl 2013), are a major contributor to cool season extreme precipitation events across

the West (Kunkel et al. 2012). Summertime convection and intense winter storms drive heavy precipitation events seasonally in the Northeast (Howarth et al. 2019). Thunderstorms in the summer are a common mechanism for extremes characterized by localized, heavy and impactful storm totals across the central and southern Great Plains. Meso-scale convective systems (MCS's) have been identified as responsible for between 30 and 70% of warm season rainfall in a region spanning the Rocky Mountains to the Mississippi River (Fritsch et al. 1986). This radically different meteorological realization of extreme events across the CONUS requires monitoring at fine spatiotemporal scales capable of capturing this regional variability and its potential for change under warming.

Indices for extreme precipitation have been developed and applied in multiple studies using a diverse set of datasets and methods (Zhang et al. 2011 and references therein). Specific to the US, precipitation extremes have been monitored using the US Climate Extremes Index (Gleason et al. 2008). Values and trends are available at CONUS and broad regional scales but not at local or sub-regional (e.g., state, water district, mountain range etc.) scales. Additionally, the US Environmental Protection Agency has a heavy precipitation climate indicator, which records the fraction of land area over the CONUS experiencing heavy precipitation in a given year. While concise and intuitive, these current approaches to climate monitoring are limited in their ability to provide information at impacts-relevant scales meaningful for stakeholders. With the potential for change in the frequency and intensity of highly regionalized phenomena (i.e., ARs or

tropical cyclones) associated with extreme precipitation under warming, the ability of monitoring efforts to discern changes at local through regional scales is imperative.

1.2.2 Atmospheric Rivers: Definition, Impacts, and Climate Change

Among a number of storm types, including tropical systems, severe convective storms, and winter storms, ARs were highlighted for the first time as a key topic of the Fourth NCA CSSR's chapter on "Extreme Storms." The report states with 'medium confidence' that the frequency and severity of landfalling ARs on the US West Coast will increase as a result of increasing evaporation and resulting higher atmospheric water vapor content that occurs with increasing temperature (i.e., CC relationship described above, Eq.1).

ARs are long, narrow filamentary corridors of strong horizontal water vapor transport (Zhu and Newell 1998) associated with important hydrometeorological impacts. Operating as one part of a larger, synoptic scale dynamical system, ARs are generally found in the warm sector of an ETC associated with a low-level jet (LLJ) ahead of the cold front (Ralph et al. 2004, 2005, 2006; Zhang et al. 2018). While only covering ~10% of Earth's zonal circumference, ARs are responsible for >90% of the total poleward water vapor transport in the midlatitudes (Zhu and Newell 1994, 1998). Given the intense transport of warm, moist air, ARs comprise the ideal conditions for forced precipitation through their interaction with a suitable lifting mechanism (e.g., orographic, frontal, convective, dynamic), fueling extreme precipitation and flooding events (Dettinger 2011).

As important features within the global hydrologic cycle, both the abundance and absence of ARs have major societal and environmental impacts (Ralph et al. 2019). In water-stressed regions, such as the western US, ARs provide a crucial source of freshwater through rain and snowfall at higher elevations (Guan et al. 2010; Dettinger et al. 2011) with the potential to mitigate drought conditions (Dettinger 2013). In this region, ARs are responsible for up to 30-50% of annual precipitation and water resources (Dettinger et al. 2011; Guan et al. 2010; Lavers and Villarini 2015; Ralph et al. 2013). On the other hand, the extreme precipitation (Ralph and Dettinger 2012) and high winds (Waliser and Guan 2017) often associated with ARs can lead to devastating floods and costly damages (Ralph and Dettinger 2011; Ralph et al. 2012; Corringham et al. 2019).

The most defining feature of an AR, and most related to the precipitation-generating mechanism, is their intense water vapor transport. AR intensity is measured by column-integrated water vapor transport (IVT),

$$IVT = \frac{1}{g}\sqrt{\left(\int_{p_s}^{p_t} qudp\right)^2 + \left(\int_{p_s}^{p_t} qvdp\right)^2} \tag{2}$$

where g is standard gravity, u and v zonal and meridional wind, respectively, q specific humidity, p_s surface pressure, and p_t an upper-atmospheric reference pressure (typically between 500 and 200 hPa; Newell 1992). The equation (Eq. 2) integrates a combined

measure of moisture and wind, or moisture flux, over a column in the atmosphere. For simplicity, IVT can be defined as the magnitude of water vapor transport and can further be separated into distinct contributions from thermodynamics (i.e., atmospheric moisture content q) and dynamics (i.e., atmospheric motion or wind u and v). The change in the thermodynamic component of IVT can be understood through the CC equation (Eq. 1) described above. Increases in the moisture component of IVT are expected to meet super-CC scaling (Gao et al. 2015), while the contribution from changes in winds is hardly detectable (Lavers et al. 2013).

In the US, the majority of AR research has focused on the West (see Ralph et al. 2020 and references therein), largely driven by water availability concerns and potential risk from associated hydrometeorological impacts. In California, landfalling ARs explain a large proportion of annual precipitation (Guan et al. 2010; Dettinger et al. 2011) and are associated with a majority of precipitation extremes (Ralph et al. 2004; Ralph and Dettinger 2012) and flooding across the region (Ralph et al. 2006, 2013). Destructive flooding due to extreme streamflow and prolonged heavy rainfall under AR conditions has also been documented over parts of Oregon and Washington (Neiman et al. 2008b, 2011; Ralph et al. 2011; Warner et al. 2012; Collow et al. 2020). Furthermore, in a study extending to British Columbia, Neiman et al. (2008a) identified ARs as modulators of the region's climate, yielding important hydrologic consequences, including increased precipitation, flows, vapor fluxes, and changes in snow water equivalence.

Considerably less attention has focused on the role of ARs in regions across the central and eastern US, however, evidence suggests that some heavy precipitation and high-impact flood events have been associated with the presence of AR-like conditions. For example, Moore et al. (2012) and Lackmann et al. (2013) linked an AR to catastrophic flooding in Tennessee and Kentucky in May 2010. Rabinowitz et al. (2018) found 15 AR events between 2010-2015 contributed to 67% of the total monthly precipitation in Mississippi River Valley. These case studies are further supported by research linking AR-like features to strong synoptic scale weather systems across the southeastern US (e.g., Pfahl et al. 2014; Mahoney et al. 2016; Debbage et al. 2017; Miller et al. 2018). Across the Midwest, ARs feeding moisture into regions of deep convection contributed to the May/June floods of 2008 (Budikova et al. 2010; Dirmeyer and Kinter 2009; Smith et al. 2013). Nakamura et al. (2013) further presents evidence of AR conditions governed by an anomalous semi-stationary ridge off the US East Coast leading to flooding in the Ohio River Basin. Concurrently, Lavers and Villarini et al. (2013), identified ARs as a major flooding agent over the central US through associated seasonal composites of average mean sea level pressure anomalies. Although not recognized as ARs, several studies have further noted the role of anomalous water vapor fluxes and 'tropical moisture feeds' as drivers of extreme precipitation over parts of the Northeast (Howarth et al. 2019; Teale and Robinson 2020).

The importance of ARs in weather and climate has further motivated a number of climate change studies (Waliser and Rutz 2020), focused mainly on the west coast of North

America (e.g., Dettinger 2011; Pierce et al. 2013; Gao et al. 2015; Payne and Magnusdottir 2015; Radić et al. 2015; Warner et al. 2015; Hagos et al. 2016; Shields and Kiehl 2016a, 2016b) and Europe (Gao et al. 2016; Lavers et al. 2013; Ramos et al. 2016; Shields and Kiehl 2016a). Research suggests that AR day frequency, geometry, IVT magnitude, seasonality, and associated flood risk may change under future simulations of climate. Augmenting the studies above, Espinoza et al. (2018) performed a global study investigating climate change projection effects on ARs using CMIP5. Results show a 50% increase in AR day frequency, with a total decrease in the number of individual AR events globally, alongside a 25% increase in AR length, width, and strength across North America. Along the US West Coast, changes in ARs are predominantly driven by increases in atmospheric water vapor due to warming. Warner et al. (2014) projects an increase of 290% in historical 99th percentile IVT days by the end of the century, consistent with projected increases identified elsewhere (Radić et al. 2015; Shields and Kiehl 2016a).

While an increase in global mean precipitation is expected under warming, the response of ARs as it contributes to this change is still uncertain. Investigations of projected impacts specific to ARs are scarce but in general the moistening of the atmosphere and thermodynamic response of IVT to warming is expected to increase AR precipitation overall (Lavers et al. 2013; Gao et al. 2015, 2016; Payne et al. 2020). However, it's important to note that while future ARs will contain more moisture, changes in atmospheric circulation (Hu et al. 2017) and precipitation efficiency (Siler and Roe

2014), among others, will likely play a role in potential change in the amount and distribution of AR precipitation in the future. Together with a limited understanding of observed change, a high degree of uncertainty remains around regional changes in AR characteristics and impacts under warming outside of the western coastlines of North America and Europe (Payne et al. 2020). The multiple roles ARs play in the climate system and the complexity of their impacts motivate the importance of a uniform holistic approach across regions CONUS-wide.

1.3 Structure of the Dissertation

The overarching theme of this dissertation is to improve our understanding of extreme precipitation and AR variability, over both the observational record and among climate model projections, with regional specificity across the CONUS. This is explored across the seasonal cycle using a broad array of data types, including in-situ, gridded in-situ, reanalysis, satellite-derived, and climate model output. A wide range of metrics are used to improve our understanding of precipitation extremes and ARs independently as well as collectively. Results are consistently presented at each grid-point as well as summarized across regions for an intuitive, yet thorough, understanding of local to regional-scale variability. Each chapter has specific objectives that contribute to overarching theme of this dissertation, as outlined below.

In *Chapter 2*, an extreme precipitation categorization scheme is developed and applied to a range of precipitation measurement products. The approach, which assigns extreme

precipitation categories, based on three-day storm totals, at each data point (i.e., grid point or gauge station), is designed to be intuitive and easily interpretable, informing on variability and change at impacts-relevant scales. The usefulness and utility of this monitoring scheme is further demonstrated through its application as the basis for a dataset intercomparison to assess observational uncertainty across a wide range of historical precipitation measurement approaches. Differences, similarities, and apparent limitations among datasets are identified using a number of metrics and summary statistics important for understanding regional changes in extreme precipitation frequency and magnitude. Regional variability in the categorized extreme precipitation climatology is also summarized and discussed relative to likely attributable meteorological mechanisms and storm types.

Chapter 3 investigates the role of ARs uniformly across the CONUS over the observational record. An objective AR detection algorithm is applied to global reanalysis to characterize AR day frequency, geometry, and intensity. The seasonal distribution of preferred AR moisture pathways is identified to distinguish canonical AR characteristics in each region. Identified ARs are further linked with multi-day precipitation totals, as described in *Chapter 2*, using high resolution gridded in-situ precipitation measurements to assess regional variability in AR-driven climatological precipitation and extremes. Aggregate measures of AR characteristics are summarized regionally, as well as at each grid point, to illustrate the geospatial climatology.

In *Chapter 4*, the objective AR detection algorithm applied in *Chapter 3* is used to quantify change in ARs between CMIP6 historical simulations and future projections under the high-end warming scenario, SSP585. The algorithm uses a relative threshold consistent for the current and future climate to characterize projected climate change impacts on AR day frequency, geometry, intensity, and associated precipitation. Multi-day total precipitation extremes are identified based on future thresholding and linked with detected ARs to assess change in their co-occurrence. Results are presented as the multi-model mean and computed for the historical simulation, mid and end-of-century projections, and difference at each grid point as well as aggregated across regions. Individual model distributions of several important AR characteristics are also shown to evaluate inter-model similarities and differences.

Finally, the main findings and conclusions of this dissertation are summarized in *Chapter 5*. Implications of results and avenues for future work relating to this field of research are considered and discussed.

Chapters 2 and *3* are based on published peer-reviewed articles in the Journal of Hydrometeorology. These chapters are presented as they are published with some minor changes to formatting.

Chapter 2: An Extreme Precipitation Categorization Scheme and its Observational Uncertainty over the Continental United States

This chapter is published as: Slinskey, E. A., P. C. Loikith, D. E. Waliser, and A. Goodman, 2019: An Extreme Precipitation Categorization Scheme and its Observational Uncertainty over the Continental United States, *Journal of Hydrometeorology*, **20**(6), 1029-1052, https://doi.org/10.1175/JHM-D-18-0148.1.

Abstract

An extreme precipitation categorization scheme, used to temporally and spatially visualize and track the multi-scale variability of extreme precipitation climatology, is applied over the Continental United States. The scheme groups three-day precipitation totals exceeding 100 mm into one of five precipitation categories, or "P-Cats". To demonstrate the categorization scheme and assess its observational uncertainty across a range of precipitation measurement approaches, we compare the climatology of P-Cats defined using in situ station data from the Global Historical Climatology Network-Daily (GHCN-D), satellite derived data from the Tropical Rainfall Measuring Mission (TRMM), gridded station data from the Parameter-elevation Regression on Independent Slopes Model (PRISM), global reanalysis from the Modern-Era Retrospective Analysis for Research and Applications, version 2, and regional reanalysis from the North American Regional Reanalysis. While all datasets capture the principal spatial patterns of P-Cat climatology, results show considerable variability across the suite in frequency, spatial extent, and magnitude. Higher resolution datasets, PRISM and TRMM, most

closely resemble GHCN-D and capture a greater frequency of high-end P-Cats relative to the lower resolution products. When all datasets are rescaled to a common coarser grid, differences persist with datasets originally constructed at a high resolution maintaining a higher frequency and magnitude of P-Cats. Results imply that dataset choice matters when applying the P-Cat scheme to track extreme precipitation over space and time. Potential future applications of the P-Cat scheme include providing a target for climate model evaluation and a basis for characterizing future change in extreme precipitation as projected by climate model simulations.

2.1 Introduction

Extreme precipitation is associated with a multitude of societal and environmental impacts across the United States (US). Often accompanying severe weather events, including hurricanes, snowstorms, and atmospheric rivers, these meteorological phenomena pose threat to property, agriculture, infrastructure, and human life while also playing a key role in the water budget (Kunkel et al. 2013). According to the 2017 National Climate Assessment (NCA) Climate Science Special Report, climate change is projected to alter the frequency, severity, and seasonality of extreme precipitation across the US (Easterling et al. 2017). Climate change mitigation policies and adaption initiatives are greatly influenced by societal vulnerabilities to climate impacts like those associated with extreme precipitation. Therefore, a comprehensive understanding and intuitive way to track and project change across space and time at impacts-relevant scales is critical.

Climate model projections of future change in global precipitation generally follow the Clausius-Clapeyron relationship projecting the atmosphere's water holding capacity to increase exponentially with temperature at roughly 7% per degree Celsius warming (Allen and Ingram 2002; Trenberth et al. 2003; and Pall et al. 2007). Consistent with these expectations, a number of studies have suggested that anthropogenic climate warming may be attributable to an increase in the probability and severity of recent notable heavy precipitation events over the US such as September 2013 in Colorado (Pall et al. 2017), the rainfall from Hurricane Harvey (Risser et al. 2017), and the August 2016 Louisiana event (Wang et al. 2016). However, the sign and magnitude of observed changes in extreme precipitation are not always immediately apparent from observational analysis at local through regional scales. This is due in part to the character of extreme precipitation varying considerably over space and time, making it difficult to detect an anthropogenic signal above natural variability (Easterling et al. 2000; O'Gorman and Schneider et al. 2009). Furthermore, understanding observed and projected changes in the frequency and intensity of key mechanisms associated with extreme precipitation, such as tropical cyclones and atmospheric rivers, is still an area of active research (e.g., Knight and Davis 2009; Prat and Nelson 2013; Gao et al. 2015; Behrangi et al. 2016; Mahoney et al. 2016; Lamjiri et al. 2017).

Several extreme precipitation indices have been developed and applied to a diverse set of datasets using a range of methods to examine changes in extreme precipitation over space

and time (Zhang et al. 2011 and references therein). One example is a set of extreme indices developed by the Expert Team on Climate Change Detection and Indices as part of the World Climate Research Programme Project on Climate Variability and Predictability, known as the "ETCCDI" (Frich et al. 2002, Alexander et al. 2006). These indices are designed to address a broad range of global climate information needs ranging from the frequency of precipitation threshold exceedances to the maximum length of wet spells. Specific to the US, precipitation extremes have been monitored using the US Climate Extremes Index (Gleason et al. 2008) in addition to the US Environmental Protection Agency's climate indicator for annual heavy precipitation aggregated over the conterminous United States (CONUS; US EPA 2016). While concise and useful, these monitoring approaches provide a great deal of climate information at broad global and national scales, but less information at local to regional scales. The regional variability in extreme precipitation can be large across a single climate region (e.g., the Northwest or Southeast), therefore it is important that monitoring addresses the need for regional relevance while also providing a similarly high level of intuitive interpretability.

The ability to detect, analyze, and track changes in extreme precipitation is also heavily dependent on the reliability of observations and a number of precipitation climatology and dataset intercomparison studies have been conducted at global and regional scales highlighting these differences (e.g., Adler et al. 2001; Guirguis and Avissar 2008 respectively). In situ station data is commonly accepted as a primary source and often used as a reference relative to other products. However, station observations are spatially

heterogeneous and may be temporally inconsistent, creating observational gaps (Kidd et al. 2017). Satellite-based precipitation measurements, on the other hand, are spatially seamless regardless of in situ gauge density or quality, however these datasets exhibit bias resulting from instrumental and algorithmic error (Sapiano and Arkin 2009; Chen et al. 2013; Behrangi et al. 2014a; Tan et al. 2016). Similarly, bias can be introduced to analysis products through data assimilation and model errors (Bukovsky and Karoly 2007; Bosilovich et al. 2008; Reichle et al. 2017), to gridded in situ products through spatial interpolation (Daly 2006), and simply from spatial resolution (Herold et al. 2017). Additionally, the high spatial and temporal variability characterizing precipitation extremes has been shown to result in exceedingly low agreement among a range of global precipitation measurement products (Donat et al. 2013). Because the dataset one uses has been shown to matter, it is critical to understand and, where possible, constrain observational uncertainty when monitoring and tracking precipitation extremes.

Here we present a climatology of an extreme precipitation categorization scheme as an intuitive way to interpret extreme precipitation climatology, variability, and change over space and time and evaluate its observational uncertainty across a range of datasets. The application of this scheme is motivated by the need for an intuitive, pointwise climate indicator for extreme precipitation that can be provided clearly at scales relevant to societal and environmental impacts. The broad and diverse range of extreme precipitation impacts makes the regional information provided by the indicator suitable for a wide range of interests concerned with heavy precipitation climatology, variability, and change

at the local through CONUS levels including scientists and practitioners. The approach, which is analogous to the familiar Saffir-Simpson hurricane intensity scale, assigns categories from one to five to extreme three-day precipitation totals at each data point (grid cell or rain gauge). However, unlike the Saffir-Simpson scale, this approach is not designed to rank an individual storm event, but rather provide information at climate scales for pointwise magnitudes of heavy three-day precipitation totals while being extensible across datasets, time, and space. This approach, adapted from the "R-Cat" categorization scheme first presented in Ralph and Dettinger (2012), can then be stratified by season, geographic sub-region, or time period, while change in extreme event categories can be monitored across multiple spatial and temporal scales. By examining the observational uncertainty of this scheme, this study highlights both the utility of the approach as a means to depict the climatology of extreme precipitation, as well as what considerations should be made when choosing a reference dataset.

2.2 Data

We apply the extreme precipitation categorization scheme to five datasets, each constructed using a different approach and all provided at a relatively high spatial resolution. All datasets used for the intercomparison are summarized in Table 2.1 and described in more detail below.

2.2.1 Tropical Rainfall Measuring Mission (TRMM) 3B42V7

Satellite-derived precipitation data are from NASA's TRMM Multi-Satellite Precipitation

Analysis (TMPA herein) 3B42V7 product (Huffman et al. 2007; Huffman and Bolvin 2015). Prior to its decommissioning in 2015, TMPA was NASA's flagship precipitation measurement product (Liu et al. 2012). TMPA is provided with a 3-hourly temporal and 0.25° latitude/longitude spatial resolution, globally from 50°N to 50°S latitude from 1998-2015. TMPA measurements are produced using microwave-calibrated infrared (IR) estimates from multiple geo-stationary earth-orbiting and low-earth orbiting satellites (Huffman et al. 2007). The final precipitation estimates contain microwave-derived measurements and calibrated thermal IR-derived estimates. The spatial domain accounts for the tendency of microwave and IR estimates to lose skill at higher latitudes (Huffman et al. 2010). The 3B42V7 product incorporates monthly in situ gauge observations from the Global Precipitation Climatology Center and the Climate Assessment and Monitoring System for bias adjustment.

2.2.2 Integrated Multi-Satellite Retrievals for GPM (IMERG)

As a part of the Global Precipitation Measurement (GPM) mission, the Integrated Multi-satellite Retrievals for GPM (IMERG herein) product was developed as an extension of TMPA after decommission. IMERG data are provided at 0.1° latitude/longitude resolution every half hour between 60°N and 60°S latitude (Hou et al. 2014; Liu 2016). The GPM core observatory presents an increased orbiting inclination over TRMM, from 35° to 65° respectively, rendering more extensive latitudinal coverage (Huffman et al. 2017). Additionally, more advanced instrumentation capable of capturing multiple phases of precipitation is possible through the addition of a higher frequency radar offering an

improved sensitivity to light precipitation as well as to snow and ice. IMERG integrates algorithms from TMPA, the Climate Prediction Center morphing technique, and Precipitation Estimation from Remotely Sensed Information using Artificial Neural Networks. As of the writing of the paper, IMERG extends from April 2014 to the present, but will be retro-processed to overlap the TRMM era. IMERG and TMPA are freely available via the GES DISC.

2.2.3 Parameter-Elevation Regressions on Independent Slopes Model (PRISM)

PRISM uses point data and a digital elevation model (DEM) to generate gridded precipitation data (Daly et al. 1994). We utilize the daily PRISM product, offered on a 0.04° latitude/longitude grid over the CONUS. The PRISM technique attempts to account for physiographic effects such as coastal proximity and orography using the linear regression between gauge measurements and the elevation of the gauge taken from a DEM (Daly et al. 1994, 2002, 2008). The gauge measurements used for interpolation were supplied by various sources including the US National Weather Service Cooperative Observer Network and the Natural Resources Conservation Service daily snow pack telemetry gauges. Station network density relates to population density (Daly et al. 2007). The PRISM product is freely available from Oregon State University's PRISM Climate Group portal.

2.2.4 Modern-Era Retrospective Analysis for Research and Applications version 2 (MERRA-2)

The MERRA-2 atmospheric reanalysis product provides 3-hourly precipitation estimates generated on a 0.5° x 0.625° latitude-longitude grid. MERRA-2 is the latest multi-year reanalysis product produced by NASA's Global Modeling and Assimilation Office using the Goddard Earth Observing System version 5 (Molod et al. 2015; Gelaro et al. 2017; Reichle et al. 2017). This product corrects model generated precipitation estimates with observations, showing marked improvements upon its predecessor MERRA (Rienecker et al. 2011; Reichle et al. 2017). The method for merging observed precipitation into MERRA-2 assimilates aerosols and integrates MERRA-Land reanalysis for correction (Reichle et al. 2017). Estimates are further merged with precipitation generated by the MERRA-2 atmospheric general circulation model weighted according to latitude.

2.2.5 North American Regional Reanalysis (NARR)

NARR is based on the regional Eta Model and its 3D variation data assimilation system initialized from lateral boundary conditions provided by the National Centers for Environmental Information (NCEI) (Mesinger et al. 2006) and is freely available through the National Oceanic and Atmospheric Administration's Earth System Research Laboratory. This product is provided at a 3-hourly temporal resolution and a 32km spatial resolution (Lin et al 1999). Precipitation gauge observations are used to adjust atmospheric moisture and energy field estimates to improve model-derived precipitation fields.

2.2.6 Global Historical Climatology Network (GHCN)

In situ daily observations are from the NCEI Global Historical Climatology Network-Daily (GHCN-D) product (Menne et al. 2012). This dataset contains comprehensive in situ climatic data that have undergone extensive quality control procedures to limit internal, spatial, and temporal inconsistencies (Durre et al. 2010). For this study, only gauges reporting at least 90% of days over the period of 1998-2015 are included. The data are frequently updated and can be obtained freely via the web from NCEI.

2.3 Methodology

2.3.1 Extreme Precipitation Categorization Scheme

Extreme precipitation totals are grouped into five categories, or "P-Cats", according to their overall accumulated three-day total. P-Cats are defined as follows using even 100 mm thresholds as intuitive bounds on each category. A three-day total between 100 and 199 mm is assigned to P-Cat 1, 200 and 299 mm to P-Cat 2, 300 and 399 mm to P-Cat 3, 400 and 499 mm to P-Cat 4, and greater than 500 mm to P-Cat 5 (Fig. 2.1). Three-day totals are defined as the sum of accumulated precipitation for that day and the two preceding days such that if a P-Cat 4 is recorded on January 4th at a given location, the precipitation accumulated over January 2nd, 3rd, and 4th totaled between 400 and 499 mm. This window is then moved forward by one day each time step so that the three-day total for each day includes the sum of that day and the previous two. The P-Cat approach is a slightly modified version of the rainfall category or "R-Cat" approach introduced by

Ralph and Dettinger (2012). This scheme is also used operationally by the Scripps Institute of Oceanography Center for Western Weather and Water Extremes (http://cw3e.ucsd.edu/) to categorize discrete rainfall events associated with AR landfalls over California. Here we use the term "P-Cat" to clarify that this scheme is not only geared towards rainfall, hence the more general "precipitation". While similar to the R-Cat scale, the P-Cat approach offers an intuitive way to interpret and visualize extreme precipitation climatology across the CONUS and applied as an indicator of climate change and variability. Our P-Cats 2-5 are the same as R-Cats 1-4, however we introduce a lower category to capture a wider geography of extreme precipitation and a greater diversity of associated meteorological mechanisms. Multiday totals have been suggested as highly relevant to regional hydrologic impacts including flooding and landslides (Ralph and Dettinger 2012). Furthermore, Ralph and Dettinger (2012) indicate that the three-day window provides the best representation of major storms, with two-day totals missing storms and four-day periods revealing negligible differences to three-day periods.

We note that in using a fixed threshold we are capturing the most extreme three-day totals defined relative to the CONUS, rather than relative to the climatology of the grid point or station where the P-Cat occurs. As such, some dry portions of the CONUS do not observe P-Cat events during the time period of our analysis while other wetter places experience relatively frequent P-Cats. While this can be viewed as a caveat, the set of fixed thresholds provides an intuitive way to view extreme precipitation climatology and

track change in the magnitude of extreme precipitation over space and time. Furthermore, while not applied in this study, variants on the P-Cat approach could be developed that are regionally specific or customized for different datasets. In that sense, the threshold approach can also carry potential for novel climate model evaluation of extreme precipitation and assessment of projections of future changes.

2.3.2 Dataset Comparison

To assess the effect of observational uncertainty on using the P-Cat approach we compare the magnitude and frequency of P-Cats across a five-dataset suite. Magnitude is assessed by comparing the maximum observed P-Cat at each data point while frequency is examined both through total P-Cat occurrence as well as the average number of P-Cats observed per year or season. Dataset comparisons are performed and summarized over the CONUS as well as over the seven multi-state defined NCA regions (Fig. 2.2; Easterling et al. 2017). All comparison analyses are performed at the annual and seasonal scales with winter defined as December, January, February (DJF), spring as March, April, May (MAM), summer as June, July, August (JJA), and fall as September, October, November (SON). Comparison is performed over the period 1998-2015, which is the period of maximum overlap across all datasets. Additionally, IMERG is compared with TMPA for the years of overlap (2014-2015). In all analyses involving GHCN-D, the station data is used only for qualitative comparison to what can be considered ground truth.

Results for all the datasets are presented both on their native grid and a common grid for comparison and to assess the effect of spatial scale on P-Cat frequency and magnitude. Gridded datasets were rescaled, prior to assigning P-Cats, to a common 0.625° x 0.5° grid over the CONUS. This resolution matches that of the coarsest resolution product included in the study, MERRA-2. To rescale each gridded product, the first-order conservative remapping technique introduced in Jones (1999) was used. Conservative remapping acts to maintain the areal average (Chen 2008), unlike alternate methods such as bi-linear, bi-cubic, or distance weighted, and has been used in a number of studies (e.g., Nikulin et al. 2012; Kalognomou et al. 2013; Diaconescu et al. 2015). The spatial correspondence between the patterns of the regridded results are quantitatively summarized using Taylor diagrams, in terms of the centered root mean squared difference (CRMSD), standard deviation, and correlation coefficient (Taylor 2001). To construct a Taylor diagram, one dataset must be chosen as the reference to measure dataset similarities and differences against. In all Taylor diagrams here, PRISM is used as the reference dataset, chosen because it is the only gridded dataset based primarily on gauge data; however, this is not to say that PRISM is without bias.

2.4 Results

2.4.1 Annual Precipitation Climatology

As a first order comparison of dataset precipitation climatology, annual mean precipitation is shown for each dataset on its native grid in Fig. 2.3. All datasets show similar general climatology patterns, however, using GHCN-D as a reference (Fig. 2.3a),

considerable differences across the datasets emerge. First order differences relate to the representation of the effect of topography on precipitation, with the high-resolution PRISM (Fig. 2.3b) best resembling GHCN-D over the mountainous West and the lowest resolution MERRA-2 (Fig. 2.3e) showing the least detail. TMPA also has a notable dry bias relative to GHCN-D across the mountains of the Northwest despite its relatively high spatial resolution (Fig 2.3c), likely due to limitations in the ability of TMPA to measure snowfall (Bharti and Singh 2015). NARR (Fig. 2.3d) has a broad dry bias over much of the Southeast compared with GHCN-D and the other three datasets. MERRA-2 is too coarse to resolve most details of individual mountain ranges; however, it does show some qualitative similarities with GHCN-D over the coastal Northwest and northern Rocky Mountains.

2.4.2 Maximum P-Cats

The maximum recorded P-Cats are presented for the full year (Fig. 2.4), for DJF (Fig. 2.5), and for SON (Fig. 2.6). Fall and winter are chosen for seasonal analysis because they are concurrent with the most widespread occurrence of heavy precipitation, spanning two primary meteorological mechanisms consistent with the findings in Kunkel et al. (2012): atmospheric rivers often associated with extratropical cyclones in the West in both seasons (Neiman et al. 2008a, 2008b; Ralph and Dettinger 2011, 2012) and tropical systems in the Southeast in the fall (Knight and Davis 2009; Knutson et al. 2010; Kunkel et al. 2010). Results are summarized across seasons and sub-regions using Taylor diagrams in Fig. 2.7.

The spatial distribution of maximum observed P-Cats in GHCN-D (Fig. 2.4a, analogous to Fig. 2.3 from Ralph and Dettinger 2012) generally resembles the precipitation climatology in Fig. 2.3, with the highest P-Cats coinciding with the highest annual rainfall. This is supported in the West by the prevalence of high-end P-Cats across the coastal mountain ranges, the Sierra Nevada and Cascade ranges, and the Transverse Ranges of Southern California. High-end P-Cats are also more prevalent in the Southeast stretching from Texas eastward to the Carolinas. The maximum P-Cats recorded during this period are generally much lower across the Great Plains, the desert Southwest, and the interior western rain shadows.

All datasets capture the general pattern of relatively high P-Cats in the western mountains and Southeast, and low P-Cats over the Great Plains and Southwest. However, considerable differences are apparent in extent and magnitude. For example, PRISM shows the most widespread P-Cat 4 and 5s, likely due at least in part from it having the finest grid resolution and being constructed using gauge data. PRISM also shows a multitude of high-end P-Cats over the Southeast, which the other datasets do not capture, possibly indicative of localized convective precipitation that can be captured by the relatively dense gauge network used to construct PRISM here. TMPA (Fig. 2.4c) also captures a greater occurrence of high-end extremes compared to NARR and MERRA-2 (Figs. 2.4d, 2.4e).

While regridding reduces some of the P-Cat magnitudes through spatial smoothing, some differences persist (right column of Fig. 2.4; i.e., regridded to MERRA-2 resolution). In the case that high resolution is necessary for capturing processes leading to extreme precipitation (Herold et al. 2017), such as localized convection, then it is possible that a high-resolution dataset will maintain some high-end totals compared with the coarser products. Potentially illustrative of this effect, PRISM maintains a relatively high number of P-Cat 2-4s after regridding (Fig. 2.4f). The same effect is apparent for TMPA over the Southeast and Northwest. In addition to spatial resolution, other factors may also be important in determining the level of agreement after interpolation, including differences in the ability of the analysis products to accurately capture land-atmosphere interaction or potential bias and overestimation in PRISM (Mesinger et al. 2006; Bharti and Singh 2015; Molod et al. 2015).

The Taylor diagrams in Fig. 2.7a,b summarize the dataset correspondence for the CONUS annually and seasonally and NCA sub-regions annually respectively. At the seasonal scale (Fig. 2.7a), NARR and MERRA-2 show a lower spatial standard deviation across all seasons with TMPA generally exceeding PRISM. TMPA also has a greater spread in pattern correlation resulting in larger CRMSD values compared with NARR and MERRA-2, especially for DJF and MAM. Both NARR and MERRA-2 cluster closely at the CONUS scale across the seasonal cycle. Less spread is apparent at the sub-region scale (Fig. 2.7b) with all datasets revealing similar spatial variance and correlation relative to PRISM.

In SON, the highest observed P-Cats captured by GHCN-D (Fig. 2.5a) are over the Pacific Northwest, central Texas, and the Gulf and Atlantic Coasts of the Southeast. P-Cat 1 and 2s are common throughout the higher elevations of the West and across the Midwest through the Northeast. Several examples of Southwest to Northeast oriented bands of P-Cat 2s are apparent in the central US. For example, one band extends from northern Illinois to southeastern Michigan and provides a useful baseline for comparing the details of the other datasets. In many cases, very high-end P-Cats can readily be traced to the contributing storm. For example, the high values over eastern North Carolina are the result of Hurricane Floyd that made landfall in September of 1999, which brought catastrophic societal impacts (Easterling et al. 2000). The similarities between Figs. 2.4 and 2.5 over the Southeast indicate that most of the highest recorded P-Cats occur during SON here.

Consistent with our previous findings, PRISM captures the greatest magnitude and spatial extent of high-end totals (Fig. 2.5b), sharing the most qualitative similarities with the GHCN-D results, including the collocation of the southwest to northeast oriented bands of P-Cat 2s across the Midwest and topographic enhancement in the West. These features are generally captured in the other datasets, however with lower magnitudes. In some cases, regional-scale details are not similar across the suite especially in the case of the high-end P-Cats over the Southeast where MERRA-2 and NARR show varying degrees of dissimilarities with the other datasets. As in Figs. 2.3 and 2.4, there is a close

relationship between spatial resolution and P-Cat magnitude, however even considering a systematic resolution related bias, some fundamental differences persist.

After spatial interpolation, PRISM and TMPA maintain high-end totals over Washington and North Carolina (Fig. 2.5f,g). MERRA-2 and NARR generally show systematically lower PCat magnitudes relative to the regridded PRISM and TMPA, providing further evidence of factors other than resolution being influential on dataset agreement (Fig. 5e,h). In Fig. 2.7c dataset spread is small between MERRA-2 and NARR, especially across the variance ratio, while TMPA tends to exceed PRISM's spatial variance in most sub-regions. Note that we omit results for Great Plains North because of its very low number of grid cells with P-Cats. In DJF (Fig. 2.6), the overall spatial coverage of stations recording P-Cats is lower than SON, especially across the central US. GHCN-D shows the most extreme precipitation occurring along the western mountains stretching from northern Washington to southern California and across the southern Midwest and Southeast (Fig. 2.6a). This is evidence that the intense precipitation from North Pacific extratropical cyclones is maximized by the orographic enhancement of landfalling atmospheric rivers (e.g., Neiman et al. 2008a, 2008b; Guan et al. 2010, 2013; Ralph and Dettinger 2012). Across the eastern half of the CONUS, high-end P-Cats are the result of strong mid-latitude cyclones that strengthen along the strong temperature gradients formed by southward excursions of Arctic air masses.

In agreement with GHCN-D, PRISM shows many of the high-end totals that occur across the West (Fig. 2.6b). TMPA's limitations at capturing snowfall are apparent with considerable under-estimation of the magnitude of P-Cats along the Sierra Nevada and Cascades (Fig. 2.6c). These results are consistent with Behrangi et al. (2014a), emphasizing the inherent challenges associated with measuring precipitation in remote regions, where station data are sparse, orography and fine scale processes are key, and precipitation type limits utility of TMPA retrievals. Substantial differences in the magnitude of P-Cats captured by NARR and MERRA-2 (Fig. 2.6d,e) suggest that grid resolution may inhibit the ability of a dataset to capture the impact of localized phenomena, although both datasets capture the broad patterns of P-Cats across the West and Southeast.

While regridding reduces the overall magnitude of P-Cat intensity in PRISM and TMPA, both datasets continue to show more P-Cat 2 and 3s. Over the Southeast, resolution does not appear as important at capturing high-end P-Cats, which is consistent with the typical synoptic scale storms that result in extreme precipitation here in winter. This also provides evidence that differences across datasets are also driven by dataset construction, and not solely a result of grid resolution. The Taylor diagram in Fig. 2.7d shows that TMPA exhibits a higher variance relative to PRISM over the Southeast and roughly the same in the Northwest, with all other datasets and sub-regions showing a slightly lower spatial variance than PRISM and pattern correlation coefficients between 0.9 and 0.99.

2.4.3 P-Cat Frequency

As for comparison of P-Cat magnitude in the above section, P-Cat frequency, computed as P-Cats per year or season, is compared across the entire year (Fig. 2.8), for SON (Fig. 2.9), and for DJF (Fig. 2.10). Differences across the data suite are also presented as biases, with reference to PRISM. Results are further summarized using Taylor diagrams in Fig S1.1.

The highest annual frequency of P-Cats in GHCN-D (Fig. 2.8a) generally corresponds spatially to the highest magnitude P-Cats in Fig. 2.4a. These areas include the Southeast and the mountains of the Pacific Northwest and California where annual P-Cat frequency exceeds 20. For reference, if a station shows an average frequency of 20 P-Cats/year, this would mean that on average 20 days of every year are part of a three-day precipitation total that exceeds 100 mm. In such cases, heavy precipitation is relatively common and the simple occurrence of a P-Cat may not necessarily be considered highly extreme in a local climatological context. In contrast, a large swath of the eastern half of the domain experiences between 2 and 8 P-Cats annually, while P-Cats are infrequent across the High Plains and the inland West. P-Cats 1 and 2 make up the vast majority of P-Cats/year CONUS-wide with some areas of the West and Southeast recording as many as two high-end P-Cats/year (not shown).

All datasets capture similar principal spatial patterns of annual P-Cat frequency. Qualitatively, PRISM (Fig. 2.8e) most closely resembles GHCN-D, even capturing many

of the small-scale features in areas of complex terrain and regional variations in the Southeast. TMPA (Fig. 2.8f) shows notable positive frequency bias across the eastern half of the CONUS and over the valleys of the coastal Northwest with lower frequencies across the western mountains, compared with PRISM. NARR and MERRA-2 both share similarities, with systematically lower P-Cat occurrence compared with PRISM after regridding. NARR shows a greater frequency of P-Cats across the Sierra Nevada compared with MERRA-2, however both datasets show considerable negative frequency biases across most of the West.

During SON (Fig. 2.9), GHCN-D shows the highest frequency of P-Cat occurrence in the Northwest and Southeast with values exceeding 10 P-Cats per season along the coasts of Washington and Oregon and between 2 and 4 in southeast Texas and southwest Louisiana (Fig. 2.9a). This indicates that at least 4 days per fall are part of a 100-mm or greater three-day precipitation total on average in these places. There are many commonalities between the frequency map in Fig. 2.9a and the maximum P-Cat map in Fig. 2.5a, with many of the regions that experience high values of one also experiencing high values of the other. However, this isn't always the case in some parts of the South and along the Atlantic Coast of Florida where P-Cats are common, but rarely exceed P-Cat 2.

Consistent with expectations based on the above results, the observation-based TMPA and PRISM (Fig. 2.9b,e) share the most similarities with GHCN-D. PRISM captures the

overall spatial patterns and frequency magnitudes, but it is also capable of resolving small scale features such as higher frequencies over southeastern Texas. Over the Northwest, as in other analyses, TMPA's limitation at capturing frozen precipitation likely contributes to its negative biases over the mountains (Behrangi et al. 2014a), however it shows a weak positive frequency bias across the lower elevations of the coastal Northwest. NARR and MERRA-2 resemble each other with systematic low frequency bias across the CONUS (Fig. 2.8f-h).

During winter (Fig. 2.10a), the P-Cat frequencies are highest across the mountains of Washington, Oregon, and California with elevated P-Cat frequencies also occurring in the higher elevations of Idaho, Utah, and Arizona. In contrast, the other area of high P-Cat occurrence is a broad swath of the South and southern Midwest where Gulf of Mexico moisture fuels heavy precipitation associated with midlatitude cyclones. PRISM (Fig. 2.10b) captures the mountain ranges across the West and the general pattern in the East (Fig. 2.10e). PRISM underestimates the isolated high frequency P-Cats that GHCN-D captures over the higher terrain of Idaho and Utah. TMPA (Fig. 2.10b) resembles both PRISM and GHCN-D, but with substantial high frequency biases over the lower elevations of the West Coast and throughout the Southeast (Fig. 2.10f). A physical explanation for this widespread bias in TMPA is unclear as it is not consistent with findings from other seasons or at the annual scale. TMPA also shows negative biases along the immediate Pacific Coast, suggesting frozen precipitation is not the only contributor to underestimation in the West. NARR and MERRA-2 are quite similar with

overall negative frequency biases across the CONUS with the exception of some western valleys.

2.4.4 Annual P-Cat Occurrence

Figs. 2.11-2.13 show spatially aggregated P-Cat frequencies over time. Here we only show results for annual frequency at the CONUS scale, for DJF over the Northwest, and for SON over the Southeast to capture the regions and corresponding seasons where high-end P-Cats are most common. In each figure, the left column shows the number of P-Cats per category on the native grid of each dataset, while the right column represents the datasets interpolated to the MERRA-2 grid. This means that all things equal, prior to regridding the coarser resolution datasets will have a lower frequency of P-Cat occurrence, simply because there are more data points in the high resolution cases. In this sense, the left column is intended for qualitative comparison while the right column compares datasets with an equal number of data points.

For most years the full range of P-Cats occurs somewhere over the CONUS according to GHCN-D (Fig. 2.11a). There is no apparent systematic trend in the frequency of any P-Cat occurrence across the CONUS and the datasets. Comparing each dataset to GHCN-D, datasets tend to show a similar evolution of interannual variability. For example, the year 2000 shows a relative minimum in P-Cat 2s in all datasets. Consistent with results from Figs. 2.4-2.10, high-end P-Cats are most common in PRISM (Fig. 2.11b) while they are most rare in NARR and MERRA-2 (Figs. 2.11d,e). When compared on a common

grid, P-Cat 1 frequencies are more comparable across the suite. PRISM (Fig. 2.11f) maintains a number of P-Cats 3 and 4s after regridding. The coefficients of variation for each P-Cat time series, computed as the standard deviation of each dataset's annual frequency divided by its mean, are recorded in Table 2.2. All datasets show a greater year-to-year variability in higher-end P-Cats relative to lower-end P-Cats. For example, GHCN-D has a coefficient of variation for the annual frequency of P-Cat 5s that greatly exceeds that of P-Cat 1s.

During SON over the Southeast (Fig. 2.12), GHCN-D shows a high number of P-Cat 4 and 5s occurring during 1998 and 1999 (Fig. 2.12a) with considerable interannual variability throughout the record. PRISM (Fig. 2.12b) continues to show the greatest number of high-end P-Cats compared with the other datasets. TMPA also captures higher-end P-Cats in the early part of the record (Fig. 2.12c), including 1999. NARR and MERRA-2 (Fig. 2.12d,e) show primarily P-Cat 1 and 2s, with MERRA-2 showing some P-Cat 3s in 1998 and 1999 suggesting that it realistically represents the high-end totals captured in the finer resolution datasets but with diminished magnitude. This reduced magnitude of extremes likely results in part from the coarser reanalysis resolution, but differences may also stem from the dataset generating algorithms. When compared on a common grid, dataset agreement is much stronger, although NARR stands out as having the lowest P-Cat occurrence, and datasets capture similar interannual variability. The coefficient of variation results continue to show greater variability among the most extreme P-Cats across the five-dataset suite (Table 2.3).

Resolving topography is important for capturing P-Cats in DJF in the Northwest sub-region (Fig. 2.13). GHCN-D and PRISM (Fig. 2.13a,b) show the most qualitative agreement including with interannual variability, with NARR also sharing commonalities in year-to-year fluctuations (Fig. 2.13d). When compared on common grids, overall magnitudes of P-Cat 1s are in reasonable agreement across the suite, however interannual variability is still somewhat different in TMPA (Fig. 2.13g) compared with PRISM and NARR (Fig. 2.13f,h). These results further suggest using caution when measuring and monitoring extreme precipitation across areas of complex terrain where orographic effects on precipitation are key and extremes are often associated with frozen precipitation. The dataset's annual P-Cat frequency results for DJF in the Northwest continue to show greater variability as the P-Cats increase (Table 2.4).

2.4.5 Comparison of Individual Storms

While the primary aim of implementing the P-Cat scheme in this study is to track and describe extreme precipitation climatology at the grid point scale, as another way to intercompare the five datasets and as a way to further demonstrate the reliability of the P-Cat approach in capturing extreme precipitation, we show the P-Cat values associated with individual historically impactful storms. Fig. 2.14 shows four examples while additional examples are provided in Figs. S1.2-S1.4. Examples were chosen to capture a wide range of storm types occurring across a diverse range of geographic areas. The top row shows the P-Cat values associated with the landfall of Hurricane Floyd in September

of 1999. Note that the P-Cat values are based on the three-day rainfall totals ending on the date specified to the right of each row. All datasets capture high-end P-Cats (3-5) over a similar region, while NARR shows relatively modest P-Cats. This indicates that all datasets with the exception of NARR are capable of capturing the magnitude of rainfall associated with this intense tropical system.

In the second row from the top, P-Cats from a notable atmospheric river event from November 2006 are shown with generally good qualitative agreement across the datasets despite the coarser datasets showing overall lower P-Cat magnitudes. There is some indication, however, that PRISM overestimates the magnitude of rainfall over the northern Oregon Coastal Mountains and the Olympic Mountains. The third row from the top compares P-Cats for an intense winter storm that occurred during December 2015. All datasets capture the swath of P-Cats 1 and 2 extending from northeast Texas into central Illinois indicating reasonable qualitative agreement in the magnitude and extent of heavy precipitation from this powerful winter storm. Lastly, the bottom row shows a comparison for a strong mesoscale convective system that occurred in September 2004. While all datasets can capture the convective precipitation to the extent that it surpasses the P-Cat 1 threshold, TMPA shows a relatively larger area of P-Cats compared with the other datasets suggesting some difference how it captures convective precipitation in this event. We also note that the P-Cat approach is capable of visualizing the propagation of weather events that produce heavy rainfall totals. Fig. S1.5 shows five-day evolutions of P-Cats for two hurricanes and one winter storm. The P-Cats show the temporal, spatial,

and intensity evolution of the storms highlighting the efficacy of the three-day total approach to capture observed heavy precipitation events.

2.4.6 IMERG Intercomparison

Considering the potential benefits of using remote sensing to continuously monitor and track extreme precipitation over time, we compare IMERG data to its predecessor, TMPA in Fig. 2.15. The latest release (V6) of IMERG fuses the early precipitation estimates of the TRMM satellite (2000-2015) with the more recent precipitation estimates collected during operation of the GPM satellite (2014 - present). At the time this study was conducted, we leveraged the existing overlap period (April 2014 - December 2015), using the maximum observed P-Cats as well as total observed P-Cat frequency for comparison. Over this two-year period, there is some indication that IMERG captures more small-scale features and better represents extremes over the mountainous West (Fig. 2.15c). These results are likely attributable, at least in part, to IMERG's higher spatial resolution, but may also be due to improvements in GPM sensors to measure snow (Hou et al. 2014). This qualitatively brings IMERG closer to GHCN-D with exceptions. For example, IMERG does a poorer job at capturing the band of P-Cat 2s stretching from northeast Texas through Missouri compared with TMPA and overestimates P-Cat magnitude over eastern Tennessee and northern Alabama. P-Cat frequencies reveal similarities between TMPA and IMERG (Fig. 2.15d).

2.5 Summary and Conclusions

Here we present a climatology of a categorization scheme for monitoring and tracking change in extreme precipitation over space and time and assess its observational uncertainty. The approach assigns a category between one and five to three-day storm totals (Fig. 2.1). Intended as a way to track extreme precipitation as a climate indicator, this scheme provides a platform for monitoring change in extreme precipitation across scales, datasets, time, and geography. However, precipitation observation products are all associated with some degree of bias, making it important to understand and attempt to constrain observational uncertainty when analyzing extremes. To demonstrate the utility of the P-Cat scheme as a way to track extreme precipitation events in time and space and to highlight the importance of understanding observational uncertainty, we apply the three-day total categorization as a basis for dataset intercomparison across four gridded products, spanning a range of construction methodologies, and in situ station data.

All gridded datasets capture the principal spatial patterns of mean annual precipitation climatology, with higher resolution datasets capturing more orographic features than the lower resolution datasets (Fig. 2.3). Focusing on extremes, the magnitude (Figs. 2.4-2.7) and frequency of P-Cats (Figs. 2.7-2.11) are assessed using the P-Cat scheme as a metric for intercomparison. In general, the higher resolution datasets more closely resemble gauge data across the CONUS and seasons. Specifically, PRISM shares many detailed commonalities with station data while the next highest resolution dataset, TMPA, is also similar overall. NARR and MERRA-2 reanalysis show systematically lower magnitude

and frequency of P-Cats across the CONUS and seasonal cycle. TMPA shows systematically lower P-Cat magnitudes and frequencies across the mountains of the West during fall and winter when a large portion of precipitation falls as snow, consistent with known limitations of TMPA at capturing frozen precipitation.

When all datasets are interpolated to a common coarser grid, differences persist but are reduced. In particular, the datasets that were originally constructed at the highest spatial resolution often maintain the highest magnitude of P-Cats, even after coarsening of the gridded data. This feature could result from a number of factors; however, one likely contributor is the fact that a dataset constructed originally at fine resolution is able to capture extreme events that simply could not be resolved at coarser grids (Herold et al. 2017). This may be particularly acute in areas of complex topography where, for example, PRISM is able to resolve local high magnitude events that the other datasets are simply not capable of capturing. Other factors could include other underlying biases in the dataset stemming from factors such as spatial and temporal heterogeneity in gauges (Kidd 2001), sensor sensitivity to precipitation type (Behrangi et al. 2012, 2014b) or methods of retrieving precipitation from individual sensors in satellites (Kummerow et al. 2011), interpolation methods or misrepresentation due to the sparseness of the observing network (Min et al 2011), and general deficiencies and model limitations simulating precipitation amounts in reanalysis (Kharin et al. 2013). The annual occurrence of P-Cats shows similar differences across the suite, with a general positive relationship between grid resolution and the number of P-Cats (Figs. 2.11-2.13).

Preliminary assessment of IMERG, the follow-on satellite product to TMPA, suggests some potential improvements over TMPA in capturing frozen precipitation and fine-scale extremes (Fig. 2.15). Ultimately, results suggest satellite data show promise in capturing the overall patterns of heavy precipitation climatology, which could lead to improved monitoring in regions with sparse ground observations. It is worth noting that since this analysis was conducted, the IMERG record has been extended back to the year 2000. A recent global study by Arabzadeh et al. (2020) intercompares atmospheric river precipitation in remote sensing and reanalysis products globally, using IMERG's longer data record (2001-2018), finding IMERG overestimated AR-related precipitation, misrepresented cold season light precipitation and snowfall, as well as deviated significantly from reanalysis at fine regional scales, attributed to a lack of sufficient in situ observations for calibration. However, at a higher temporal (30-minute) and spatial resolution (0.1°), the IMERG dataset offers the opportunity for capturing localized short-duration extremes across a larger latitudinal extent (60°N-S). IMERG has further been shown to depict the duration, spatial extent, and speed of storm propagation as it contributes to local and regional precipitation accumulation and heavy precipitation event impacts across the CONUS, characteristics difficult or impossible to extract from previous generation, lower resolution gridded datasets (Zhou et al. 2019).

We acknowledge some assumptions and limitations in use of the P-Cat scheme as a climate indicator for extreme precipitation. First, the use of fixed thresholds for the entire

CONUS is intended to highlight the heaviest precipitation across the domain in an intuitive way. As such, some drier regions do not record P-Cats as defined in this study, even though smaller totals may be considered impactful relative to local climatology. The synoptic scale of measurement also captures totals at a temporal scale often associated with impacts such as flooding and landslides (Ralph and Dettinger 2012) but does not distinguish between shorter and longer duration totals. This may be relevant for lower-end P-Cats that could result from short duration extreme convective events. It is also possible that a single storm may be counted more than once due to the moving three-day window used to construct the P-Cat. Finally, while we include the five datasets here in an effort to capture a range of measurement methods while focusing on high resolution products, this analysis could be extensible to other observations.

Overall, the P-Cat characterization scheme applied here offers several opportunities for future research and applications. By comparing P-Cat climatology in climate model simulations of the historical climate to observations, this scheme could provide a novel target for climate model evaluation. As further extension of the P-Cat approach for dataset intercomparison, P-Cat thresholds could be customized to a dataset's grid resolution to account for the inherently lower magnitude of extremes captured at coarser versus finer resolutions although this could come with somewhat reduced levels of intuitiveness since a P-Cat 1 would be different for different datasets. The P-Cat scheme could also be used for assessing future projections of changes in extreme precipitation in climate models. Lastly, the P-Cat approach is easily extensible to other regions,

facilitating temporal and spatial tracking and monitoring of extremes, dataset intercomparison, model evaluation, and future change assessment.

Chapter 3: A Climatology of Atmospheric Rivers and Associated Precipitation for the Seven US National Climate Assessment Regions

This chapter is published as: Slinskey, E. A., P. C. Loikith, D. E. Waliser, B. Guan, and A. Martin, 2020: A Climatology of Atmospheric Rivers and Associated Precipitation for the Seven U.S. National Climate Assessment Regions, *Journal of Hydrometeorology*, **21**(11), 2439-2456, https://doi.org/10.1175/JHM-D-20-0039.1.

Abstract

Atmospheric Rivers (ARs) are long, narrow filamentary regions of enhanced vertically integrated water vapor transport (IVT) that play an important role in regional water supply and hydrometeorological extremes. Here, an AR detection algorithm is applied to global reanalysis from Modern-Era Retrospective Analysis for Research and Applications, version 2 (MERRA-2) to objectively and consistently characterize ARs regionally across the continental United States (CONUS). AR characteristics and associated precipitation are computed at the grid point scale and summarized over the seven US National Climate Assessment (NCA) regions. ARs are most frequent in the fall and winter in the West, spring in the Great Plains, and fall in the Midwest and Northeast. ARs show regional and seasonal variability in basic geometry and IVT. AR IVT composites reveal annually consistent northeastward directed moisture transport from the Pacific Ocean in the West, while moisture transport patterns vary seasonally across the Southern Great Plains and Midwest. Linked AR precipitation characteristics suggest that a substantial proportion of extreme events, defined as the top 5% of three-day

precipitation totals, are associated with ARs over many parts of CONUS, including the East. Regional patterns of AR-associated precipitation highlight that seasonally-varying moisture transport and lifting mechanisms differ between the East and the West where orographic lifting is key. Our study aims to contribute a comprehensive and consistent CONUS-wide, regional-scale analysis of ARs in support of ongoing NCA efforts. Given the CONUS-wide role ARs play in extreme precipitation, findings motivate continued study of associated climate change impacts.

3.1 Introduction

Atmospheric rivers (ARs) are long, narrow regions of strong horizontal water vapor transport (Zhu and Newell 1994, 1998; Ralph et al. 2004) responsible for a multitude of hydrometeorological impacts (Guan et al. 2010; Dettinger et al. 2011; Neiman et al. 2011; Moore et al. 2012; Dettinger 2013; Mahoney et al. 2016). Typically associated with a low-level jet (LLJ) ahead of the cold front in the warm sector of an extratropical cyclone (AMS 2017), ARs cover only ~10% of Earth's zonal circumference but account for >90% of the total poleward water vapor transport in the midlatitudes (Zhu and Newell 1998; Guan and Waliser 2015). A typical AR is several thousand kilometers long and only a few hundred kilometers wide, capable of transporting more water than the largest rivers on Earth (Ralph et al. 2017). Enhanced precipitation occurs when the AR interacts with a mechanism capable of lifting it beyond saturation level. Some examples include orographic lifting (Ralph et al. 2005), convection (Letkewicz and Parker 2010), and synoptic scale frontal systems (Businger 1990), among others.

In water-stressed regions, such as parts of southwestern United States (US), ARs provide a crucial source of water through replenishing reservoirs, contributing to snowpack at higher elevations, and often alleviating existing drought conditions (Guan et al. 2010; Dettinger 2013; Paltan et al. 2017). On the other hand, the extreme precipitation associated with ARs can lead to flooding (Ralph et al. 2006; Neiman et al. 2011; Konrad and Dettinger 2017), rain-on-snow events (Guan et al. 2016), levee breaks (Florsheim and Dettinger 2015), landslides (Young et al. 2017), debris flows (Oakley et al. 2017), and avalanches (Hatchett et al. 2017). Furthermore, research linking ARs with underlying patterns of damaging coastal extreme winds (Waliser and Guan 2017) and resulting storm surges (Khouakhi and Villarini 2016) suggests ARs are associated with effects beyond their role in precipitation extremes.

The hydrometeorological extremes associated with ARs are well documented along the West Coast. Water availability concerns in California have motivated a growing number of analyses, identifying landfalling ARs as responsible for between 30%-70% of the annual precipitation (Guan et al. 2010; Dettinger et al. 2011; Gershunov et al. 2017) as well as the majority of precipitation extremes (Ralph et al. 2004; Ralph and Dettinger 2012; Lamjiri et al. 2017) and flooding across the state (Ralph et al. 2006, 2013). Destructive flooding associated with AR conditions has also been documented over parts of Oregon and Washington (Neiman et al. 2008a, 2011; Warner et al. 2012). A study extending from the Mexico/California border northward into British Columbia, Canada,

highlighted the importance of ARs in modifying the region's climate and yielding important hydrologic consequences, including increased precipitation, river/stream flows, vapor fluxes, and changes in snow water equivalent (Neiman et al. 2008b).

Considerably less attention has focused on the role of ARs in other regions of the US; however, a number of heavy precipitation and high-impact flood events have been linked with AR-like conditions across parts of the central/eastern US. For example, Moore et al. (2012) and Lackmann et al. (2013) linked AR conditions with severe flooding in Tennessee in May 2010. More recently, Rabinowitz et al. (2018) found 15 AR events between 2010-2015 contributed to 67% of the total monthly precipitation across the north-central Mississippi River Valley, consistent with Lavers and Villarini (2013b). Nakamura et al. (2013) further presents evidence of AR conditions governed by an anomalous semi-stationary ridge east of the US East Coast attributable to flooding in the Ohio River Basin. Across the Southeast, ARs have been documented as an important contributor to annual rainfall totals and heavy precipitation event frequency (Mahoney et al. 2016; Debbage et al. 2017; Miller et al. 2018). Despite this documented importance of ARs across the Continental United States (CONUS), AR climatology has not received the same level of comprehensive documentation away from the West Coast.

The importance of ARs in weather and climate has further prompted increasing interests in the behavior of ARs under global warming (e.g., Dettinger 2011; Lavers et al. 2013; Gao et al. 2015; Payne and Magnusdottir 2015; Warner et al. 2015; Hagos et al. 2016;

Shields and Kiehl 2016; Espinoza et al. 2018; Gershunov et al. 2019). Existing literature suggests that many aspects of ARs may change under future warming, including frequency, geometry, integrated water vapor transport (IVT) magnitude, seasonality, and associated flood risk (Waliser and Cordiera 2020, and references therein). Furthermore, changes in the frequency or intensity of ARs could affect the occurrence and magnitude of associated precipitation and flooding, warranting continued observational analysis to benchmark historical change and provide a target for model evaluation (e.g., Guan and Waliser 2017).

ARs were highlighted for the first time in the Fourth National Climate Assessment (NCA) Climate Science Special Report (CSSR) as a key topic in its chapter on "Extreme Storms" (Kossin et al. 2017). Key findings in the report summarized the importance of ARs along the US West Coast to snowpack and annual precipitation. It also highlighted possible future increases in the frequency and severity of landfalling ARs related to increased evaporation and higher atmospheric water vapor concentrations with increasing temperature. Motivation for this work is to help provide a more comprehensive and consistent CONUS-scale analysis of ARs over the seven NCA regions (Fig. 2.2) as a contribution to future reports. In this study we regionally examine AR climatologies across the CONUS and investigate the associated precipitation characteristics. The hydrometeorological importance of ARs has prompted significant incentive to improve our understanding of ARs at regional scales to inform resource management, hazard resilience, and decision-making as well as provide a basis for assessing future change.

Previous studies have explored AR climatology across a range of spatial scales and geographies (e.g.,Dettinger et al. 2011; Moore et al. 2012; Rutz et al. 2014; Guan and Waliser 2015; Lavers and Villarini 2015; Mahoney et al. 2016; Debbage et al. 2017), however this study is novel in the level of detail it provides in regards to AR characteristics and their relation to extreme precipitation at a relatively high spatial resolution over the CONUS. Furthermore, this study, to the authors' knowledge, is the first to summarize AR climatology and importance as a mechanism for extreme precipitation over the seven NCA regions.

3.2 Data

3.2.1 Modern-Era Retrospective Analysis for Research and Applications, version 2 (MERRA-2)

ARs are identified using the National Aeronautics and Space Administration's (NASA) Modern-Era Retrospective Analysis for Research and Applications, version 2 (MERRA-2; Gelaro et al. 2017) reanalysis internally-derived IVT fields. Daily average IVT is calculated from hourly MERRA-2 IVT data provided on a 0.5° latitude × 0.625° longitude grid (Bosilovich et al. 2016) spanning 36 years over the period of 1981-2016. IVT is generated from zonal and meridional winds and specific humidity fields. The use of internally derived IVT values through the MERRA-2 system have the advantage of being calculated across all (internal) model time steps and on all model vertical coordinates, not just the standard output pressure levels, and therefore may be preferable over coasts and mountains (Dettinger et al. 2018). MERRA-2 uses the Goddard Earth

Observing System Model, version 5 (GEOS-5) state-of-the-art data assimilation system and is freely available online through the Goddard Earth Sciences (GES) Data and Information Services Center (DISC) (http://disc.sci.gsfc.nasa.gov/mdisc/). While other reanalysis products could be employed to detect ARs, MERRA-2 has been utilized in the study of ARs in previous studies (e.g., Guan and Waliser 2017; Lora et al. 2017; Mundhenk et al. 2018) and is the default reference dataset for the AR Tracking Method Intercomparison Project (ARTMIP; Shields et al. 2018) facilitating the comparison of results from this study across other AR detection algorithms. AR characteristics based on MERRA/MERRA-2 and ERA-Interim are remarkably similar to each other (e.g., Guan and Waliser 2015, 2017, 2019; Guan et al. 2018), and the selection of a specific contemporary reanalysis product is not expected to change the conclusions of this paper.

3.2.2 Parameter-elevation Regressions on Independent Slopes Model (PRISM)

Spatially interpolated, ground-based precipitation measurements were obtained from the Parameter-elevation Regressions on Independent Slopes Model (PRISM; Daly et al. 2008). This dataset incorporates observations from monitoring networks across the CONUS and uses a weighted regression to interpolate climate data based on topographic and physiographic variables using a digital elevation model. PRISM offers high resolution precipitation measurements on a 0.04° latitude/longitude grid over the CONUS that have been used in a wide range of climatology studies (e.g., Behrangi et al. 2016; Demaria et al. 2017; Kim et al. 2018). A detailed assessment of observational uncertainty in PRISM, alongside a suite of historical precipitation measurement approaches, in

capturing three-day extreme precipitation climatology can be found in *Chapter 2*. Daily precipitation estimates available from 1981 are used for this analysis. PRISM data can be obtained from the PRISM Climate Group at Oregon State University (http://prism.oregonstate.edu/).

3.3 Methodology

3.3.1 AR Identification

The objective identification of ARs employed here is based on the approach introduced in Guan and Waliser (2015) and later updated and validated with in-situ/dropsonde data in Guan et al. (2018). This approach applies a combination of geometry and IVT magnitude/direction criteria to identify contiguous regions (i.e., areas of connected grid cells), or "objects", of enhanced IVT transport. Objects first retained from IVT magnitude thresholding (i.e., above the seasonally- and geographically-dependent 85th percentile) are further filtered using directional and geometric requirements. In addition to having an appreciable poleward component (>50 kg m^{-1} s^{-1}), more than 50% of the area of the IVT object must have IVT directions within 45° of the mean IVT direction of the object. This ensures general coherence in IVT direction within the object. Geometric requirements are then applied, and objects longer than 2000 km with length-to-width ratios >2 are retained as ARs. Multiple, sequentially higher IVT magnitude thresholds (i.e., 85th- 95th percentiles at an increment of 2.5) are applied if an IVT object fails the other criteria. For each of the 12 months, the 85th percentile IVT is shown for reference in Fig. S2.1. The use of multiple IVT thresholds allows for the identification of ARs within

the core region of a larger, wider object that may not meet the geometry criteria (Guan et al. 2018).

The AR detection algorithm employed here consists of a broad and generalized AR definition, as in Zhu and Newell (1998), that does not impose predetermined geographical requirements for AR identification (as noted in Guan and Waliser 2017) and does not isolate collocated mechanisms of moisture transport (e.g., North American Monsoon, etc.). This method defines ARs based on moisture transport and connected object characteristics only. Therefore, it does not consider spatiotemporally related phenomena (e.g., fronts and extratropical cyclones) that are part of the phenomenological understanding of ARs in the global climate. Defining ARs in this way is consistent with current literature (Shields et al. 2018), and it is beyond the scope of this study to attempt to link AR objects with any phenomena besides extreme precipitation. We will alert the reader when interpreting AR activity, characteristics, and hydrometeorological impacts if such interpretation overlaps with other well-documented phenomena of the climate system, such as tropical and extratropical cyclones, convective systems, etc.

3.3.2 Linked AR Extreme Precipitation Days

Extreme precipitation days are defined as three-day precipitation totals exceeding the 95th percentile of non-zero three-day totals, calculated at each grid cell. The use of a percentile-based threshold defines extremes based on the local climatology. Three-day totals are calculated such that each day's three-day total includes the sum of that day and

the previous two (as in *Chapter 2*). While single-day totals are a common measure for precipitation, the use of multiday totals have been shown to better capture some heavy precipitation impacts while also reducing uncertainty due to temporal mismatch among data products (Ralph and Dettinger 2012). Herein we refer to qualifying three-day totals as extreme precipitation days. An AR extreme precipitation linkage is made when at least one AR is present during the three-day window defining the precipitation extreme.

A minimum distance-based interpolation scheme is used to link AR characteristics, defined using MERRA-2, with PRISM's high resolution precipitation measurements. We developed this process to assign MERRA-2's coarser resolution grid cells to PRISM's finer resolution grid cells. More specifically, each PRISM grid cell is linked with the MERRA-2 grid cell that has the shortest distance from the grid cell center. All analyses are performed seasonally with winter defined as December, January, February, spring as March, April, May, summer as June, July, August, and fall as September, October, November.

3.4 Results

3.4.1 AR Characteristics

3.4.1.1 AR Frequency

The seasonal distribution of AR frequency, calculated at each grid cell as the percentage of days when the grid cell is within the boundary of an AR for that season, across the CONUS is shown in Fig. 3.1. Results show ARs are primarily a cold season phenomenon

along the West Coast. Consistent with Rutz et al. (2014), maxima occur in the winter in the Southwest and in the winter and fall in the Pacific Northwest (PNW; Fig. 3.1a,d). East of the Rocky Mountains, AR occurrence is notable throughout the year. A wintertime maximum is evident across the Southeast with a rate of AR occurrence of >13% of winter days (Fig. 3.1a). High AR occurrence over the Great Plains and Ohio River Valley in the spring (~12%; Fig. 3.1b) may be related to moisture transport through features like the Great Plains LLJ (Nakamura et al. 2013; Lavers and Villarini 2013) and "Maya Express" (Budikova et al. 2010; Dirmeyer and Kinter 2009; Smith et al. 2013). Over the central US, the highest rainfall rates occur during the spring and summer coinciding with a seasonal maximum in convective activity (e.g., Dirmeyer and Kinter 2010; Villarini et al. 2011b), where elevated AR frequency is also evident (Fig. 3.1b,c). Consistent with Nakamura et al. (2013), a springtime maximum in the Ohio River Basin (Fig. 3.1b) supports the strong link between ARs and flooding across the region. Similarly, several studies have shown a strong connection between ARs and flooding across parts of the central US (e.g., Lavers and Villarini 2013; Nakamura et al. 2013). An example of a particularly high-impact and persistent AR event was the 1-2 May 2010 flood in Nashville, Tennessee (Moore et al. 2012). Although given considerably less attention in the literature, ARs occur across the seasonal cycle in the Northeast with a notable maximum in the fall, consistent with Hsu and Chen (2020) and the high AR precipitation fraction (AR contribution to total annual rainfall) noted in Lavers and Villarini (2015).

3.4.1.2 AR Magnitude and Direction

The seasonal distribution of mean IVT magnitude and direction at each grid cell for all AR days between 1981-2016 is shown in Fig. 3.2. An AR day is defined as any part of the identified AR object that is spatially collocated with that grid cell. Results reveal a seasonally consistent west-to-east gradient of AR IVT across the CONUS, with the exception of the immediate West Coast. Maxima in mean IVT during AR days are evident during the winter and fall in the PNW ranging between 400-450 kg m^{-1} s^{-1} along the Coast Range and Cascade Mountains of Oregon and Washington. For the Southwest, and more specifically coastal California and the Sierra Nevada, the mean IVT maximum occurs during the winter between 300-400 kg m^{-1} s^{-1}. Maxima in IVT magnitude for these regions is consistent with the seasonal distribution of AR occurrence in Fig. 3.2a-d. Lower IVT values across the western interior may be reflective of the influence of upwind topography, which acts to decrease the water vapor transport as an AR penetrates inland (Rutz et al. 2014). Elevation can also lead to reduced IVT magnitude since there is less atmosphere to integrate over and water vapor concentrations are much higher at lower elevations. Seasonal mean IVT direction across the West Coast is predominantly from the southwest. This follows the well-known horizontal moisture transport pathway from the sub-tropics to the extratropics that is sometimes referred to as the "Pineapple Express" when originating near Hawaii (Lackmann and Gyakum 1999; Dettinger 2011; Dettinger et al. 2011).

East of the Rocky Mountains, elevated IVT on AR days is extensive, revealing a pronounced line separating the eastern half of the country from the dry West. It is during the spring and summer over the Great Plains that the export of moisture from the tropics by way of the Gulf of Mexico is at a maximum (Knippertz and Wernli 2010), however elevated mean IVT is apparent in the fall as well. Moisture in this region is known to be transported from the Caribbean and Gulf of Mexico by way of the northern branch of the Caribbean LLJ, which feeds into the Great Plains LLJ (Mestas-Nuñez et al. 2007; Dirmeyer and Kinter 2010). This moisture transport pathway has been coined the "Maya Express," exhibiting a north-south orientation. While Fig. 3.2 does not show moisture transport upstream of the CONUS, this feature appears to be reflected among the mean IVT direction vectors for this region. During the summer in the Midwest, across the Mississippi Valley, mean IVT values >500 kg m^{-1} s^{-1} are evident (Fig. 3.2c). In connection with the Great Plains LLJ, ARs have been documented as transporting moisture into regions of deep convection or mesoscale convective systems (MCSs; e.g., Anderson and Arritt 2001), with recent examples documented in May/June 2008 in the U.S. Midwest (Budikova et al. 2010; Dirmeyer and Kinter 2009; Smith et al. 2013). Similarly, the Ohio River Valley, across Tennessee and Kentucky, reveals areas of high IVT, notably during the spring and fall at >500 kg m^{-1} s^{-1}. This region is affected by extratropical cyclones that travel eastward across the US, advecting moisture northward from the Gulf of Mexico (Lavers and Villarini 2015). The Appalachian Mountains are highlighted by decreased mean AR IVT values relative to the rest of the region, likely due to low-level moisture reduction through orographically enhanced precipitation (e.g.,

Smith et al. 2011) and higher elevation. Overall, IVT magnitude is considerably higher in the East compared to the West in all seasons, with the exception of the immediate coastal zones of the PNW in the fall and winter.

3.4.1.3 AR Area

The seasonal distribution of AR area is shown in Fig. 3.3. AR area is calculated as the median area for all ARs that have overlapped a grid cell. Median, as opposed to mean, values are used to limit the influence of outliers among the often non-normal AR area distributions. AR area has important implications for the spatial extent of associated impacts. During the winter, high values of AR area are prominent in the Northwest extending across the country from western Washington to eastern North Dakota with values $>6x10^6$ km^2. Although less frequent, high AR area values over the interior west likely represent large features that originate in the Pacific and penetrate inland (Fig. 3.3a). Some examples include the January 2010 AR event that penetrated eastward across the Pacific Ranges breaking hydrometeorological records across Arizona (Neiman et al. 2013; Hughes et al. 2014) and the November 2006 events that not only severely impacted Oregon and Washington but reached Glacier National Park, Montana causing extensive flooding (Neiman et al. 2008b; Rutz et al. 2014; Mueller et al. 2017). The signal of inland penetrating ARs over the western US is evident in the spring and fall as well (Fig. 3.3b,c). Results show that the largest ARs occur more commonly across the West compared to the East with an extensive portion of the Southwest and Southern Great

Plains experiencing ARs with a smaller areal extent (< $2x10^6$ km^2) during the summer (Fig. 3.3c).

3.4.2 AR Composites

To synthesize the spatial characteristics of the ARs in each region, seasonal composites of AR IVT magnitude and direction, along with AR axis density plots, for a major city in each of the seven NCA regions are shown in Figs. 3.4 (winter/fall) and 3.5 (summer/spring). Each composite represents the mean characteristics of AR IVT magnitude and direction at each grid cell for all AR days where the city was within the boundaries of an AR object (left side of Figs. 3.4,3.5a-n). AR axis density plots illustrate the cross-AR location of maximum IVT, showing the typical locations of the greatest AR intensity when an AR is affecting the city of interest for a given NCA region (right side of Figs. 3.4,3.5a-n). Following Guan and Waliser (2015), the AR axis is calculated by identifying the two grid cells on the boundary of the object to locate the maximum great circle distance. The arc is further divided into small segments equal to the number of grid cells between the outermost points. The great circle arc perpendicular to each segment is identified and, of the grid cells intersected by the arc, the one with maximum IVT is noted. The axis is defined by connecting the grid cells of maximum IVT.

3.4.2.1 Winter/Fall Composites

Winter/fall composite and axis density plots are shown in Fig. 3.4. Regions of composite IVT magnitude and direction for Portland, Oregon (OR), Los Angeles, California (CA),

and Rapid City, South Dakota (SD) during the winter reveal similar patterns of predominantly northeastward directed AR IVT from the Pacific Ocean (Fig. 3.4a-c), often associated with “Pineapple Express” type moisture transport. In the fall, IVT strength and direction is similar although the total number of AR days for each city is lower compared to the winter, with Los Angeles, CA and Rapid City, SD less than Portland, OR (Fig. 3.4h-j). Axis density plots show a relatively wide north-south swath of AR axes, roughly centered on both cities (Fig. 3.4a-c,h-j), with high axis density over the cities themselves. For all regions, we note that in some cases AR axes appear geographically removed from the city. This occurs when the AR object touches the city on one end but the bulk of the AR extends well away from the city. Axis density plots also reveal regions of maxima that are likely associated with local topography where IVT isn’t being depleted from orographic uplift. For example, high values of axis density are found along the Columbia River and Snake River Valleys in the Portland, OR composite (Fig. 3.4a).

The pattern of composite IVT magnitude for Rapid City, SD (Fig. 3.4c,j) demonstrates the importance of inland penetrating ARs. This occurs where lower or less consistent topographical barriers allow for high water vapor transport over the interior West, common during the cool season (Rutz et al. 2014). In contrast with typical moisture transport in the western US, eastern regions can experience corridors of strong water vapor transport that extend from multiple different moisture source regions, including the Gulf of Mexico, Caribbean Sea, and Atlantic Ocean (e.g., Pfahl et al. 2014). Composite

IVT analyses for Oklahoma City, Oklahoma (OK) show moisture transport over both the Pacific and Gulf of Mexico on AR days (Fig. 3.4d,k). Other cities across the eastern US, including Columbus, Ohio (OH), Augusta, Maine (ME), and Washington DC, reveal similar patterns of composite IVT magnitude and direction as well as axis density during the cold season with a relative high occurrence of AR days (Fig. 3.4e-n). Compared with western US, cities in the East tend to show a stronger northward component in IVT direction further indicative of differing patterns of water vapor transport. According to several studies, ARs with different IVT directions are known to produce different orographic precipitation distributions and hydrological impacts (e.g., Ralph et al. 2003; Neiman et al. 2011, 2013; Hughes et al. 2014; Hecht and Cordeira 2017). ARs in the East with a stronger northward component likely run parallel to the Appalachian Mountains, rather than orthogonal like along the West Coast, thus resulting in a different impact magnitude from orographic lifting. Rainfall may also result more from frontal lifting in the East compared with the predominance of orographic lifting in the West.

3.4.2.2 Summer/Spring Composites

Summer/spring composite and axis density plots are shown in Fig. 3.5. ARs along the West Coast are most common during the fall and winter, therefore AR day frequency and magnitude for Portland, OR and Los Angeles, CA in the spring and summer (Fig. 3.5a,b,h,i) is decreased relative to results in Fig. 3.4. In general, when ARs occur during spring/summer in these cities they continue to transport moisture directed predominantly northeastward, although with a decreased maximum in IVT magnitude relative to

winter/fall phenomena. IVT vectors directed northwest in southern California during the summer suggest ARs may occur alongside and include contribution from other meteorological mechanisms (e.g., North American Monsoon; Guan and Waliser 2017). Rapid City, SD displays a smaller spatial area of composite IVT, less suggestive of a predominant influence from inland penetrating ARs, as well as a stronger northward directed component in IVT direction (Fig. 3.5c,j). Similarly, Oklahoma City, OK shows seasonal maxima in the fall and spring, along with a north-south oriented band of high axis density extending from Texas to the Great Lakes in the spring (Fig. 3.5k). IVT composite results are consistent with studies that identify influence from "Maya Express" moisture transport which has been linked to a number of impactful flooding events across the central US (Moore et al. 2012; Lavers and Villarini 2013; Nakamura et al. 2013). A similar pattern of water vapor transport is shown in Columbus, OH during the spring (Fig. 3.5l) with a strong northward component in IVT direction. During summer/spring, ARs have been known to supply regions of deep convection across the central US with ample low-level moisture, resulting in heavy precipitation and flooding (Lavers and Villarini 2013). As for the East Coast, Augusta, ME and DC continue to show broad regions of elevated composite IVT throughout the spring and summer.

3.4.3 Linked AR Precipitation Characteristics

3.4.3.1 Fraction of AR Precipitation to Total Precipitation

The percent of climatological precipitation that falls on an AR day is shown in Fig. 3.6 for each season. An AR day is defined at a grid cell as any day where an AR object

spatially overlaps with the grid cell and all precipitation (>1mm) that falls on that day is considered AR precipitation. A value of 100% would indicate that all precipitation that falls at that grid cell is associated with an AR. Across the CONUS, regional and seasonal variability in AR precipitation is apparent. ARs explain ~30% of the precipitation in areas across the Northwest in the winter and fall (Fig. 3.6a,d). Across California, values show ARs are responsible for over 50% of precipitation during the fall and winter, consistent with Guan et al. (2010), Dettinger et al. (2011), and Gershunov et al. 2017. East of the Rocky Mountains, maxima in AR precipitation fractions are also apparent, notably in the Southeast and Midwest, during the winter, spring, and fall (Fig. 3.6a,b,d). Notable AR fractions in the Southeast show that ARs account for between 3055% of the total precipitation in the region. Several studies have demonstrated the importance of AR moisture in producing impactful precipitation across the Southeast, markedly during the winter and shoulder seasons, which is consistent with results shown here (e.g., Moore et al. 2012, Mahoney et al. 2016, Debbage et al. 2017). Summer stands out with notable low percentages suggesting that ARs are less influential in producing precipitation during these months, possibly because heavy precipitation here is often associated with localized convection and non-AR tropical disturbances (Fig. 3.6c). In the northeast, high AR precipitation fractions in the winter can be associated with impactful snowfall events, such as in the winter of 2009/2010 (Halverson and Rabenhorst, 2010). In general, ARs provide a substantial proportion of annual precipitation to many parts of the CONUS, however other mechanisms also play an important role, especially in the summer.

3.4.3.2 ARs and Extreme Precipitation

The seasonal distribution of the fraction of linked AR extreme precipitation days relative to the total number of extreme precipitation days, calculated at each grid cell, is shown in Fig. 3.7. A value of 100% indicates that all extreme precipitation days (defined in the methods section) at that grid cell were associated with an AR. ARs represent an important meteorological mechanism for generating wintertime precipitation extremes along the West Coast (Fig. 3.7a). They are associated with a majority of extreme precipitation days across much of California and the coastal zones of Oregon and Washington. During the winter ~8% of the Southwest had an extreme precipitation fraction >90% (Table S2.1). While ARs weaken as they propagate inland due to the precipitating out of low-level water vapor resulting from orographic lift, they also comprise a large proportion of extreme days for inland areas of the West during the winter and fall. For example, while Arizona has a relatively low AR frequency (Fig. 3.1), it has values between 70-100% indicating that when it does experience an extreme precipitation day it's often associated with an AR. These results are consistent with existing literature linking several impactful extreme precipitation days with AR conditions across the interior West (Rutz et al. 2012; Neiman et al. 2013; Hughes et al. 2014; Rivera et al. 2014).

Regions east of the Rocky Mountains also experience maxima in precipitation extremes associated with ARs. In the eastern and central US, AR fractions are highest in the winter, spring, and fall with several regions revealing notable maxima. For example, the

Ohio River Valley, specifically across the Tennessee and Kentucky border, reveals high AR extreme precipitation fractions during the winter and spring (Fig. 3.7a,b), with between 75-85% of extreme precipitation events concurrent with an AR. These results are consistent with Lavers and Villarini (2013) which identified ARs as a major flooding agent over the central US. The Southeast displays elevated AR extreme precipitation fractions during the non-summer months, consistent with Mahoney et al. (2016), where winter and spring events across the western portion of the region are linked to strong synoptic weather systems transporting water vapor from the Gulf of Mexico. During the winter ~7% of the Southeast region has extreme precipitation fractions >90% (Table S2.1). Although not all snowfall in the Northeast is associated with ARs, maxima in wintertime AR-driven precipitation extremes across this region may be associated with impactful snowstorms (Lavers and Villarini 2015).

The fraction of AR days with extreme precipitation relative to the total number of AR days at each grid cell is shown in Fig. 3.8, plotted as a percent. In other words, a value of 100% would indicate that all ARs are associated with an extreme precipitation day, as defined by the three-day total. The highest percentages are found across the West Coast and western mountains during the winter (Fig. 3.8a), although few places exceed 40%. This indicates that even where ARs are common, and a high percentage of extreme precipitation days are associated with an AR, many ARs occur without there being an extreme precipitation day. This result emphasizes that ARs are not always hazardous, and can be beneficial or simply benign when it comes to precipitation impacts (Corringham et

al. 2019). During the wintertime, the Rocky Mountains are visible with higher fractions on the west (windward) side of the range compared to the drier east (leeward) side, supporting the notion that this range is the second major topographic barrier encountered by landfalling ARs across the West (Fig. 3.8a).

The notably low AR fractions throughout the central US, stretching across the Northern and Southern Great Plains, indicate that ARs are rarely associated with extreme precipitation days, despite their frequent occurrence in some portions of the region. Results show ~10-20% of ARs are associated with extreme precipitation days across the eastern half of the US, with greater percentages, between 25-35%, across the Great Lakes and Ohio River Valley in the winter (Fig. 3.8a). In these regions, orographic lifting of AR moisture is minimal or non-existent, so other synoptic and mesoscale forcing (e.g., convection, frontal, isentropic lift) must play a role in AR-related precipitation intensity and duration. For example, Mahoney et al. (2016) identifies a number of precipitation triggering mechanisms working in conjunction with corridors of water vapor transport linked to heavy precipitation over the southeastern US, including synoptic scale frontal systems, landfalling tropical cyclones, MCS's, and orographic lifting over the Appalachian Mountains. Linked AR extreme precipitation fractions clearly demonstrate the importance of ARs as a mechanism for heavy precipitation in many portions of the CONUS, including across the East.

3.4.4 NCA Region Summaries

3.4.4.1 Seasonal and Regional Distribution of AR Magnitude, Area, and Direction

Annual distributions of AR magnitude, direction, and area are shown for each of the seven NCA regions (Fig.2.2) in the histograms in Fig. 3.9. ARs in each region must have at least 10% of their grid cells within the region bounds to be counted in the histogram. AR IVT magnitude reveals a distribution with a slightly longer right-tail in regions across the western half of the country, including the Northwest (skewness of 0.90), Southwest (skewness of 0.80), and Northern (skewness of 0.51)/Southern Great Plains (skewness of 0.28; Fig. 3.9a-d), and close to normal or symmetric distributions among regions in the East (Fig. 3.9e-g). In general, western sub-regions tend to have lower median IVT magnitudes compared to the East. The Northeast has the highest median IVT magnitude at ~413 kg m^{-1} s^{-1} (Fig. 3.9f). The seasonal distribution of AR IVT magnitude shows western sub-regions with maxima during the winter (Fig.S2.2a-d) and the eastern regions during the summer (Fig. S2.4e-g). Across all seven NCA regions, AR area has a positively skewed distribution with skewness values ranging between 1.25-1.77 and all regions revealing a median area between 0.18-0.23x10^7 km^2 (Fig. 3.9h-n). The Northwest and Northeast share the highest median area of 0.23x10^7 km^2 (Fig. 3.9h,m). The seasonal spread of AR area continues to show positively skewed distributions with all seven regions experiencing the largest ARs during the winter months, with medians between ~0.25-0.35x10^7 km^2 (Fig S2.2h-n). AR IVT is consistently directed in the northeastward direction, with median IVT direction for all regions ranging between ~50°-58° (with 0° due North; Fig.2.9o-u). All regions indicate that AR IVT typically has a stronger

eastward than poleward component and ARs with a westward component are rare, consistent with Guan and Waliser (2015). Seasonally, western regions experience the most eastward directed ARs during the winter (Fig.S2.2a-d), while eastern regions reveal a higher occurrence of north/northeastward directed ARs, suggesting influence from southern moisture sources, such as the of Gulf of Mexico.

3.4.4.2 NCA Region Summary of AR Characteristics

AR characteristics, as described at the grid point scale above, are summarized over the seven NCA regions in Figure 3.10 and reported in Table 3.1. Here, region shading provides a measure of AR frequency and arrow size, direction, and color refers to median AR IVT magnitude, direction, and area, respectively. AR frequency for a given NCA region is normalized by area (i.e., number of AR days per 10,000 km^2) to account for differences in region size. ARs in each region are again identified under the condition that at least 10% of the grid cells of the AR object are within the region boundaries. Results show that the largest area (arrow color) and magnitude (arrow length) ARs occur in the winter and fall in the Northwest and Southwest, which is consistent with earlier results at the grid point scale (Figs. 3.2a,4a). ARs during the winter in the Northern Great Plains also tend to have the largest area, likely related to cool season inland penetrating ARs originating over the Pacific Ocean, which must be relatively large in order to reach such an area. These three regions also experience ARs with similar median IVT directions, ~60° or northeastward, during the winter (Fig. 2.10a; Table 3.1). During the spring and summer ARs in the West tend to have a smaller areal extent, between 1-

$2.5x10^6$ km^2, and magnitude, between 200-250 kg m^{-1} s^{-1} (Fig. 3.10b,c). In the Southern Great Plains, AR frequency and magnitude are highest in the spring and summer. Springtime ARs in this region tend to be directed more north/northeastward, relative to other seasons, with a median IVT direction of ~46° (Table 3.1). The Midwest has similarly directed ARs, experiencing its highest magnitude ARs in the summer and fall (Fig. 3.10c,d). The Northeast reveals notable maxima in AR frequency and magnitude, compared with the rest of the country, across the seasonal cycle. During the winter and fall, ARs in the Southeast are relatively larger in areal extent, between $2\text{-}2.5x10^6$ km^2 (Fig 3.10d), with little seasonal variation in magnitude. Although useful in summarizing AR characteristics over the NCA regions, in some cases summarized characteristics may mask sub-regional scale variations, for example those induced by topographic barriers.

3.4.4.3 NCA Region Summary of AR Precipitation

Seasonally and regionally summarized AR precipitation characteristics are illustrated in Fig. 3.11 and recorded in Table 3.2. Here, region shading (green) refers to extreme precipitation day frequency, calculated as the spatial median of the total number of qualifying days experienced by the region over the study period. Each region has an illustrated bucket depicted with a water level, white bar, and gray bar. The water level refers to the median fraction of AR precipitation or the amount of precipitation that fell on AR days relative to the total precipitation amount. The white bar refers to the median extreme precipitation fraction, or the number of linked AR extreme precipitation days relative to the total extreme precipitation day frequency. The gray bar refers to the

median AR fraction or the number of linked AR extreme precipitation days relative to the total AR day frequency.

Results show that the Northwest experiences the greatest number of extreme precipitation days during the winter and spring (Fig. 3.11a,b). In the winter, ARs are responsible for ~25% of the total precipitation received in the region with close to 75% of the extreme precipitation days related to an AR (Table 3.2). The Southwest also shows a maximum in the fraction of AR precipitation extremes in the winter (Fig. 3.11a), with 66% of all precipitation days linked to ARs and ~15% of the ARs in the region resulting in an extreme (Table 3.2). Only a small proportion, between 5-10%, of the total precipitation experienced in the Northern Great Plains is attributable to ARs across the seasonal cycle. In the Southern Great Plains, results show that ARs play an important role with the highest number of extreme precipitation days occurring in the spring and summer (Fig. 3.11b,c) and over 50% of the extreme precipitation days related to an AR (Table 3.2) in the spring. Likewise, the Midwest shares extreme precipitation day maxima in the spring and summer. During these months ARs explain between 50-55% of the extreme precipitation days and >20% of the total precipitation experienced by the region. The Northeast has a relatively high occurrence of extreme precipitation days across the seasonal cycle, accounting for the most precipitation during the fall and winter (Fig. 3.11a,d), in some cases related to impactful snow storms experienced by the region. Consistent with Mahoney et. al (2016), ARs are more influential in the Southeast during

the cool/transition season months (fall-spring; Fig. 3.11a,b,d) where ARs are linked to between 70-80% of the extreme precipitation days (Table 3.2).

3.5 Summary and Conclusions

In the Fourth NCA CSSR, ARs were identified as a key topic in its chapter on "Extreme Storms," focused primarily on the US West Coast. However, research has shown that ARs frequently occur and impact many regions across the CONUS. To expand our understanding and documentation of regional AR impacts, we consistently apply an objective AR detection algorithm to global reanalysis to provide a fine-scale pointwise and regionally aggregated annual and seasonal understanding of AR frequency, physical characteristics, and impacts across the CONUS summarized over the seven NCA regions. AR detection is based on IVT magnitude thresholds, as well as a number of geometric and directional criteria following the technique described in Guan and Waliser (2015) and updated in Guan et al. (2018).

Seasonal climatologies of AR frequency across the CONUS reveal ARs in the Northwest and Southwest are most common in the winter and fall (Fig. 3.1a,d). Although considerably less widely studied, AR occurrence east of the Rocky Mountains is observable across the seasonal cycle with notable maxima across the Southeast in the winter and in the central US Mississippi River Basin during the summer and shoulder seasons (Fig. 3.1b-d). Mean IVT magnitude and direction results illustrate the influence of the mountainous coastal terrain across the West acting as a barrier reducing water

vapor transport as ARs penetrate inland (Fig 3.2a). Generally higher levels of background moisture and a more diverse array of precipitation triggering mechanisms in the East likely explain differences in AR occurrence and associated impacts compared to the West. Even with a generally drier background environment, the largest area ARs occur in the interior western US (>$4.5x10^6$ km^2) demonstrating a strong signature of large features penetrating inland from the Pacific Ocean across the interior during the winter (Fig. 3.3a).

Seasonal patterns of water vapor transport during AR days for major cities across the seven NCA sub-regions were identified based on AR axis density plots and an IVT composite analysis (Figs. 3.4,3.5). Western cities reveal predominantly northeastward directed IVT influenced by moisture transported from the tropical pacific indicative of the well-known "Pineapple Express" phenomenon (Fig. 3.4 a-c). Cities in the East show seasonally varying patterns of water vapor transport. Notable north-south oriented bands of moisture were apparent among AR axis density plots for cities across the central US in the spring (Fig. 3.5k,l), consistent with literature identifying "Maya Express" moisture transport fueling the Great Plains LLJ.

Objectively identified ARs were further linked with high resolution precipitation measurements to examine the relationship between ARs and precipitation across the CONUS. Results show that ARs explain ~30% of the precipitation in areas across the Northwest and ~50% of the precipitation over parts of California during the fall and winter (Fig. 3.6a,b). Across the Midwest and Southeast, maxima in the ratio of AR

precipitation to total precipitation are evident during the winter and shoulder seasons (Fig. 3.6a,b,d). The seasonality of linked AR extreme precipitation days in the western and eastern US has also been shown to starkly differ, with winter/fall (Fig. 3.7a,b) days being markedly more prominent in the West and summer/spring (Fig. 3.7b,c) days dominant in the eastern and central US. The fraction of linked AR extreme precipitation days relative to the total amount of ARs days revealed higher and more variable fractions west of the Rocky Mountains compared to areas to the east, likely related to the regional differences in precipitation triggering mechanisms (Fig. 3.8).

Regionally aggregated AR IVT and precipitation characteristics are summarized across the seven NCA regions in Figs. 3.9-3.11. Histograms of the distribution of three basic AR characteristics, including IVT magnitude, direction, and area, reveal regional variations in distribution shape and median values. Higher values of median IVT magnitude are apparent in the East compared to the West (Fig. 3.9a-g), while both the Northwest and Northeast reveal maxima in AR area (Fig. 3.9h,m). All regions indicate that AR IVT typically has a stronger eastward than poleward component, with a rare occurrence of ARs with a westward component (Fig. 3.9o-u). Regionally aggregated statistics for AR characteristics show seasonal variability in AR size, strength, direction, and frequency (Fig. 3.10). Similarly, regionally summarized AR precipitation statistics highlight the importance of ARs in fueling precipitation extremes across the US (Fig. 3.11).

Two caveats should be considered when interpreting results from this climatology. The first is choice of dataset and the second is choice of detection algorithm. While MERRA-2 has been used extensively for AR detection in recent literature (Guan and Waliser 2017; Lora et al. 2017; Mundhenk et al. 2018; Shields et al. 2018), results could vary slightly with use of a different reanalysis but are not expected to change the conclusions of this paper (Guan and Waliser 2015, 2017, 2019; Guan et al. 2018). The detection algorithm applied here is based on a well-documented approach, however sensitivity of results to algorithm choice, although beyond the scope of this current study, would add robustness to this climatology (e.g., Shields et al. 2018; Rutz et al. 2019). The detection algorithm also cannot identify AR-linked phenomena, meaning that although the physical interpretation of an AR across regions may differ, for example an extratropical cyclone in a Northwest AR versus the Great Plains LLJ in Midwest ARs, the method is unable to objectively account for it.

The results of this study can be leveraged in two ways. First, the results can be used as a benchmark for considering how climate change may affect AR features and impacts. Second, observed AR characteristics can be used to evaluate the performance of climate models at simulating the seasonality and regional distribution of AR characteristics and precipitation extremes across the CONUS. Ultimately, this study yields insight into the fundamental importance of ARs in the hydroclimate of the CONUS and how that importance varies by region.

Chapter 4: Assessment of Projected Climate Change Effects on Atmospheric Rivers and Associated Precipitation in CMIP6 Models for the Seven US National Climate Assessment Regions

Abstract

A uniform regional approach across the contiguous United States (CONUS) is used to quantify how atmospheric rivers (ARs) change between Coupled Model Intercomparison Project Phase 6 (CMIP6) historical simulations and future projections under the Shared Socioeconomic Pathway (SSP) 585 warming scenario. An objective AR detection algorithm, using percentile-based integrated water vapor transport (IVT) thresholding defined in the historical climate, is applied to CMIP6 to characterize climate change impacts on AR frequency, geometry, intensity, and associated precipitation. Future changes in AR characteristics and associated precipitation are computed at the grid point scale and summarized over the seven US National Climate Assessment (NCA) regions across the CONUS. End of the century (2071-2100) projections indicate increases of up to ~11 more AR days per season regionally, notably across the West in the winter, central and southeastern US in the spring, parts of the East in the summer, and Pacific Northwest and interior West in the fall. AR IVT magnitude shows notable increases of up to ~55 kg m^{-1} s^{-1} across parts of the western and eastern US, with little future change in mean AR IVT direction regionally. Projected change in AR linked precipitation indicates ARs will be responsible for a larger proportion, up to +20% seasonally, of total climatological precipitation in most regions by the end of the century. AR days linked with extreme precipitation days are projected to make up a greater majority of total extreme precipitation day occurrence of up to +30% seasonally, notably across the West in the

winter and Midwest in the spring and fall. Results from this study aim to inform the continued efforts of the NCA concerning anticipated changes in weather and hydrology extremes across the CONUS.

4.1 Introduction

An extensive and growing body of literature (Ralph et al. 2020 and references therein) has highlighted the significance of atmospheric rivers (ARs) within the global water cycle (Zhu and Newell 1998; Newman et al. 2012) as well as to the occurrence and modulation of hydrometeorological extremes (Ralph et al. 2006; Rutz et al. 2014; Lavers et al. 2011; Viale and Nuñez 2011; Warner et al. 2012; Moore at al. 2012). Projections of extreme precipitation intensification across the globe are strongly linked to increases in atmospheric water vapor with warming at the rate of Clausius Clapeyron scaling, about 7% ($°C^{-1}$) (Wehner et al. 2013; Kunkel et al. 2013s, 2013b). This robust thermodynamic response of atmospheric moisture has the potential to alter AR frequency, strength, precipitation, and associated hydrological extremes in the future (Hagos et al. 2016; Mahoney et al. 2018; Singh et al. 2018; Curry et al. 2019). With change likely already underway, a robust understanding of model fidelity and future projections of AR precipitation extremes at regional scales is of the upmost importance.

ARs are long, narrow filamentary corridors of strong horizontal water vapor transport (Zhu and Newell 1994, 1998), influential to the hydroclimate of a number of regions in the mid-latitudes. ARs have an established influence on regional precipitation extremes

and associated impacts throughout the contiguous United States (CONUS; as shown in *Chapter 3* and Slinskey et al. 2020), including across the West Coast (Neiman et al. 2008a; Guan et al. 2010; Dettinger et al. 2011; Ralph and Dettinger 2012; Lamjiri et al. 2017), interior west (Rutz et al. 2012, 2014, 2015; Neiman et al. 2013; Hughes et al 2014; Rivera et al. 2014); Northwest (Neiman et al. 2008b, 2011; Collow et al. 2020), central/Midwest (Lavers and Villarini 2013; Rabinowitz et al. 2018), and Southeast (Moore et al. 2012; Mahoney et al. 2016; Debbage et al. 2017; Miller et al. 2018;). Elsewhere AR-like features and conditions have also been identified and linked with impactful precipitation (Businger et al. 1990; Budikova et al. 2010; Letkewicz and Parker 2010; Pfahl and Wernli 2012; Pfahl et al. 2014), for example "tropical moisture feeds" (Howarth et al. 2019) and anomalous water vapor flux (Teale and Robinson et al. 2020) in the Northeast.

Despite the key role ARs play in global water and energy cycles and their influence on regional precipitation distribution and extremes, only a limited number of studies have evaluated AR representation among global climate models (GCMs). Of the existing AR modeling studies, few have been diagnostic and scrutinized the details of processes, such as those associated with water budgets; cloud, convection, and latent heat processes; or meso-scale circulations (Waliser and Cordeira 2020). Several studies investigating the ability of climate models to realistically simulate ARs and associated precipitation found that Coupled Model Intercomparison Project Phase 5 (CMIP5) models produce the large-scale weather patterns associated with ARs reasonably well (Payne and Magnusdottir

2015, Gao and Leung 2016, Ramos et al. 2016, Warner and Mass 2017). AR response to warming has been found to hinge on several key factors at the root of biases, including model physics, dynamical core, and resolution which can vary from model to model (Wick et al. 2013; Hagos et al. 2015; Guan and Waliser 2017). A more recent study (Norris et al. 2021), evaluated extreme precipitation days over California using 28 CMIP6 models, finding models underestimate the magnitude of integrated water vapor transport (IVT; a measure of AR intensity) associated with extreme precipitation. The varying degrees of uncertainty associated with AR representation within GCMs can be used to guide interpretations of projected change in the future.

A number of studies have assessed the degree to which ARs and associated impacts will change under warming across the West Coast (Dettinger 2011; Gao et al. 2015; Hagos et al. 2016; Payne & Magnusdottir 2015; Radić et al. 2015; Shields and Kiehl 2016a, 2016b; Warner et al. 2015; Gershunov et al. 2019), Europe (Gao and Leung 2016; Lavers et al. 2013; Ramos et al. 2016; Shields and Kiehl, 2016a), and globally (Espinoza et al. 2018). The majority of the above studies used CMIP5 to identify change in AR characteristics, including intensity, frequency, geometry, and location. Across North America, studies show an increasing trend in the frequency and intensity of AR days in future climates, with Gao and Leung (2016), Ramos et al. (2016), and Shields et al. (2016) finding that ARs will comprise an increasing share of extreme precipitation in some regions. However, disagreement around changes in CMIP5 simulated AR seasonality and regional patterns of AR frequency remains among existing work (Payne

and Magnusdoittir 2015, Lavers et al. 2015, Warner and Mass 2015). In a global analysis, Espinoza et al. (2018) found an increase of ~50% in AR conditions, supported by ~25% increase in AR length, width, and strength. Given the importance of ARs in determining water vapor and precipitation distribution, along with the character and pattern of extreme precipitation, a uniform CONUS-wide analysis of the projected effect of climate change on ARs with regional specificity is warranted.

In this study, the latest suite of state-of-the-art GCMs from the CMIP6 database are used to assess change in the regional climatology of AR characteristics and associated precipitation across the CONUS. A global, objective AR detection algorithm (Guan and Waliser 2015; Guan et al. 2018) is applied to five CMIP6 models to evaluate change in AR day frequency, geometry, and IVT characteristics. To assess the effect of climate change on AR impacts, the contribution of ARs to projected changes in precipitation characteristics and extreme precipitation frequency is quantified. All metrics are calculated at each grid point and summarized over the seven US National Climate Assessment (NCA) regions across the CONUS (Fig. 2.2).

4.2 Data and Methodology

CMIP6 (Eyring et al. 2016) is used to identify ARs and associated precipitation among the historical period (1984-2013) and mid- (2036-2065) and end-of-century (2071-2100) projections under the Shared Socioeconomic Pathway (SSP) 585, also referred to as the high-end emissions warming scenario. The SSP-585 scenario updates the Representative

Concentration Pathway (RCP) 8.5 from CMIP5 (O'Neill et al. 2016). IVT values are constructed using daily values of 3-D wind and water vapor, and monthly surface pressure at all available pressure levels, including 1000, 850, 700, 500, and 250 hPa, extending to the surface. Five CMIP6 models, limited by the model output availability necessary for calculating IVT, are used in this analysis and are detailed in Table 4.1. Only the first ensemble member from each model is used for the historical and SSP-585 projections. Model output is interpolated to a uniform 1° lat-lon grid following the IVT calculation but prior to the analysis detailed in Sections 4.2.1 and 4.2.2. Daily precipitation model output is used to link identified AR days with associated precipitation. The CMIP6 data are available from the Earth System Grid Federation (ESGF) archive (https://esgf-node.llnl.gov/search/cmip6/).

4.2.1 Objective AR Detection Algorithm

The global AR detection algorithm introduced in Guan and Waliser (2015), and updated in Guan et al. (2018), is used to identify AR days among model historical simulations and future projections. The approach combines a multiple, sequential percentile-based technique (i.e., 85^{th}-95^{th} percentile of geographically and seasonally dependent climatological IVT) with a minimum IVT threshold (100 kg m^{-1} s^{-1}), to identify contiguous features characterized by anomalous water vapor transport. To ensure coherence, more than half of the area of the AR must share consistency in direction (within 45°) with the overall mean IVT direction, in addition to an appreciable poleward component (>50 kg m^{-1} s^{-1}). The method requires an AR be ≥2000 km in length and have

a length/width ratio ≥ 2. This technique has facilitated a consistent examination of basic AR characteristics on a global scale in a number of studies involving AR climatology and variability, global model evaluation (Guan and Waliser 2017), AR-related extreme events (Waliser and Guan 2017), and the effect of climate change on ARs (Espinoza et al. 2018). For this analysis, IVT thresholding is defined based on the historical simulation and applied to future projections to identify ARs within each individual model. While using historical-based thresholding offers an understanding for potential change in AR-features based on the current climate, ARs defined using future thresholds would likely have higher IVT magnitude percentiles, generating a lower number of AR days during the future period than shown here.

4.2.2 Linked AR Extreme Precipitation

Extreme precipitation days are defined as exceedances of 95th percentile non-zero three-day precipitation totals calculated at each grid point (consistent with *Chapter 3* and Slinskey et al. 2020). The use of a percentile-based threshold ensures consideration of the local climatology when defining extremes. Each three-day total includes the sum of that day and the previous two (as in *Chapter 2,3* and Slinskey et al. 2019, 2020). Multi-day totals have been shown to better capture some heavy precipitation impacts while also reducing uncertainty due to temporal mismatch among data products (Ralph and Dettinger 2012). Herein, qualifying three-day totals are referred to as extreme precipitation days. Linked AR extreme precipitation days occur when at least one AR day is present during a precipitation extreme's three-day window.

4.3 Results

4.3.1 Historical Simulations

AR frequency (days/season) is calculated at each grid point, as the number of days when a given grid point is within the boundary of an AR, for the historical period (1984-2013) in Fig. 4.1. Results are shown for MERRA-2 (Fig.4.1a-d), the reference, and the historical simulation multi-model mean (Fig. 4.1e-h) for the 5 CMIP6 models included in this analysis (Table 4.1). Comparison of MERRA-2 and the multi-model mean reveals AR day frequency patterns are reasonably well-represented in the CMIP6 models, lending confidence to their ability to reproduce the principle spatial patterns of AR climatology. Notable positive AR day frequency biases are visible across the West in DJF, MAM, and SON (Fig.4.1e,f,h). Across the East, positive frequency biases are visible in the Southeast in the MAM and JJA (Fig.4.1f,g), while over parts of the Northeast and Midwest moderate negative frequency biases occur in DJF and MAM (Fig. 4.1e,f), respectively.

Model evaluation of additional AR characteristics across the CONUS have shown that AR IVT biases among CMIP6 models tend to be negative, with most regions and seasons below 10% (Gonzalez-Hirshfeld et al. 2021). Results also show high positive AR area biases across all seasons and regions, suggesting low confidence in CMIP6 model ability to accurately capture this metric. Simulated linked AR extreme precipitation metrics tend to agree well with observations in most regions, excluding areas of complex terrain,

signifying possible model constraints in resolving orographic precipitation processes. Overall, biases across variables suggest the historically simulated multi-model mean is a reasonable representation of the observational reference, with regional and seasonal variability among biases for different AR characteristics.

4.3.2 Projected Change in AR Characteristics

4.3.2.1 AR Day Frequency

Multi-model mean AR day frequency (days/season) is calculated at each grid point and shown for the historical simulation period, mid- and end-of-century projections, and change across the seasonal cycle in Fig. 4.2. Results show an increase in the number of AR days consistently across all seasons and regions, to varying degrees, by the end of the century (Fig. 4.2q-t). End-of-century change generally follows the patterns of mid-century change (Fig. 4.2m-p) except with a greater magnitude. Across the West, end-of-century AR day frequency maxima are most prominent in SON (Fig. 4.2l), with regionally aggregated increases of ~10 more AR days in the Northwest and Northern Great Plains and ~7 more AR days in the Southwest. End-of-century AR day occurrence in the interior West may be related to projected increases in inland penetrating ARs along the West Coast (Mahoney et al. 2018).

East of the Rocky Mountains, projections show the most AR days occurring in winter across the Southeast (Fig. 4.2i), throughout the Mississippi River Basin and Ohio River Valley in MAM (Fig. 4.2j), and across parts of the Midwest in SON (Fig. 4.2l). Increases

in AR days in the Central US and Great Plains in MAM, follow expectations of projected change in another major mechanism for moisture transport in the region, the Great Plains low-level jet (LLJ), which is projected to increase in the southern plains in the spring and in the central plains in the summer (Tang et al. 2017). The seasonal distribution of AR day frequency maxima generally mimics the historical patterns (Fig. 4.2a-d), suggesting that regions across the East that have shown a relatively high count of AR days in the past will receive more by the end of the century. The Northeast shows notable increases in the MAM, JJA, and SON (Fig. 4.2r-t) with ~6-7 more AR days projected regionally in the future (Fig. 4.2v-y).

4.3.2.2 AR Magnitude and Direction

As a measure of AR strength, multi-model mean AR IVT magnitude and direction is shown for the historical simulation and future projection periods in Fig. 4.3a-l. Change, or the difference between the future projection and historical simulation, in AR IVT magnitude is shown for the mid-century, end-of-century, and regionally aggregated end-of-century in Fig 4.3m-y. Mean AR IVT magnitude is calculated at each grid point as the average IVT value across all days detected as an AR. Change in IVT direction was found to be negligible, with little to no change by the end of the century, and therefore was left out of Fig. 4.3m-y.

Among the historical simulation (Fig. 4.3a-d), results show a large geographical stretch of the eastern US with IVT magnitude values ranging from 450-550 kg m^{-1} s^{-1} across the

seasonal cycle, while along the West Coast elevated values tend to occur in DJF and SON, generally delineated by the Coast Range and Cascade Mountains. As with AR frequency, end-of-century change in IVT magnitude (Fig. 4.3m-p) generally follows mid-century change (Fig. 4.3q-t) at a higher magnitude. Regional change across the West Coast shows an increase of ~24 kg m^{-1} s^{-1} in the Southwest, mainly occurring in California (Fig. 4.3q), in DJF (Fig. 4.3u) and ~37 kg m^{-1} s^{-1} in the Northwest in SON (Fig. 4.3y) by the end of the century. These results are generally consistent with existing literature finding dramatic AR IVT increases along the West Coast with warming (e.g., Warner et al. 2015). In the Southeast in DJF, MAM, and SON, AR IVT magnitude increases by >30 kg m^{-1} s^{-1} across the region (Fig. 4.3u,v,y). The greatest regional change, relative to the historical simulation, in IVT magnitude on AR days occurs in the Northeast with an increase of around ~42 kg m^{-1} s^{-1} in MAM and SON (Fig. 4.3v,y).

4.3.2.3 AR Area

The seasonal distribution of projected change in AR area, calculated at each grid point as the median area of all collocated AR objects, is shown in Fig. 4.4. Projected change in AR area has the potential for important implications regarding the spatial extent of associated impacts as well as the number of detected AR days in the future. In the historical simulation, the largest ARs occur in DJF (Fig. 4.4a), with smaller ARs evident in MAM and JJA. Projections of change by the end of the century are consistently positive across all regions and seasons (Fig. 4.4m-t). In the end-of-century period in DJF, maxima in AR area values are broad, extending from western Washington to Wisconsin

with values ranging between 7.5-8.5 $x10^6$ km^2 magnifying mid-century change (Fig. 4.4i). High AR area values persist across the northern half of the country and interior west across the seasonal cycle, specifically in SON with regional increases of 3.8 $x10^6$ km^2 in the Northwest and 3.5 $x10^6$ km^2 in the Northern Great Plains (Fig. 4.4y). The eastern half of the country, notably the Northeast and Southeast, generally experiences ARs with a smaller areal extent compared to the West, although change by the end of the century remains positive, generally between ~2-3 $x10^6$ km^2.

4.3.3 Projected Change in Linked AR Precipitation Characteristics

4.3.3.1 Proportion of AR Precipitation to Total Precipitation

Projected change in the percent of climatological precipitation (>1mm) that falls on a detected AR day, defined at each grid point when any part of an identified AR object is spatially collocated with that grid point, is shown in Fig. 4.5. For context, a value of 100% would indicate that all the precipitation recorded at a grid point was associated with an AR. Across the seasonal cycle, among the historical simulation (Fig. 4.5a-d), ARs are responsible for a higher percentage of total precipitation during DJF, MAM, and SON, leaving JJA with generally lower values consistent with lower AR day occurrence during this season (Fig. 4.5c). In the West, historical simulations reveal ARs are responsible for 50-60% of the total precipitation along the West Coast in DJF and SON (Fig. 4.51a,d). Historic maxima in AR-driven precipitation occur in the Northeast in DJF and SON at ~35-40% (Fig. 4.5a,d), while in the Southeast values vary seasonally at

around at ~35% in MAM and ~45-50% in DJF across the Ohio River Valley in SON (Fig. 4.5b,d).

By the end of the century, increases in AR-related precipitation are visible across most regions (Fig. 4.5 i-l). In the Northwest and Southwest, ~45-55% of precipitation is AR-related in DJF and SON, with ~70% AR-related in California in DJF, MAM, and SON (Fig. 4.5 i,j,l). Across the East, values approaching 60% are visible in the Southeast in SON and MAM, in the Ohio River Valley in SON, and in the Northeast in DJF and SON (Fig. 4.5 i,j,l). Regional change is highest in MAM in the Midwest and Northeast at +16% and in SON in the Northwest at +17% and Northeast at +15%. Generally, results show positive projected change in the fraction across regions and seasons by the end of the century, suggesting future ARs will be responsible for a larger proportion of the seasonal precipitation that falls CONUS-wide. The notable decrease in AR-driven precipitation visible in southern California in JJA (Fig. 4.5o,s), suggests ARs are projected to make up a smaller fraction of precipitation during these months, possibly signifying an increased role by other mechanisms. This change may be related to influence by monsoon-driven convection, which has been documented as impactful to warm season precipitation in this region (Higgins et al. 1997).

4.3.3.2 ARs and Extreme Precipitation

Figure 4.6 shows the seasonal distribution of projected change in the fraction (%) of linked AR extreme precipitation days relative to the total number of extreme precipitation

days calculated at each grid point. Here a value of 100% indicates that all of the extreme precipitation days (defined in section 4.2.2) captured at a grid point are associated with an AR. In DJF the western US, a region that has historically experienced a large proportion of AR-driven precipitation extremes (Fig. 4.6a), maintains high values ranging between 90-100% among the mid- and end-of-century projections (Fig. 4.6e,i). This could be related to changes in the occurrence of inland penetrating ARs. In a study by Mahoney et al. (2018), marked increases in inland precipitation were documented through stronger, deeper moisture transport penetrating the Coastal and Cascade Mountains of Oregon and 'spilling over' into the Snake River Valley fueling orographic precipitation in the Sawtooth Mountains. Elevated values in the future are also visible along the West Coast in MAM and interior West in SON (Fig. 4.6j,l), further illustrated by the dissipating signature of the Sierra Nevada, suggesting reduced orographic efficiency in the future (Siler and Roe et al. 2014). This is especially evident among projected change values in the Northern Great Plains region in MAM, JJA, and SON (Fig. 4.6r-t). Although at relatively lower percentages overall, compared to other regions, results show the region experiencing some of the largest relative increases at ~20% in these seasons (Fig. 4.6v-y).

Increased AR-driven extreme precipitation in the future is also evident across regions in the East. A larger proportion of extreme precipitation days are associated with ARs in the Midwest and Northeast in MAM (Fig. 4.6r). Although ARs make up a considerable proportion of extremes across the Southeast in DJF, MAM, and SON (Fig. 4.6a,b,d), the

region is projected to experience some of the lowest values of change, between +4-8% across the seasonal cycle. Parts of the central US also tend to experience a lower proportion of extremes linked to ARs relative to the other regions, however projections of change are consistently positive across the region. Overall, results indicate ARs will contribute to a larger proportion of extreme precipitation days across many parts of the CONUS by the end of the 21st century, suggesting a possible diminished role by other meteorological mechanisms.

The seasonal distribution of the fraction of linked AR extreme precipitation days relative to the total number of AR days and associated projected change is shown in Fig 4.7. Here a value of 100% would indicate that all AR days detected at a grid point were associated with an extreme precipitation day. It's important to note that when interpreting this metric, the use of a percentile based threshold (i.e., 95th) for defining multi-day extreme precipitation, limits the number of extreme precipitation days possible (i.e., top 5% of days for each season over the 30-yr climatology). This combined with a relatively larger number of AR days (having been detected using a different set of percentile-based thresholds) will necessarily produce lower percentages than previously shown in the extreme precipitation fraction.

Historically, the highest percentages are visible across the West, specifically along the coast and western mountain ranges, with values between 30 and 40% during some seasons (Fig. 4.7a-d). By the end of the century, the fraction of linked days to AR days

across the West lessens by ~5-6% in the Northwest and Southwest (Fig. 4.7u-y), suggesting that a number of AR days will occur without a precipitation extreme. This result emphasizes that ARs are not always hazardous and can be beneficial or benign when it comes to precipitation impacts. The signature of the Rocky Mountains is visible throughout most seasons among both the historical simulation and future projections, revealing higher fractions along the windward side of the range and relatively lower fractions on the leeward side. While this supports the concept of the Rockies as the second major topographic barrier encountered by ARs in the West, projections generally show the central US with the only positive change, suggesting future ARs may penetrate complex terrain and cause impactful precipitation on the leeward side of the range. Fractions in the East are generally lower compared to the West, indicating that ARs in the East are less likely to be associated with a precipitation extreme than those in the West. This result likely speaks to the diverse range of precipitation triggering mechanisms (e.g., convective or frontal lift) in the East, compared to the West. However, end-of-century change in the East is consistent with the West (Fig. 4.7q-t), indicating a smaller proportion of linked days to AR days. Regional aggregates further show a notable consistent decrease in the Southeast at ~4% across all seasons by the end of the 21st century (Fig. 4.7u-y).

For better interpretation of the decreased end-of-century change shown here, it's important to note that increases in the number of AR days in the future are evident (shown in Fig. 4.2). With 95th percentile extreme precipitation thresholds defined in the

future, even if all possible extreme precipitation days are associated with an AR, there are likely to be more projected AR days than extreme precipitation days, generating a lower proportion of linked days to AR days. Negative change could result from changes in the linked AR extreme precipitation days contributing to this fraction, warranting additional analysis to fully understand potential implications of the results. Even with a robust understanding of IVT and the CC relationship under warming signifying a higher moisture content in future ARs, a number of other factors could have implications on AR-precipitation characteristics in the future necessitating deeper analysis in future AR impacts studies.

4.3.4 NCA Region Summaries

4.3.4.1 Inter-model Comparison of Regional and Seasonal Distributions of AR Size and Strength

As a means of comparing individual model output among projected change in the AR characteristics shown at the grid point scale in Figs. 4.3 and 4.4, individual model boxplots representing the seasonal distribution of AR magnitude and AR area, for each of the seven NCA regions, are shown in Figs. 4.8 and 4.9. Each figure contains 4 panels (rows) corresponding to a different season, with varying colors for distinction between regions (columns). Model names are labeled along the horizontal axis. Each region's colored boxplots show the end-of-century distribution, while gray boxplots show the historical distribution, depicted side-by-side to illustrate change and allow for inter-model comparison. The solid colored (end-of-century projection) and gray (historical

simulation) lines through each region's boxplots reflect the multi-model mean value. The asterisk (*) on each boxplot signifies the 95th percentile of the distribution. Here, AR characteristics shown for each region represent ARs that had at least 10% of their area within the region bounds.

AR magnitude is shown in Fig. 4.8 as the distribution of maximum IVT (kg m^{-1} s^{-1}) for all ARs detected in a given region. A shift in the multi-model mean magnitude of maximum AR IVT is apparent from the historical distribution to the end-of-century projection, indicating that the AR maximum IVT will increase in the future across all regions and seasons. DJF and SON display the distributions with the largest spread, highest values, and greatest change, relative to the historical simulation (Fig. 4.8a,d), exceeding 2000 kg m^{-1} s^{-1} in SON by the end of the century in some models in some regions, consistent with seasonal maxima in mean AR IVT shown in Fig. 4.3. In MAM, the Southern Great Plains, Midwest, Northeast, and Southeast regions reveal distributions with less spread and lower values of maximum AR IVT, rarely exceeding 1500 kg m^{-1} s^{-1}, compared to regions in the West (Northwest, Southwest, Northern Great Plains) which tend to show larger values and positively skewed distributions (Fig. 4.8b). The MRI-ESM2-0 model has a notably high 95th percentile value in MAM and SON across all regions compared to other models (Fig. 4.8b,d), while the median value for the MPI-ESM1-2-LR model tends to be lower relative to other models, notably in SON (4.8d). Qualitatively, model spread is lowest for regions in the East in DJF, MAM, and JJA, compared to model output among regions in the West.

Regional boxplots of AR area ($x10^7$ km^2) are shown for each model in Fig. 4.9. All models project increases in AR area size and variability by the end of the century across all regions and seasons. Models generally agree that the largest ARs occur in SON across all regions, with the ACCESS-ESM1-5 and MRI-ESM2-0 models capturing the largest ARs during those months, in some cases exceeding 3 $x10^7$ km^2 among the end-of-century distributions (Fig. 4.9d). ARs in MAM and JJA (Fig. 4.9b,c) tend to be smaller in areal extent compared to DJF and SON (Fig. 4.9a,d), with 95th percentile values rarely exceeding 1.5 $x10^7$ km^2 in future projections. Distributions of AR area are consistently positively skewed across all seasons and regions, including MAM and JJA where distributions show less spread (Fig. 4.9b,c). Overall, model spread shows regional and seasonal variability, with the smallest spread occurring among regions in the East in DJF and JJA (Fig. 4.9a,c), where models tend to show similar median values, 95th percentiles, and range, and largest spread in SON across all regions (Fig. 4.9d).

4.3.4.2 NCA Region Summary of AR Characteristics

End-of-century change in AR characteristics, shown at the grid point scale in Figs. 4.5-4.7, are summarized over the seven NCA regions in Fig. 4.10. Here shading reflects projected change in AR frequency and arrow size and color refer to change in maximum AR IVT magnitude and AR area, respectively. Arrow direction represents mean end-of-century AR IVT direction. Projected change in AR frequency for a given NCA region is normalized by area (i.e., number of AR days per 10,000 km^2) to account for differences

in region size. ARs in each region are again identified under the condition that at least 10% of the grid points of the AR object are within the region boundaries.

Results show the largest changes in AR area (arrow color) occur in the Northwest, Southwest, Northern Great Plains, Midwest and Northeast in SON (Fig. 4.10d) and in the Northwest in DJF (Fig. 4.10a). Change in maximum AR IVT magnitude (arrow length) is greatest in the Northwest and Northern Great Plains in DJF (Fig. 4.10a) and consistently across all regions in SON (Fig. 4.10d). Notable changes in AR day frequency are apparent in the Northwest in JJA (Fig. 4.10c) at ~5 more AR days/10,000 km^2 and in the Northeast in MAM (Fig. 4.10b) at ~6 more AR days/10,000 km^2, where relatively smaller changes in AR magnitude and area are projected. The Midwest and Southern Great Plains experience the greatest increase in AR days in MAM (Fig. 4.10b), with relatively modest increases in AR magnitude, between 100 and 150 kg m^{-1} s^{-1}. JJA reveals generally smaller changes in AR days and AR area (Fig. 4.10c), with regions in the East experiencing greater changes in AR magnitude than regions in the West. There is little regional variability among regionally aggregated AR direction in the future.

4.3.4.3 NCA Region Summary of AR Precipitation Characteristics

Seasonally and regionally summarized end-of-century change in AR precipitation characteristics are illustrated in Fig. 4.11. Here, region shading (brown-to-green) reflects change in the 95th percentile threshold for the three-day precipitation totals used to define extreme precipitation days. Each region further displays an illustrated bucket depicted

with a red and blue water level as well as a dark and light stacked gray bar. The water level refers to the median fraction of AR precipitation or the amount of precipitation that fell on AR days relative to the total precipitation amount, among the historical simulation (blue) and end-of-century projection (red). The depth of the red line, therefore, reflects the change labeled on each bucket. The adjacent bar refers to the median extreme precipitation fraction, or the number of linked AR extreme precipitation days relative to the total number of extreme precipitation days for the historical simulation (dark gray) and end-of-century projection (light gray). Again, the depth of the light gray bar reflects change in the percentage here.

Results show the largest increases in the 95th percentile extreme precipitation threshold occur in the Southeast and Northwest in DJF (Fig. 4.11a), while the majority of regions in JJA experience a decrease in the threshold by the end of the century (Fig. 4.11c). In MAM in the Southern Great Plains, Southeast, and Northeast, as well as in SON in the Northwest, ARs are projected to be responsible for 15% more of the total climatological precipitation (Fig. 4.11b,d). In the Northwest and Southwest, the largest proportion of linked days to extreme precipitation days occurs in DJF at ~85-95% with small future change and in SON at ~70-75% historically with 15% and 10% increase by the end of the century, respectively (Fig. 4.11a,d). The Northern Great Plains experiences relatively large increases in the extreme precipitation fraction across the seasonal cycle, displaying percentages between 20-30% in the historical simulation with comparable increases by the end of the century, between +15-20%. In the Southeast, ARs are projected to be

responsible for between 45-50% of the total precipitation in DJF, MAM, and SON and experience proportions between 70-75% of linked days to extreme days by the end of the century (Fig. 4.11a,b,d). Historically consistent with Mahoney et. al (2016), ARs are projected to become more influential in the Southeast during the cool/transition season months (fall-spring). The Northeast shows an increase in the 95th percentile extreme precipitation threshold in all seasons, including JJA. Among the historical simulation, ARs are responsible for 20-30% of the total precipitation across the seasonal cycle and between 50-65% of extreme precipitation days in DJF, MAM, and SON, with projected changes each ranging from +5-15% by the end of the century (Fig. 4.11a,b,d). The Southwest is projected to experience a 10% increase in AR-driven precipitation, as well as in the proportion of linked days to extreme days in all seasons except for JJA, which shows little-to-no change in the future.

4.4 Summary and Conclusions

Across the CONUS, research on the effect of climate change on ARs and associated hydrometeorological impacts is limited. The growing body of evidence documenting ARs and AR-like conditions driving precipitation extremes and flooding among the observational record warrants a CONUS-wide assessment of change under warming. To expand our understanding of the regional-scale variability in potential change in AR characteristics and associated precipitation, an objective AR detection algorithm is applied to five CMIP6 GCMs to provide a pointwise and regionally aggregated seasonal

understanding of AR frequency, magnitude, geometry, and impacts over the seven NCA regions across the CONUS.

Climatologies of projected change in AR frequency (Fig. 4.2) across the CONUS reveal increased AR day frequency in all regions and seasons by the end of the century. Notable increases in SON are evident for the Northwest, Southwest, and Northern Great Plains, indicating ~7-11 more AR days per season in the future. Projections of higher AR IVT magnitude by the end of the century in the Northern Great Plains (Fig. 4.3q-t) may point to lower precipitation efficiency by orography along the western boundary of the region. The thermodynamic response of the atmosphere, signifying a higher moisture content within an atmospheric column at high altitudes, may lessen the effect of orographic forcing (Siler and Roe 2014; Shi and Durran 2016), the dominant precipitation lifting mechanism along the West Coast, potentially altering the frequency and magnitude of inland penetrating ARs in the future. Increased AR day frequency in the Southern Great Plains, Midwest, and Northeast is also prominent among end-of-century projections in MAM (Fig. 4.2r).

IVT magnitude on AR days is also expected to increase in all US regions across the seasonal cycle (Fig. 4.3). Maxima in AR IVT magnitude in the future occur in the Northwest and Southwest in DJF and SON (Fig. 4.3q,t). Regions across the eastern US, including the Midwest, Northeast, and Southeast, reveal large increases in AR intensity in MAM and SON (Fig. 4.3r,t). Projections reveal some of the largest regional increases

in AR IVT magnitude occur in the Northeast, ranging between ~34-43 kg m^{-1} s^{-1}. Increased atmospheric moisture with warming, based on CC scaling, has been shown as the primary cause of intensified IVT (Lavers et al. 2015). Increased IVT on AR days, although not the only determinant, poses potential influence to AR-related precipitation patterns and intensity (Pendergrass 2018).

Increased AR area (Fig. 4.4) is also expected under warming based on mid- and end-of-century projections. The largest ARs in the future are projected to occur in the Northwest and Northern Great Plains, increasing by up to ~4 $x10^7$ km^2 in areal extent, suggesting potential for an increased role by vast inland penetrating ARs by the end of the century. Changes in AR geometry may also be linked to projected increases in AR days, as individual AR features will comprise a larger geographic area relative to the historical period. These results are consistent with Espinoza et al. 2018, which notes an increase in AR conditions (days) as well AR length and width.

Objectively detected ARs among model historical simulations and future projections further linked with precipitation characteristics signify potential change in AR impacts across the CONUS (Fig 4.5-4.7). Results show ARs are projected to play a bigger part in the total precipitation experienced by US regions, specifically in the Northwest in SON where ARs are projected to be responsible for ~17% more of the total precipitation in the region (Fig. 4.5y). AR-related precipitation is also shown to increase substantially in the Midwest and Northeast in MAM at 16% by the end of the century (Fig. 4.5v). Projections

of linked AR extreme precipitation days relative to the total number of extreme days, shows high percentages projected across the West in most seasons (Fig.4.6). While the dependency of local warming on precipitation intensity has been shown to modulate the rate of snowfall decline in the Cascades and Sierra Nevada (Rupp and Li 2017), change in AR driven precipitation under warming accompanied by expectations around changes in freezing level across the Northwest (Catalano et al. 2019), may influence the balance of rain versus snow, posing significant ramifications for water resource management, hydropower production, and natural ecosystems. Increases in extreme precipitation days that are AR-related are also evident across the Southern Great Plains, Midwest, and Northeast in MAM (Fig 4.6r). In general, the proportion of linked AR extreme precipitation days to AR days is projected to decrease across most US regions by the end of the century (Fig.4.7). This result may imply an increased role by other extreme precipitation-causing meteorological mechanisms; however, a more robust interpretation requires continued analysis on projected change in AR linked extreme precipitation days in the future.

Regional summaries of AR characteristics and associated precipitation across the seven NCA regions are shown in Figs. 4.8-4.11. Individual model boxplots of historical and future distributions of maximum AR IVT and AR area reveal an increase in AR magnitude and size by the end of the century across all regions and seasons with a high level of model agreement (Figs. 4.8-4.9). Regionally aggregated statistics show large increases CONUS-wide in maximum AR IVT by $\geq +150$ kg m^{-1} s^{-1} and AR area in SON,

as well as in the Northwest and Northern Great Plains in DJF (Fig. 4.10). Regionally summarized AR precipitation characteristics (Fig. 4.11) show an increase in 95th percentile multi-day precipitation across all regions and seasons, apart from JJA which largely sees a decrease in the threshold by the end of the century. ARs are broadly projected to become responsible for a larger proportion of wet days in most regions, notably in the Northwest in SON and in the Southern Great Plains, Midwest, and Northeast in MAM (Fig. 4.11b,d). Projected increases in the proportion of linked days to extreme precipitation days are also evident with regional and seasonal variability.

Several caveats should be considered when interpreting results from the climatologies of projected change presented here. The use of five models in this analysis is not sufficient for a robust sampling of model physics or internal variability. Results further require statistical significance testing, to determine error bars for projections of future change. Additionally, results have yet to be fully reconciled with a CMIP6 climate model evaluation being carried out in parallel to this study, which will offer a direct evaluation of CMIP6 model representation of AR characteristics and associated precipitation across NCA regions (Gonzalez-Hirshfeld et al. 2021). It's important to note that several methodological choices presented here have the potential to alter results, including historically defined IVT thresholding for AR detection and 95th percentile precipitation extremes defined in the future. AR detection using future IVT would likely result in lower values of AR day frequency due to a higher 85th percentile under warming. The use of historically defined 95th percentile precipitation extremes would also alter results and

conclusions from this analysis, with a higher frequency of extreme precipitation days likely. Ultimately, this study provides added understanding of the regional variability in projected change regarding the character and associated impacts of ARs and further highlights the continued need for improving our understanding of the effect of climate change on ARs across all US regions.

Chapter 5: Summary, Conclusions, and Implications of Future Work

Extreme precipitation is associated with multiple societal impacts including threats to property, agriculture, infrastructure, and even human life. While it is recognized that anthropogenic climate warming will alter precipitation extremes globally, considerable uncertainty remains around the sign and magnitude of change at local to regional scales (Wehner et al. 2010; Fischer et al. 2014; Farnham et al. 2018). In order to constrain the regional drivers of this uncertainty, an improved understanding of the roles of associated local through synoptic scale processes is required. The recurrent theme of this dissertation is to provide an in-depth understanding of regional variability in extreme precipitation and associated meteorological mechanisms in past, present, and future climates across the contiguous United States (CONUS). In particular, analyses focus on documenting the frequency and magnitude of precipitation extremes and atmospheric rivers (ARs) seasonally over the seven National Climate Assessment (NCA) regions across the CONUS, in both recent and future decades.

In *Chapter 2*, an extreme precipitation categorization scheme is developed and applied to a range of diverse precipitation measurement approaches to monitor and track extreme precipitation regionally across the CONUS, as well as to better understand and constrain observational uncertainty. *Chapter 3* applied an objective AR detection algorithm to global reanalysis to identify and characterize ARs and associated precipitation regionally across the CONUS. *Chapter 4* extended the analysis performed in *Chapter 3* to identify regional-scale variability in projected change in AR characteristics and associated

precipitation under warming across the CONUS. This chapter summarizes and discusses the key findings of each chapter, their implications and relevance within the scientific community, as well as opportunities and avenues for future work, as outlined below.

5.1 Development and Application of an Extreme Precipitation Categorization Scheme and Assessment of Observational Uncertainty

In *Chapter 2*, a gridded indicator of change in extreme precipitation over the CONUS is developed and applied to monitor and track precipitation extremes over both space and time. Developed as a contribution to NASA's support of the continuing efforts of the NCA, a key goal of this analysis was to apply the scheme as a target for a dataset intercomparison to constrain observational uncertainty and assess the effect of resolution on the ability of a dataset to capture small-scale extremes. The indicator itself manifested as a precipitation category (P-Cat) ranking system based on assigning a P-Cat to three-day precipitation totals exceeding 100mm of total accumulated precipitation. P-Cats are categorized such that, 100-200 mm is assigned P-Cat 1, 200-300 to P-Cat 2, 300-400 to P-Cat 3, 400-500 to P-Cat 4, and 500+ to P-Cat 5. To better understand and constrain observational uncertainty, the P-Cat scheme is applied as a target for a dataset intercomparison across a range of precipitation measurement products constructed using different techniques. The intercomparison includes in situ station data from the Global Historical Climatology Network-Daily (GHCN-D), satellite-derived data from the Tropical Rainfall Measuring Mission (TRMM), gridded station data from the Parameter-elevation Regression on Independent Slopes Model (PRISM), global reanalysis from the

Modern-Era Retrospective Analysis for Research and Applications, version 2 (MERRA-2), and regional reanalysis from the North American Regional Reanalysis (NARR).

Results from this analysis provide a complete and intuitive way to interpret and visualize extreme precipitation climatology across the CONUS. One of the more striking results is that the most extreme precipitation events occur across the mountains of the western US in the winter and across the southeastern US in the summer and fall, associated with ARs and tropical systems, respectively. Dataset intercomparison results provide additional insight into observational uncertainty and the importance of dataset choice when applying the P-Cat scheme to track extreme precipitation over space and time. All datasets included capture the principal spatial and temporal patterns of precipitation extremes across the CONUS, however, considerable differences exist in the magnitude and spatial extent of P-Cat climatology. In general, the datasets with the finest native resolution best capture the magnitude and spatial detail of P-Cat magnitude and frequency as measured by in-situ station data. This result is consistent with expectations that finer resolution gridded data should be able to resolve events at the far tails of the precipitation event probability distribution as compared with coarser data where spatial smoothing would reduce the magnitude of extremes. However, after datasets are spatially interpolated to a coarser grid, higher resolution products maintain the highest magnitude and frequency of P-Cat events, suggesting that a high native resolution is important for fundamentally capturing local-scale extremes. Additionally, satellite-derived products

show robust limitations at capturing extremes in regions of complex terrain across the West, specifically where frozen precipitation is a major contributor to extreme events.

The extreme precipitation categorization scheme described above was developed as a 'heavy precipitation' pilot indicator of climate change for use by the NCA. It was specifically constructed to improve upon the current indicator which failed to provide regionally specific, versatile, and user-oriented information at relevant spatial and temporal scales meaningful to most stakeholders. To better address the goals of the NCA, the P-Cat scheme was designed and executed to allow for easy calculation, visualization, and discernability of spatiotemporal changes in extreme precipitation frequency and intensity. Its usefulness extends to a wide range of user-communities from both private and public sectors, including water resource managers, local and state governments, agricultural and construction interests, and urban planners. The indicator is now available as a web-based platform, using the open-source python-based Bokeh library[2], as a point and click interactive web platform for computing and visualizing P-Cat variability across NCA sub-regions and time-periods. In addition, the observational dataset intercomparison performed here provided a necessary understanding of the range of observational uncertainty in extreme precipitation climatology, allowing for more robust conclusions about the implications associated with choosing a precipitation platform for use as a primary reference.

[2] https://bokeh-gis.geog.pdx.edu/app

Following the analysis presented in *Chapter 2*, the continued use of the P-Cat methodology offers a range of avenues for future work. The P-Cat approach is easily extensible to other regions, or globally, to facilitate temporal and spatial tracking and monitoring of extremes. The dataset intercomparison can be applied to additional precipitation measurement products (i.e., radar). The indicator also has application for use as a target for climate model evaluation, as well as integration within NASA Jet Propulsion Laboratory's Regional Climate Model Evaluation System, as a novel measure of model skill at realistically simulating extreme precipitation climatology. To improve the extensibility of the P-Cat scheme, which uses a fixed threshold to define P-Cats, a flexible P-Cat scale has since been developed (not shown here). This flexible scale uses in situ station observations to assign each P-Cat a percentile range based on a CONUS-wide three-day precipitation total frequency distribution. Percentiles are further used to identify P-Cat events among observational datasets, such that all datasets will necessarily have some occurrence of all five categories and when applied, acts to remove systematic bias that may be related to grid resolution, providing a different angle on dataset intercomparison. In turn, this flexible scheme is customizable for a given geographical region or dataset. Finally, the P-Cat methodology and usefulness as an indicator of climate change offers a basis for exploring the driving meteorological mechanisms associated with P-Cat events (e.g., ARs).

5.2 Identification of Atmospheric Rivers and Linked Precipitation Regionally Across the CONUS Within the Observational Record

In *Chapter 3*, an objective AR identification algorithm is applied to global reanalysis, from MERRA-2, to consistently characterize ARs and associated precipitation regionally across the CONUS. The approach involves a combination of percentile-based IVT thresholding, as well as a series of geometric and directional requirements to identify coherent regions of enhanced IVT. Characteristics, including AR day frequency, IVT magnitude, and area, as well as several metrics assessing linked AR extreme precipitation, are computed at each grid point and summarized over the seven NCA regions across the CONUS. Precipitation extremes are identified based on three-day precipitation totals exceeding the 95th percentile at each grid point. A minimum distance-based interpolation scheme is used to link AR characteristics, defined using MERRA-2, with PRISM's high resolution precipitation measurements. To further discern the spatial characteristics of ARs in each region, seasonal composites of AR IVT magnitude and direction, along with AR axis density plots, are computed for a major city in each of the seven NCA regions.

Seasonal climatologies of AR frequency reveal ARs in the Northwest and Southwest are most common in the winter and fall, with greater than 10% of days having a detected AR. Although considerably less widely studied, AR occurrences east of the Rocky Mountains are observable across the seasonal cycle with notable maxima of greater than 12% in the Southeast in the winter and 10% in the Central US during the summer and shoulder

seasons. Composites of IVT for cities exhibiting different AR climatologies, further highlight regional variability among AR geometries and associated water vapor pathways. Detected ARs linked with precipitation measurements show that ARs are responsible for up to 50% of the total precipitation that falls over parts of the Northwest and Southwest during the fall and winter, as well as across the Midwest and Southeast during the spring. A substantial proportion of extreme precipitation days are also associated with ARs over many parts of the CONUS, including the eastern US. However, the seasonality of linked AR extreme precipitation days is starkly different across regions. For example, across the Northwest close to 75% of extreme precipitation days are linked to ARs in the winter, while across the Midwest and southern Great Plains ARs play an important role during the summer with over 50% of extreme precipitation days AR-related. Results suggest generally higher levels of background moisture and a more diverse array of precipitation triggering mechanisms in the East are likely responsible for differences in AR occurrence and impacts compared to the West.

The role of ARs and associated impacts have been well-documented across the western US, with considerably less attention focused on the influence of ARs in other regions across the CONUS. However, a growing body of evidence, predominantly in the form of case-studies and regionally specific analyses, support links between AR-like conditions and a number of heavy precipitation and high-impact flood events across parts of the central/eastern US. This study was the first to summarize AR climatology and importance as a mechanism for extreme precipitation consistently, at relatively fine

spatial scales, over the seven NCA regions across the CONUS. In turn, results offer insight into the fundamental importance of ARs to the hydroclimate of many regions across the CONUS where they have been largely under-studied. While it was beyond the scope of the study to attempt to link AR objects with any phenomena besides extreme precipitation, interpretation of AR activity, characteristics, and hydrometeorological impacts across regions largely overlapped with a number of other well-documented phenomena of the climate system, speaking to the complex and interwoven mechanisms driving AR impacts. For example, high AR occurrence over the Great Plains and Ohio River Valley in the spring indicated potential linkages to moisture transport through features like the Great Plains low-level jet and "Maya Express." Furthermore, high rates of AR extreme precipitation across the eastern half of the US, where orographic lifting of AR moisture is minimal or non-existent, suggests new insights regarding the role of non-orographic or synoptic and mesoscale forcing (e.g., convection, frontal, isentropic lift) in AR-related precipitation patterns, intensity, and duration across the East.

Results from this study can be leveraged in a number of ways to support ongoing work. The observed AR characteristics and metrics used to assess regional variability here are currently being applied to evaluate the performance of climate models at accurately representing the seasonality and regional distribution of AR characteristics and precipitation extremes across the CONUS (Gonzalez-Hirshfeld et al. 2021). Observed patterns of AR frequency, geometry, magnitude, and impacts further serve as a benchmark for quantifying projections of change in future AR characteristics under

global warming (i.e., *Chapter 4*). Insight surrounding the role of non-orographically driven AR precipitation further motivates questions regarding the key synoptic environments (i.e., meteorological characteristics, dynamical processes, lifting mechanisms) responsible for producing precipitation during an AR and their regional variability. With a growing understanding of the geographical extent of AR impacts, a number of analyses that have been applied to the West Coast can equally be applied to the East. For example, ARs have been documented as influential in modulating drought along the US West Coast (Dettinger 2013). With additional insight from this analysis as to the substantial role of ARs in regional precipitation and extremes across the East, questions emerge around the role ARs and drought in regions East of the Rockies, such as the agriculturally rich Great Plains. Finally, results from this analysis have the opportunity to motivate continued robust regional-scale analyses of AR importance in regions around the globe where they may not yet be fully understood.

5.3 Quantification of the Effect of Climate Change on Atmospheric River Characteristics and Associated Precipitation using CMIP6 Models

In *Chapter 4*, an objective AR identification algorithm is applied to five Coupled Model Intercomparison Project Phase 6 (CMIP6) models to quantify projected change in AR characteristics and associated precipitation by the end of the century. AR identification uses relative IVT thresholding consistent for the current and future climate and is applied uniformly and consistently across CONUS. Change is quantified between each CMIP6 model's historical simulation (1984-2013) and mid- (2036-2065) and end-of-century

(2071-2100) projections under the Shared Socioeconomic Pathway (SSP) 585, or high-end emissions warming scenario. The projected impact of warming on AR frequency, geometry, intensity, and associated precipitation is quantified at the grid point scale as well as summarized over the seven NCA regions across the CONUS. ARs are subsequently linked with extreme precipitation occurrence, defined as three-day precipitation totals exceeding the 95th percentile relative to a given time period. An AR extreme precipitation linkage is made when an AR is collocated with at least one day in the three-day total used to define the extreme. An inter-model comparison, assessed model spread among historical simulation and end-of-century projection results for the distribution of AR IVT magnitude and area among ARs detected in each NCA region stratified by season.

Projections indicate that increases in AR days will occur across all regions and seasons by the end of the 21st century. Notable maxima occur in the West in the winter, central and southeastern US in the spring, parts of the Northeast in the summer, and Pacific Northwest and interior West in the fall. AR IVT magnitude is also projected to increase across all regions and seasons by the mid- and end-of century, with little-to-no change in AR IVT direction. Some of the greatest regional change in AR IVT is projected to occur in the Northeast by +40 kg m^{-1} s^{-1} in the spring and fall. Projections of the seasonal distribution of AR area also show positive change in the future, indicating some of the largest ARs will occur across the Northwest and Northern Great Plains in the winter and fall. Model intercomparison results show a high degree of model agreement regarding

increased maximum AR IVT magnitude and AR area by the end of the century. Linked AR precipitation characteristics indicate ARs will be responsible for a larger proportion of total precipitation in most regions by the end of the century, notably in the Midwest and Northeast in the spring and in the Northwest and Northeast in the fall by +15-17%. The proportion of linked AR extreme precipitation days to the total number of extreme days is also projected to increase, with a large expanse of the West maintaining between 90-100% in the winter and the Ohio River Valley experiencing between ~70-85% in the winter, spring, and fall. Projections of the proportion of linked days to AR days reveal largely negative change in the future, requiring further assessment of the projected change in linked days.

This work was carried out as an extension of the analysis presented in *Chapter 3*, and was motivated by the need for a more holistic and comprehensive understanding of ARs and their response to climate change across the CONUS. While the documentation of observed change, characteristics, and impacts of ARs outside of the western US is limited, as mentioned above, our understanding of projected change in ARs under warming in most US regions, at impacts-relevant scales, is largely non-existent. Using the latest available state-of-the-art suite of global climates models (GCM's) from the CMIP6 database, this is the first study, to date, to assess climate change effects on ARs over the seven NCA regions across the CONUS. Results are further presented at grid point through regional scales, to capture and record fine-scale changes, as well as communicate aggregated regional results, most relevant to society and stakeholders.

While results across the West largely corroborated with existing literature documenting increases in AR frequency, intensity, and associated impacts in the future, this work further illuminated potential change in regions across the East, where AR research is minimal. The combination of the observational analysis in *Chapter 3* and this climate change assessment aim to provide a more comprehensive and consistent CONUS-scale analysis of ARs for the continued efforts of the NCA as a contribution to future reports.

While the documented effects of warming on ARs within this analysis are thorough, interpretation of the results relies heavily upon climate model fidelity and the ability of climate models to realistically simulate AR climatology relative to observations. Towards this end, an evaluation of AR representation in CMIP6 models is currently being carried out in parallel to this assessment and preliminary results do show some notable biases which have not yet been thoroughly reconciled with projections (Gonzalez-Hirshfeld et al. 2021). In addition to a contextual understanding of model performance, results from this analysis motivate the need for continued diagnostic studies to identify sources of systematic bias in AR representation among models to improve simulations and projections. This analysis employs a multi-model approach in an effort to reduce the sensitivity of results to any one model's construction choices. However, due to limitations in data availability, the use of only five model further lends itself to the inclusion of more models, as data becomes available, to reduce sensitivities. Results further motivate the incorporation of additional metrics (e.g., AR duration, thermodynamic vs dynamic drivers of change in AR IVT, etc.) for evaluating the

changing role of ARs with warming across US regions. Future research identifying the key synoptic environments and processes that contribute to precipitation formation in ARs, their representation among climate models, and their potential for change under warming is critical to an improved understanding of potential intensification and regional variability of AR impacts in the future.

5.4 Concluding Remarks

While extreme precipitation is generally expected to intensify under global warming, uncertainty remains around the sign and magnitude of change at local through regional scales. With change likely underway and impacts being felt, a firm and comprehensive understanding of future projections of extreme precipitation at impacts-relevant scales is both critical and urgent. The results and conclusions from this dissertation aim to identify and quantify uncertainty in the regional-scale variability of extreme precipitation climatology and associated meteorological mechanisms in past, present, and future climates. As a contribution to the continuing efforts of the NCA, each main chapter provides information at regionally-relevant scales, computed at each grid point as well as summarized over the seven NCA regions across the CONUS. The methodologies and statistical analyses applied here are simple, yet robust, measures of regional variability and change that can easily be reproduced to foster and support continued analyses on precipitation extremes.

The World Climate Research Program's 'Weather and Climate Extremes' Grand Challenge identifies two key questions as critical to its advancement. These questions address whether current observations are sufficient for studying extremes and what the roles of local through synoptic scale processes are in the formation of extremes. The culmination of the three main chapters of this dissertation directly addresses these widely recognized challenges. To address observational sufficiency, *Chapter 2* demonstrates differences among data products at capturing extreme precipitation climatology across the CONUS. Amidst substantial variability, product limitations were largely driven by native grid resolution in reanalysis products, misrepresentation of complex terrain and snowfall in satellite-derived products, and spatiotemporal inconsistencies among in situ data. Observations are the key foundation for understanding long-term climate variability and change. Continued investigation of data limitations and inconsistencies is necessary to inform future instrumental and algorithmic improvements required to underpin detection and attribution studies and model evaluation.

To address the roles of synoptic, regional, and local scale processes in the formation of extremes, *Chapters 3* and *4* focus on ARs, which exist as one part of a larger, synoptic scale dynamical system driving precipitation extremes across the CONUS. ARs play a substantial role in driving extreme precipitation across many regions CONUS-wide, with the potential for change under warming reinforcing their importance to water resources. ARs have their own physical and statistical properties, which vary locally, regionally, and seasonally, but are distinct from other storms and weather phenomena. Recognition

of their special roles in weather and climate extremes will allow for more targeted responses to both the risks and benefits to society now and in the future. Better quantification of the importance of meteorological mechanisms and their interactions is critical for reducing uncertainties in projections and improving sub-seasonal to decadal predictability of extreme precipitation and attribution.

Looking forward, future climate change impacts studies require an improved dynamical and physical process-based understanding of extreme precipitation and the associated driving meteorological mechanisms. Given the important role ARs play in the regional hydrometeorology of the US and their role in weather and water extremes, understanding how the underlying synoptic scale weather patterns associated with enhanced AR precipitation events will change in the future is imperative. The profound effects of topographic forcing on winter mid-latitude cyclones and AR conditions are well-documented across the US West Coast (Ralph et al. 2006; Neiman et al. 2008a; Paltan et al. 2017). However, this is not the only mechanism inducing the upward motion of moisture necessary for triggering precipitation; other processes, such as synoptic and mesoscale systems, can play an important role in the intensification of precipitation via convective motion. At present, an observed robust investigation of the multiscale interactions and dynamic environment within ARs that drive associated extreme precipitation across regions over the CONUS does not exist. Knowledge of these synoptic regimes is necessary to address the current challenges in AR forecasting and projections of their distribution, intensity, and frequency. Future work leveraging the

findings from this dissertation, aims to carry out a rigorous and robust investigation of the underlying dynamics driving AR precipitation extremes and their spatiotemporal variability across the CONUS. Reducing uncertainty in the regional-scale variability and disproportionate rates of change in extreme weather and climate events across the CONUS is crucial in order to mitigate risk and reduce negative impacts to natural systems and society.

Chapter 2 Tables

Agency Source	Dataset		Spatial Resolution	Temporal Resolution	Data Source	Reference
NASA	TMPA	TRMM Multi-Satellite Precipitation Analysis 3B42V7	0.25° x 0.25°	3-hourly	Satellite	Huffman et al. (2007)
NASA	IMERG	Integrated MultiSatellite Retrievals for GPM	0.1° x 0.1°	30-minute	Satellite	Huffman et al. (2017)
OSU	PRISM	Parameter-Elevation Regressions on Independent Slopes Model	0.04° x 0.04°	Daily	Gridded in situ station data	Daly et al. (1994)
NASA	MERRA-2	Modern Era RetrospectiveAnalysis version 2	0.625° x 0.5°	3-hourly	Global Reanalysis	Molod et al. (2015)
NCEP	NARR	North American Regional Reanalysis	32 km x 32 km	3-hourly	Regional Reanalysis with gauge assimilation	Mesinger et al. (2006)
NOAA	GHCN-D	Global Historical Climatology Network		Daily	In situ station data	Menne et al. (2012)

Table 2.1 Datasets used in the intercomparison and their associated specifications.

Coefficients of Variation					
Annual P-Cat Frequency: CONUS					
	P-Cat 1	P-Cat 2	P-Cat 3	P-Cat 4	P-Cat 5
GHCN-D	0.1506	0.3602	0.4901	0.9164	1.3614
PRISM	0.2029	0.4466	0.7060	0.9800	1.2972
TMPA	0.2834	0.7035	1.4352	2.2687	4.2426
NARR	0.256	0.6584	1.3625		
MERRA-2	0.3701	0.9433	2.7955	4.2426	

Table 2.2 Dataset's coefficient of variation values for each P-Cat's annual frequency across the CONUS.

Coefficients of Variation					
SON P-Cat Frequency: Southeast					
	P-Cat 1	P-Cat 2	P-Cat 3	P-Cat 4	P-Cat 5
GHCN-D	0.4325	0.7217	1.1422	1.856	2.7255
PRISM	0.4839	0.7796	1.4984	1.8646	2.2129
TMPA	0.5626	1.0129	2.2725	3.2571	4.2426
NARR	0.5970	1.0043	3.0870		
MERRA-2	0.6522	1.2568	2.9218	4.2426	

Table 2.3 Same as in Table 2 except for SON and only over the Southeast sub-region.

Coefficients of Variation					
DJF P-Cat Frequency: Northwest					
	P-Cat 1	P-Cat 2	P-Cat 3	P-Cat 4	P-Cat 5
GHCN-D	0.4082	0.6106	1.4798	2.4589	4.2426
PRISM	0.4393	0.6483	0.9957	1.5989	1.9965
TMPA	0.8906	1.7957	4.2426		
NARR	0.5802	1.3096	2.7069		
MERRA-2	0.6997	2.5205			

Table 2.4 Same as in Table 2 except for DJF and only over the Northwest sub-region.

Chapter 3 Tables

NCA Region	AR Frequency				Magnitude of Mean IVT ($kg\ m^{-1}\ s^{-1}$)				Direction of Mean IVT (degree)				Area ($x10^6\ km^2$)			
	DJF	***MAM***	***JJA***	***SON***	***DJF***	***MAM***	***JJA***	***SON***	***DJF***	***MAM***	***JJA***	***SON***	***DJF***	***MAM***	***JJA***	***SON***
NW	530	504	627	658	303.14	233.95	220.47	273.42	62.88	58.56	50.08	57.67	3.73	2.10	1.27	2.35
SW	935	1022	1279	1209	271.78	232.01	240.44	273.61	60.42	53.25	49.94	51.90	3.15	1.84	1.04	2.03
GPN	639	943	1236	1114	273.12	258.18	278.45	292.51	59.22	49.59	48.12	50.51	3.51	2.08	1.26	2.30
GPS	937	1190	1211	1163	294.62	313.51	350.22	335.58	53.58	45.74	59.70	46.66	2.66	1.84	1.31	2.05
MW	840	1120	1133	1233	321.84	351.34	388.32	360.89	52.33	46.83	57.87	47.89	2.87	2.07	1.79	2.30
NE	654	734	713	741	387.14	396.62	455.64	414.56	52.61	52.47	63.72	51.61	2.80	2.26	2.06	2.31
SE	1071	1231	986	1146	370.55	388.37	441.79	397.06	50.47	46.87	62.50	47.12	2.41	1.93	1.70	2.05

Table 3.1 Aggregated statistics for seasonal AR characteristics summarized over each of the seven NCA regions including AR frequency (ARs/10,000 km^2); median IVT magnitude ($kg\ m^{-1}\ s^{-1}$); median direction of mean AR IVT (degree), and median AR area ($x10^6\ km^2$).

NCA Region	Extreme Precip. Frequency				Fraction of Total Precip. (%)				Extreme Precip. Fraction (%)				AR Fraction (%)			
	DJF	MAM	JJA	SON	DJF	MAM	JJA	SON	DJF	MAM	JJA	SON	DJF	MAM	JJA	SON
NW	124	123	68	98	24.97	13.18	11.38	21.89	74.73	40.74	28.00	60.92	27.47	18.00	7.25	16.99
SW	69	68	71	63	24.92	14.00	13.14	27.61	66.00	39.66	34.69	66.20	14.65	8.59	8.03	11.56
GPN	69	98	110	76	4.17	7.28	9.68	11.63	18.06	23.76	24.56	33.33	5.66	10.48	8.41	8.25
GPS	61	86	91	70	21.90	19.85	14.47	26.48	49.09	50.94	38.18	59.42	7.65	10.02	10.22	8.98
MW	95	115	118	100	18.76	23.50	20.66	30.80	53.19	54.46	49.18	66.04	18.75	16.27	15.85	15.26
NE	126	127	129	118	25.97	21.11	18.42	26.14	61.86	54.10	46.88	57.14	17.75	15.96	14.80	12.56
SE	107	107	123	91	39.85	32.68	20.67	37.20	79.67	73.47	48.28	71.43	16.37	15.17	17.48	15.82

Table 3.2 Aggregated statistics for seasonal AR precipitation characteristics summarized over each of the seven NCA regions including extreme precipitation day frequency (spatial median); fraction of AR precipitation relative to total precipitation (%); fraction of AR extreme precipitation relative to total extreme precipitation days (%); and fraction of AR extreme precipitation relative to total AR days (%).

Chapter 4 Tables

Model	**Native Grid**	
MPI-ESM1-2-HR	384x192	0.7°
BCC-CSM2-MR	320x160	1.1°
MRI-ESM2-0	320x160	1.1°
ACCESS-ESM1-5	192x144	1.5°
MPI-ESM1-2-LR	192x96	1.9°

Note: Native grid spacing is calculated as $\left(\frac{360}{Nlon}\frac{180}{Nlat}\right)^{0.5}$, where *Nlon* and *Nlat* are the number of grid points in the x and y direction (as in Norris et al. 2021; see study for relevant caveats). Models are listed in ascending order of native grid spacing.

Table 4.1 CMIP6 models included in study.

Chapter 2 Figures

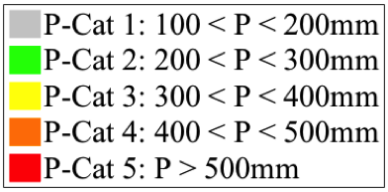

Figure 2.1 P-Cat thresholds and associated colors used in subsequent figures.

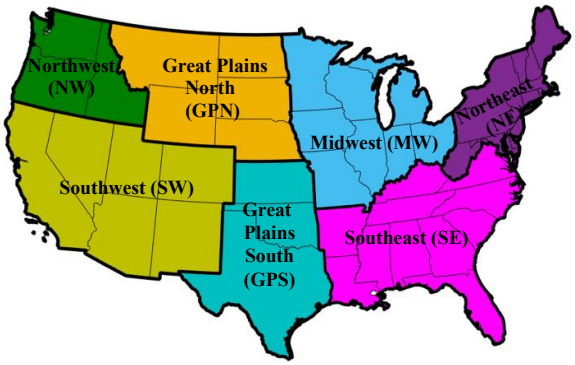

Figure 2.2 The seven NCA sub-regions and the associated abbreviations.

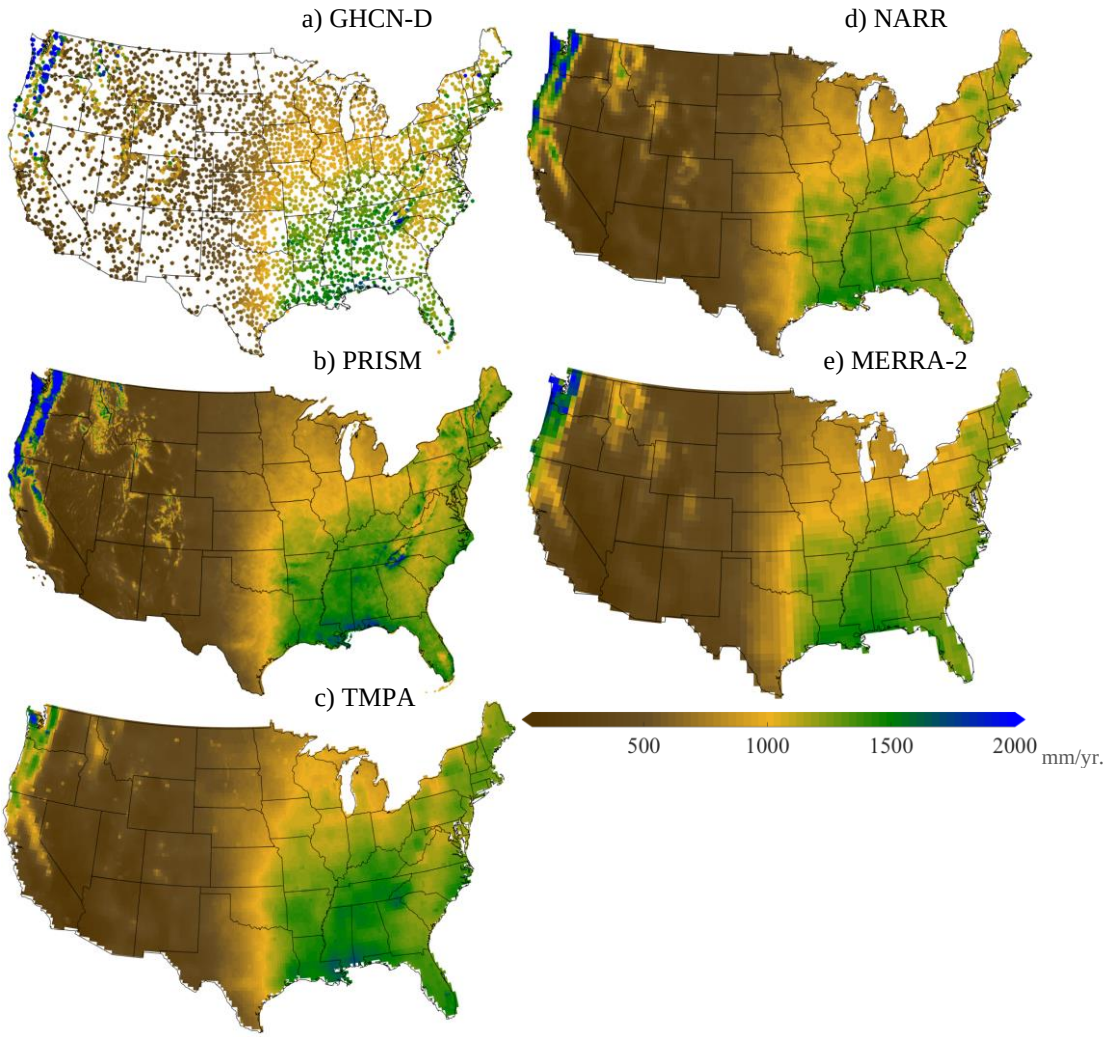

Figure 2.3 Average annual precipitation over the period of 1998-2015. Results are for (a) GHCN-D, (b) PRISM, (c) TMPA, (d) NARR, and (e) MERRA-2.

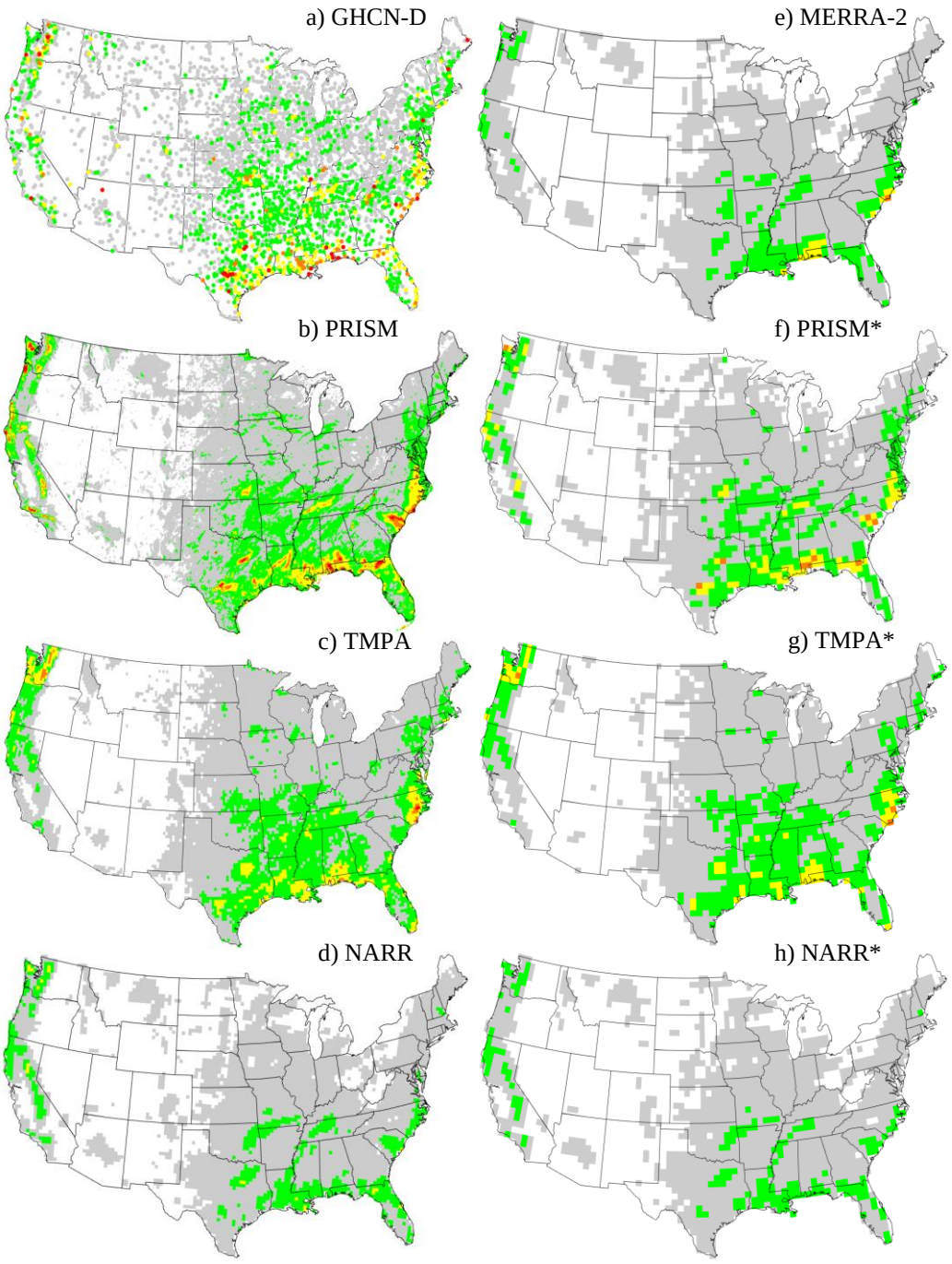
a) GHCN-D
e) MERRA-2
b) PRISM
f) PRISM*
c) TMPA
g) TMPA*
d) NARR
h) NARR*

Figure 2.4 Maximum observed P-Cat at each grid point over the 1998-2015 period. (a-d) Maximum P-Cats on native grid, (e-h) maximum P-Cats on common MERRA-2 grid. Spatially interpolated datasets are indicated with an asterisk. Color scale is as in Figure 2.1. Un-shaded grid points indicate that no P-Cat has occurred during the data record.

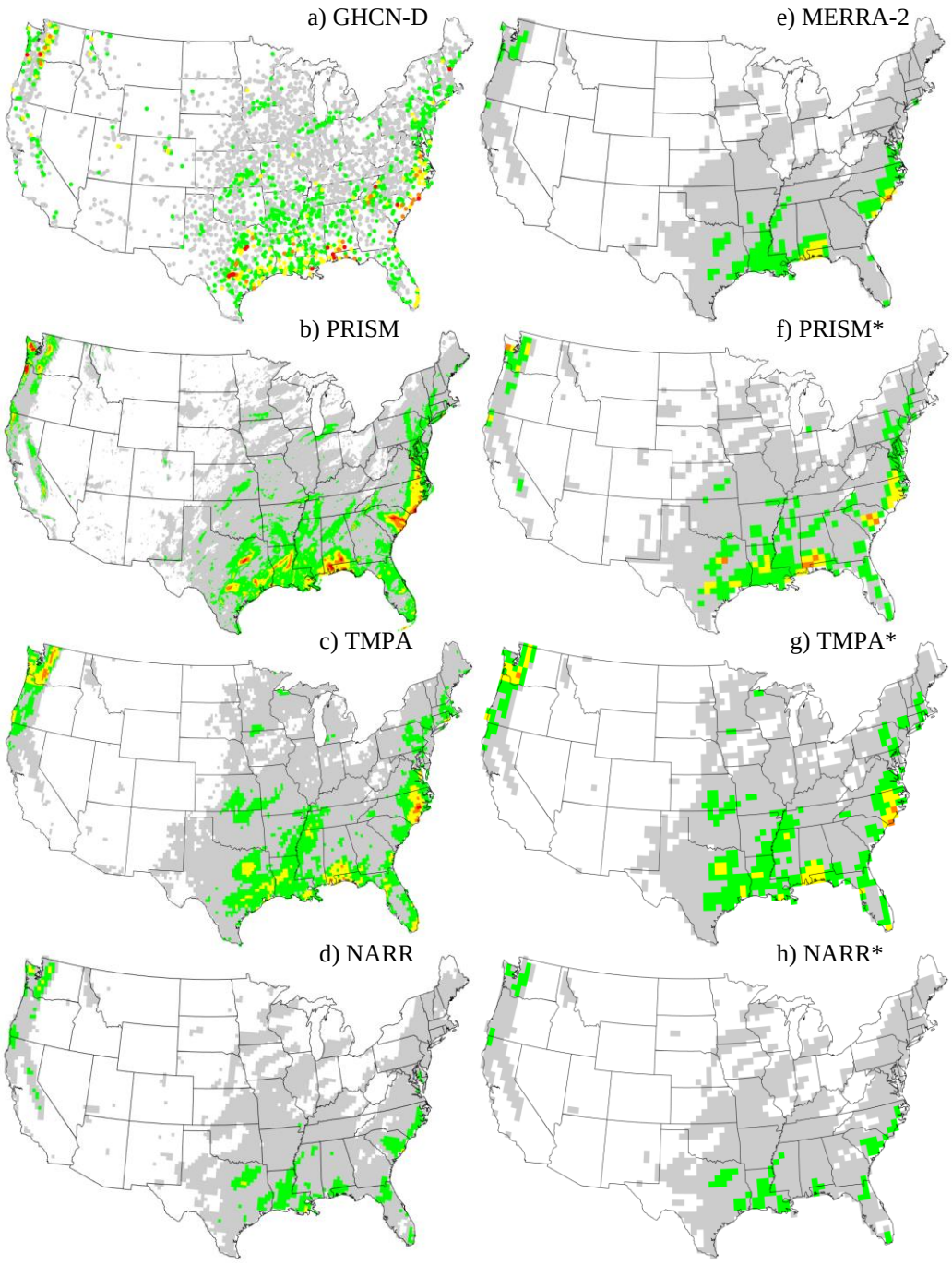

Figure 2.5 Same as in Figure 2.4 except for SON.

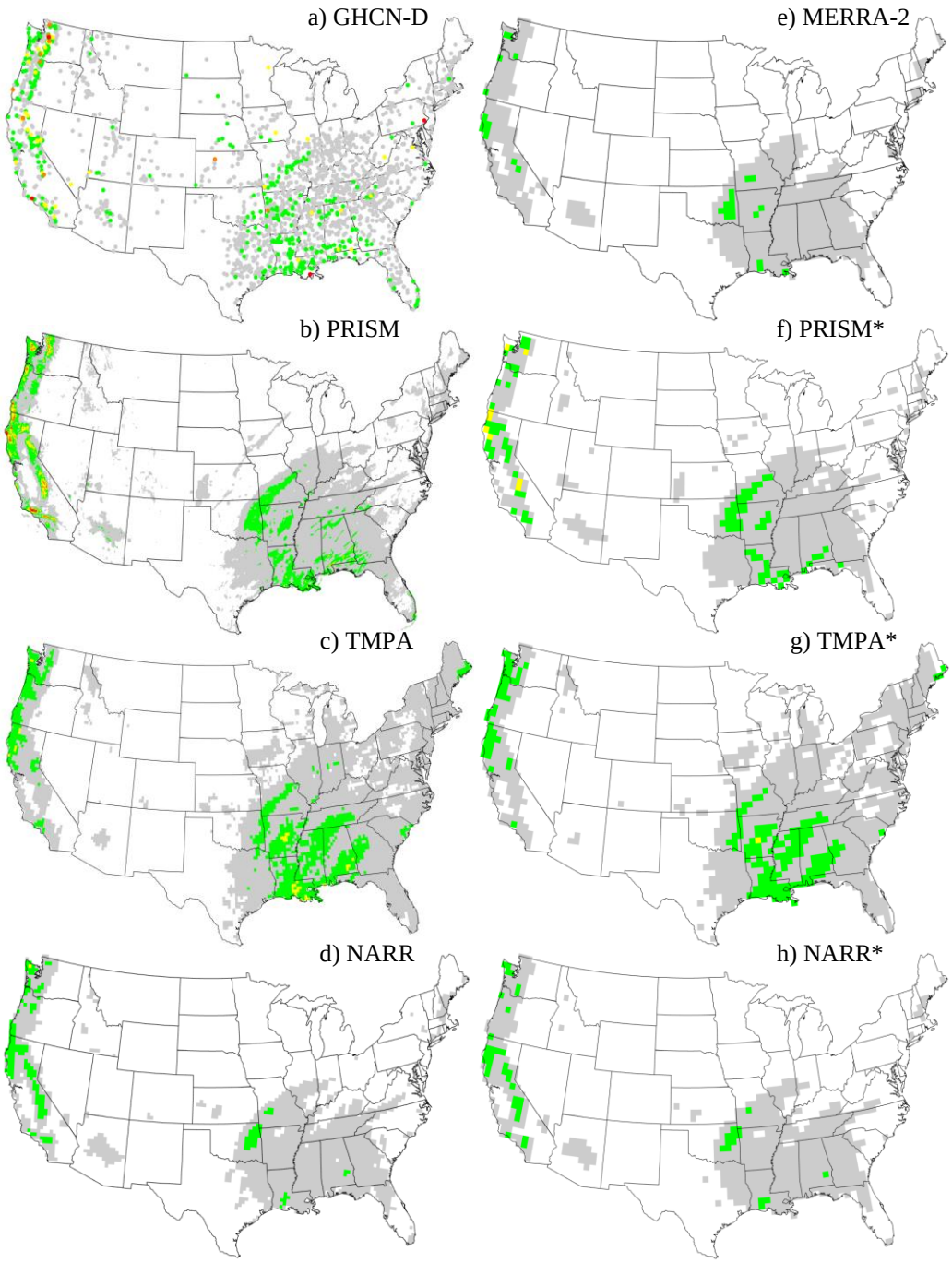

Figure 2.6 Same as in Figure 2.4 except for DJF.

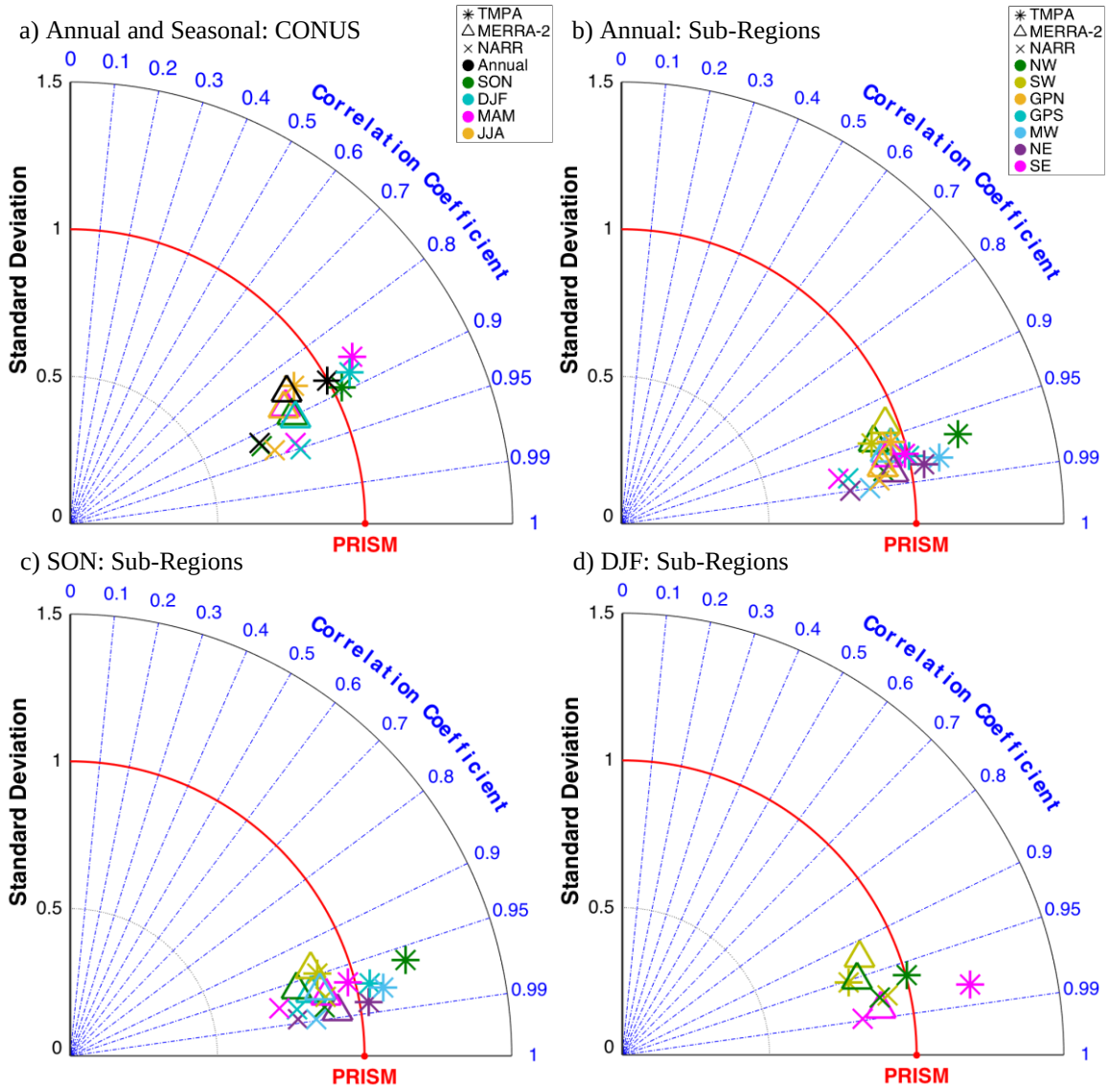
a) Annual and Seasonal: CONUS
b) Annual: Sub-Regions
c) SON: Sub-Regions
d) DJF: Sub-Regions
TMPA
MERRA-2
NARR
Annual
SON
DJF
MAM
JJA
NW
SW
GPN
GPS
MW
NE
SE
Correlation Coefficient
Standard Deviation
PRISM
0
0.1
0.2
0.3
0.4
0.5
0.6
0.7
0.8
0.9
0.95
0.99
1
1.5
0.5

Figure 2.7 Taylor diagrams quantifying the spatial correspondence of the maximum observed P-Cats for TMPA, MERRA-2, and NARR relative to PRISM. Results are for (a) the CONUS annually and seasonally, (b) relevant NCA sub-regions annually, (c) September, October, November for the NCA sub-regions, and (d) December, January, February for the NCA sub-regions. Each dataset is labeled by a symbol with each season and sub-region assigned a color as defined in the legends in the top two panels. The x and y axes correspond to the standard deviation ratio between the indicated dataset and PRISM. The radial axis is the pattern correlation, and the distance between the symbol and the PRISM location is proportional to the centered root mean squared difference between the spatial field of the maximum P-Cats of the indicated dataset and PRISM, normalized by the spatial standard deviation of the PRISM field.

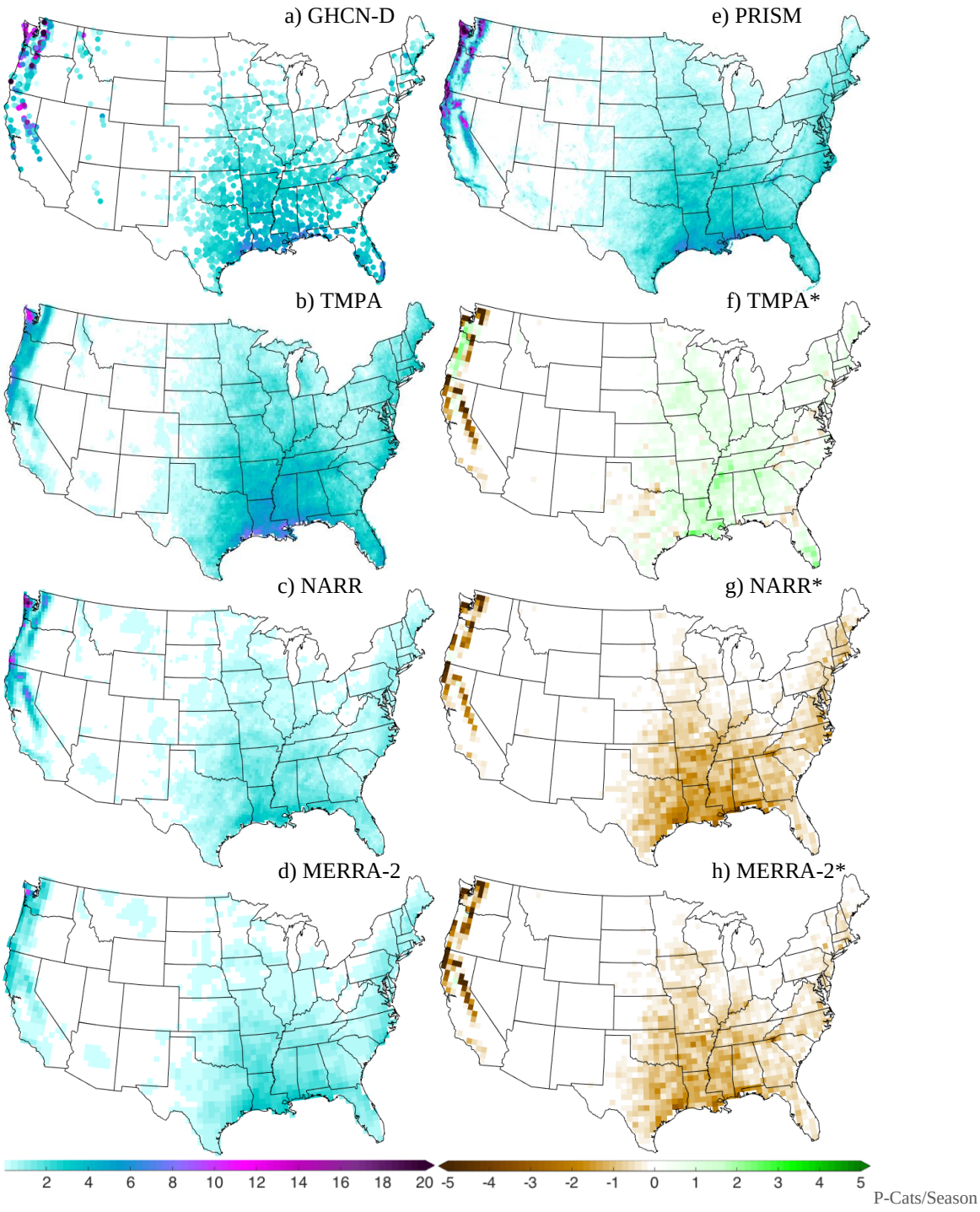
a) GHCN-D
e) PRISM
b) TMPA
f) TMPA*
c) NARR
g) NARR*
d) MERRA-2
h) MERRA-2*
2 4 6 8 10 12 14 16 18 20
-5 -4 -3 -2 -1 0 1 2 3 4 5
P-Cats/Season

Figure 2.8 (a-e) Mean annual frequency of P-Cat occurrence over the 1998-2015 record, (f-h) the difference between the mean annual frequency of P-Cat occurrence in the indicated dataset and PRISM. Frequencies are recorded as the number of P-Cats per year. Spatially interpolated datasets are indicated with an asterisk.

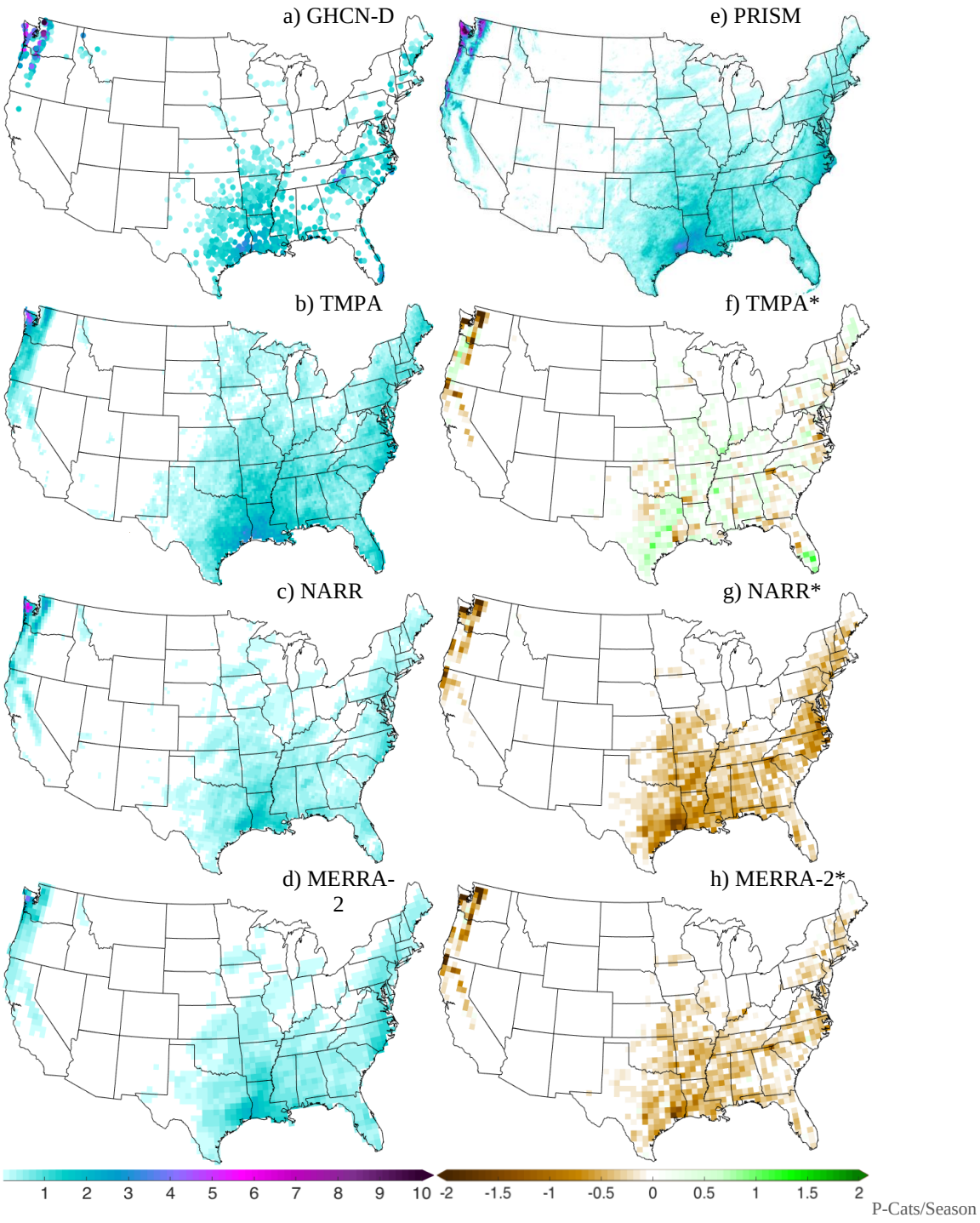

Figure 2.9 Same as in Figure 2.8 except for SON.

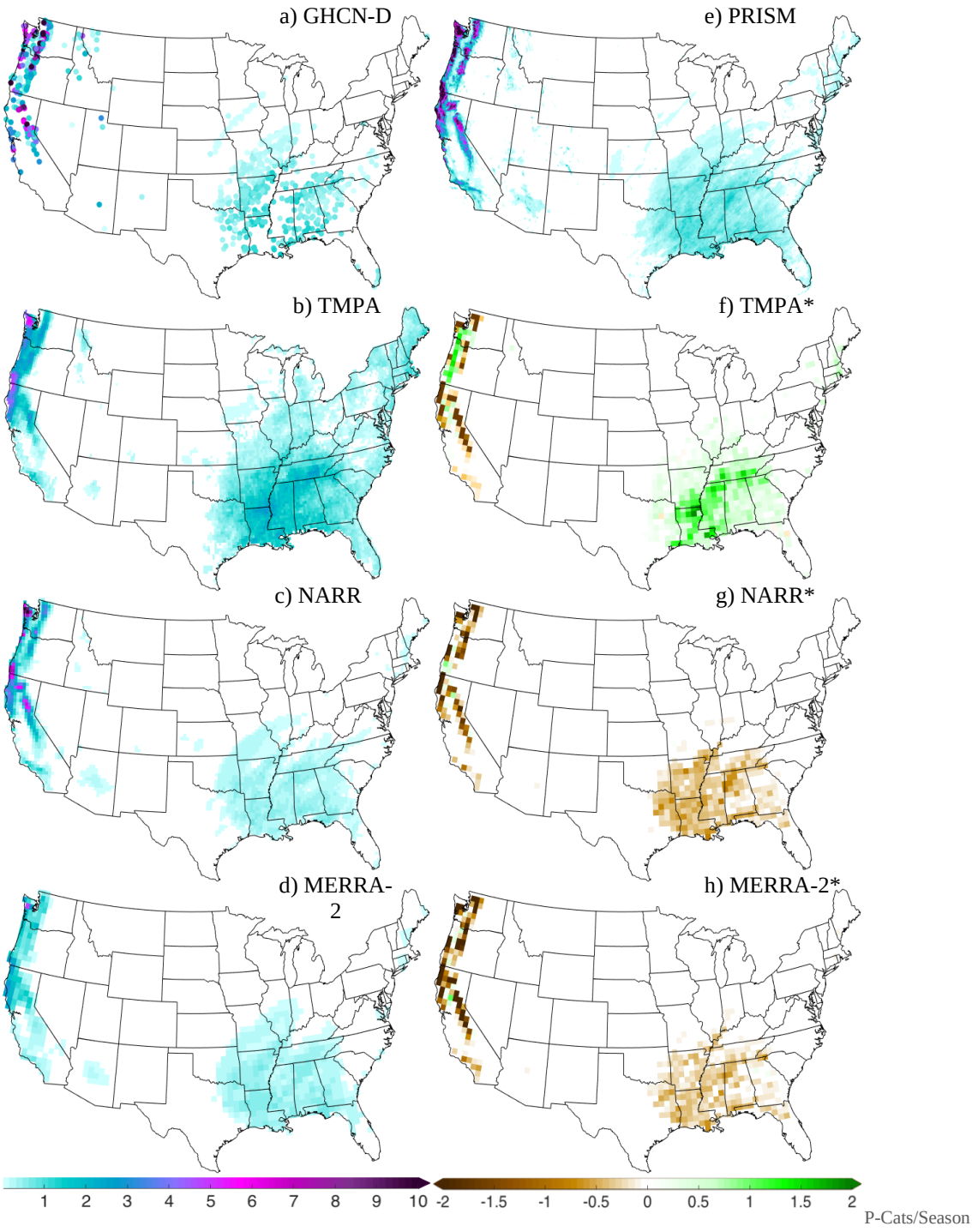

Figure 2.10 Same as in Figure 2.8 except for DJF.

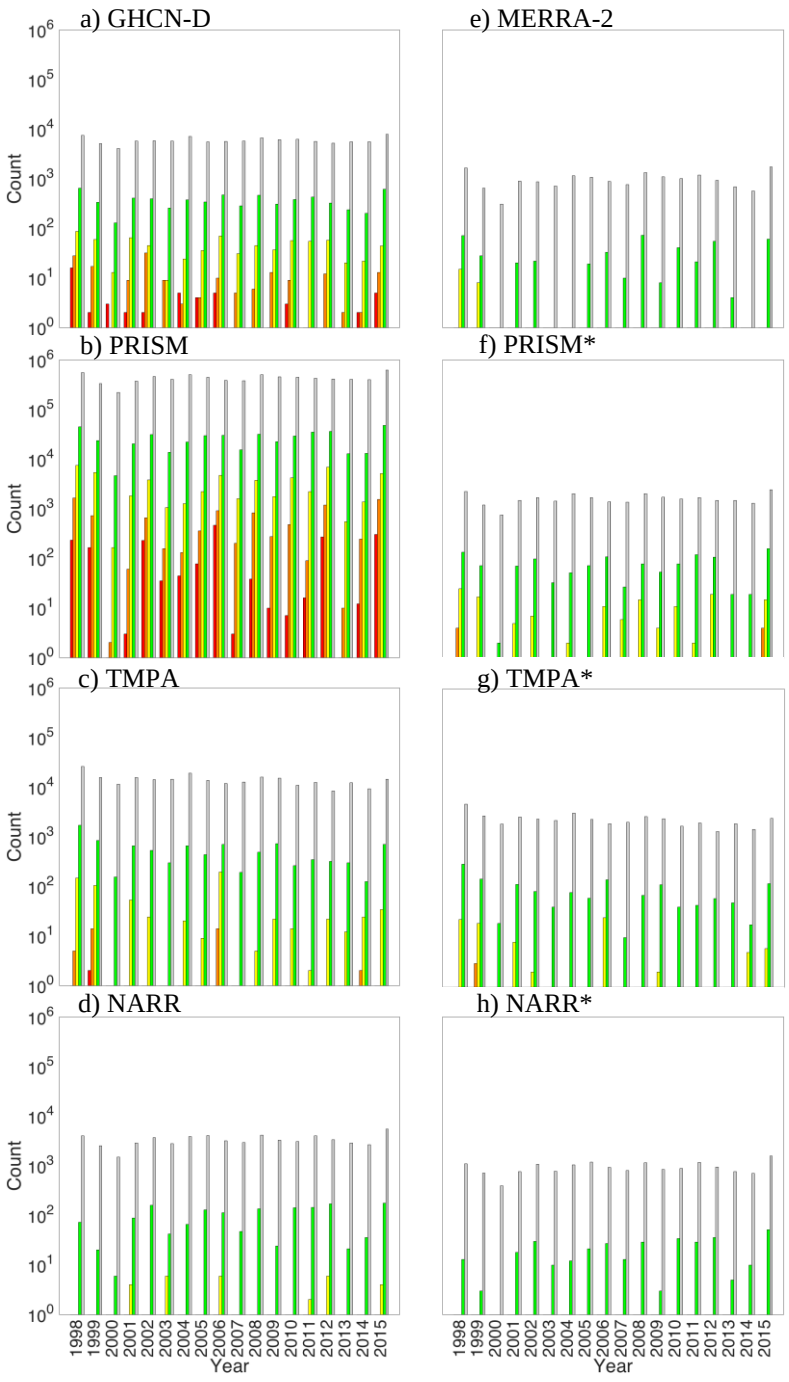
a) GHCN-D
e) MERRA-2
b) PRISM
f) PRISM*
c) TMPA
g) TMPA*
d) NARR
h) NARR*
Count
Year
1998
1999
2000
2001
2002
2003
2004
2005
2006
2007
2008
2009
2010
2011
2012
2013
2014
2015

Figure 2.11 Annual frequency of observed P-Cats over the 1998-2015 period. (a-d) Annual frequency of P-Cats on native grid, (e-h) annual frequency of P-Cats on common grid. Spatially interpolated datasets are indicated with an asterisk. Gray bars represent P-Cat 1, green P-Cat 2, yellow P-Cat 3, orange P-Cat 4, and red P-Cat 5 as in the legend in Figure 2.1. Results are plotted on a log scale.

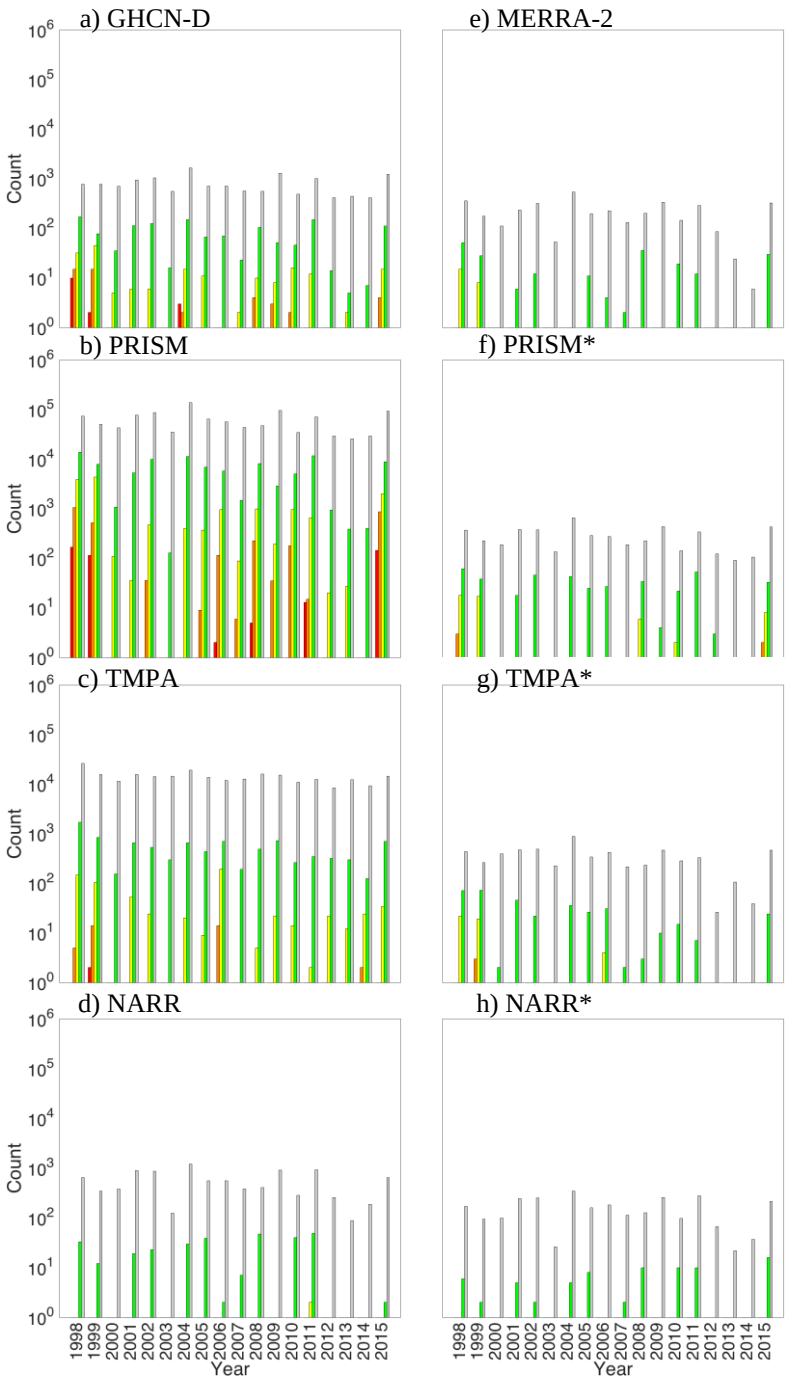

Figure 2.12 Same as in Figure 2.11 except for SON and only over the Southeast sub-region.

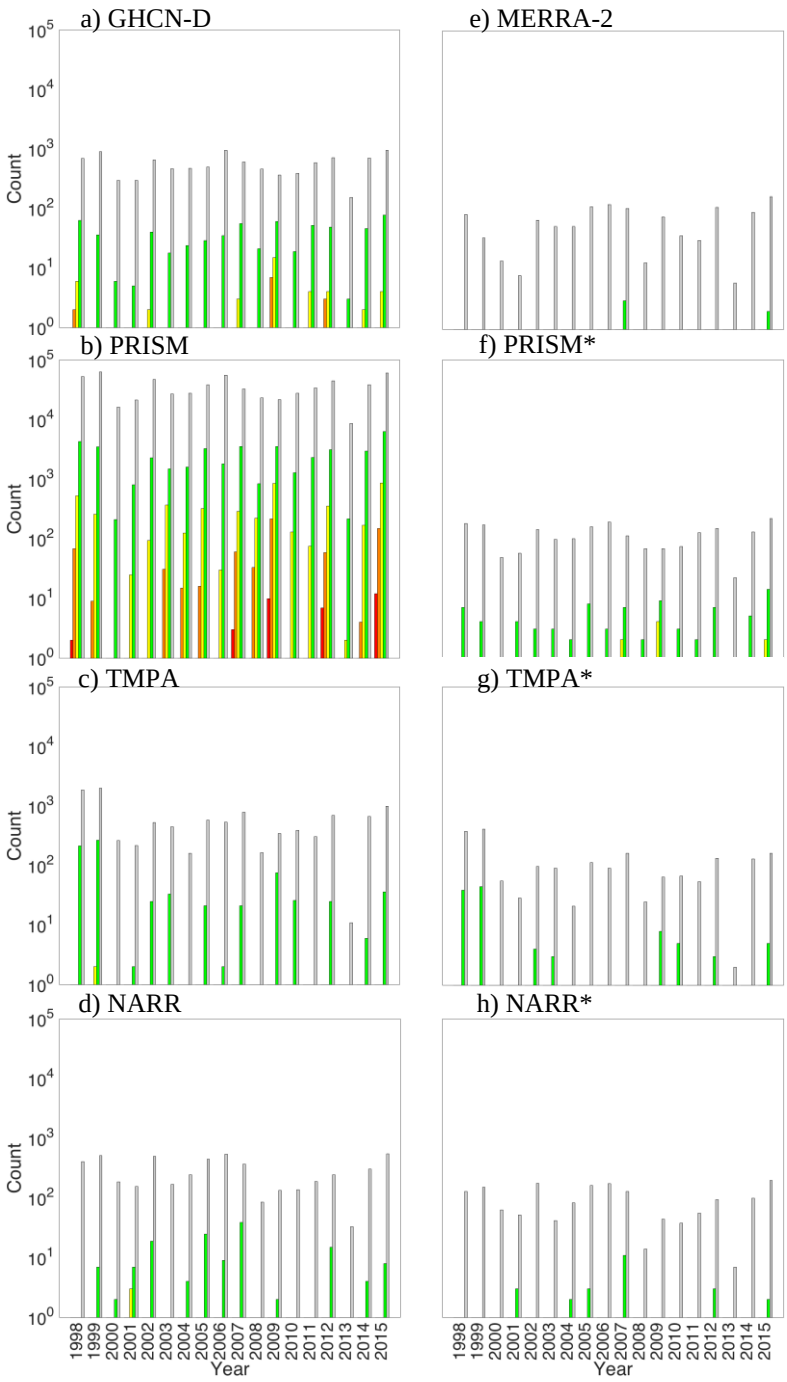

Figure 2.13 Same as in Figure 2.11 except for DJF and only over the Northwest sub-region.

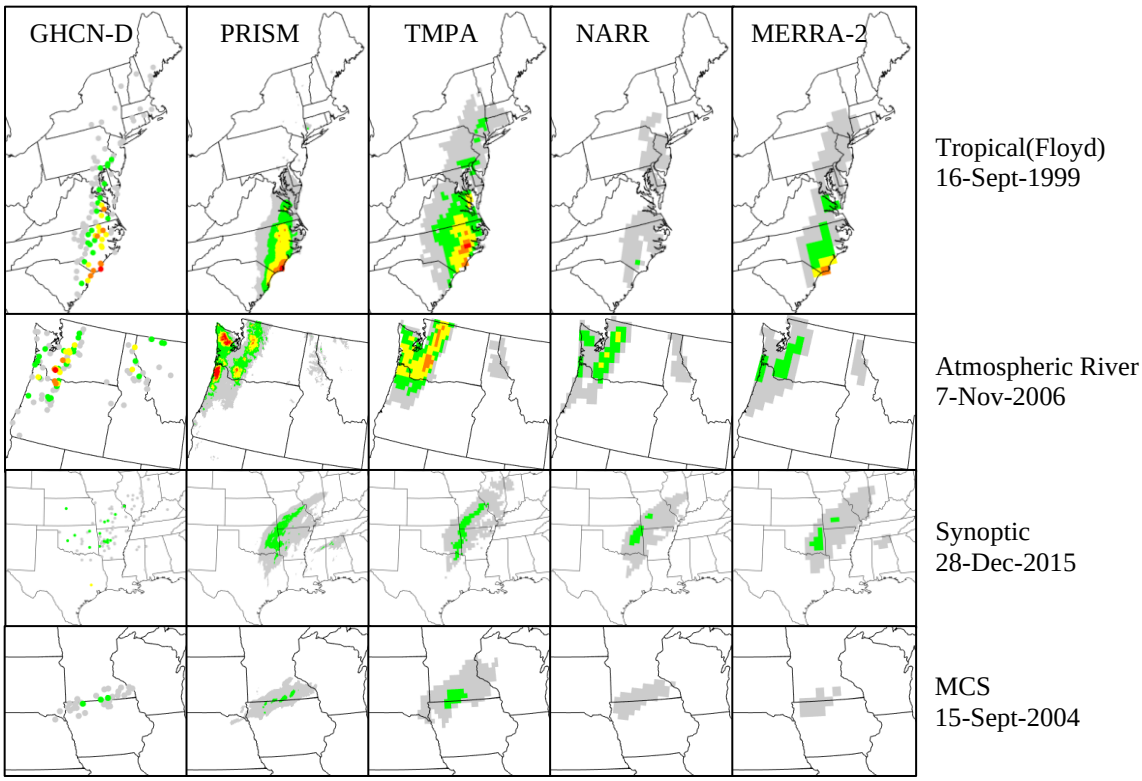

Figure 2.14 P-Cat values for four individual storm events. The color scheme follows previous figures. P-Cat values are computed as the three-day precipitation total ending on the day indicated at the right of each row. Storms include a tropical cyclone (Floyd), an atmospheric river, a synoptic scale mid-latitude winter cyclone, and a mesoscale convective system (MCS).

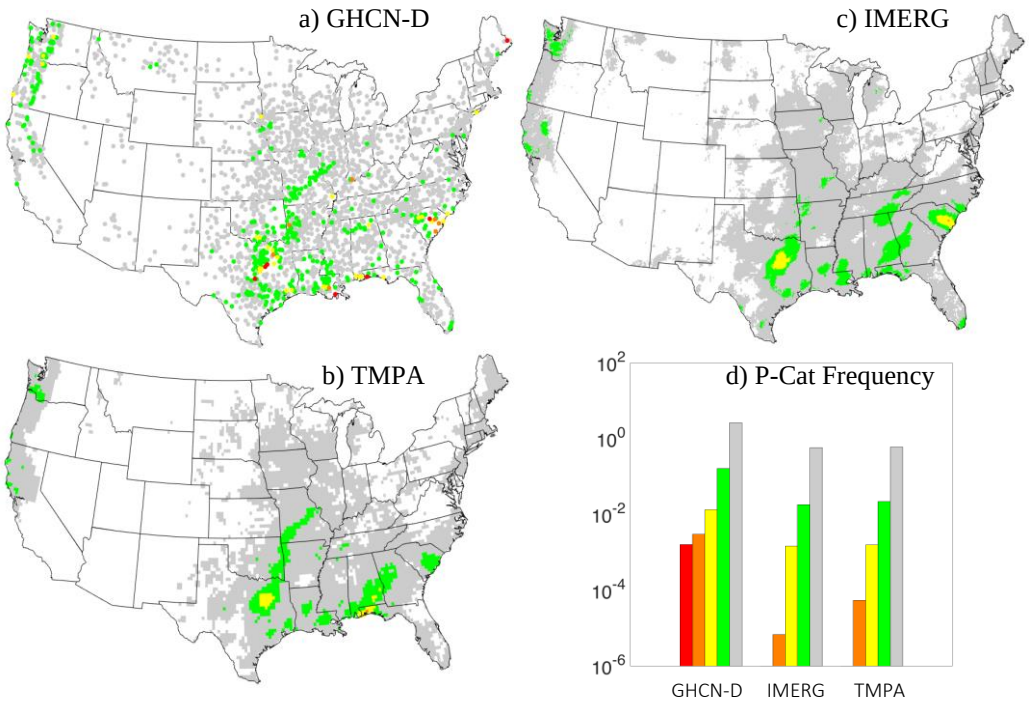

Figure 2.15 Maximum observed P-Cats during April 2014-December 2015, the TMPA/IMERG overlap period. Results are for (a) GHCN-D, (b) IMERG, (c) TMPA, (d) Annual frequency per grid cell/station observed over time record.

Chapter 3 Figures

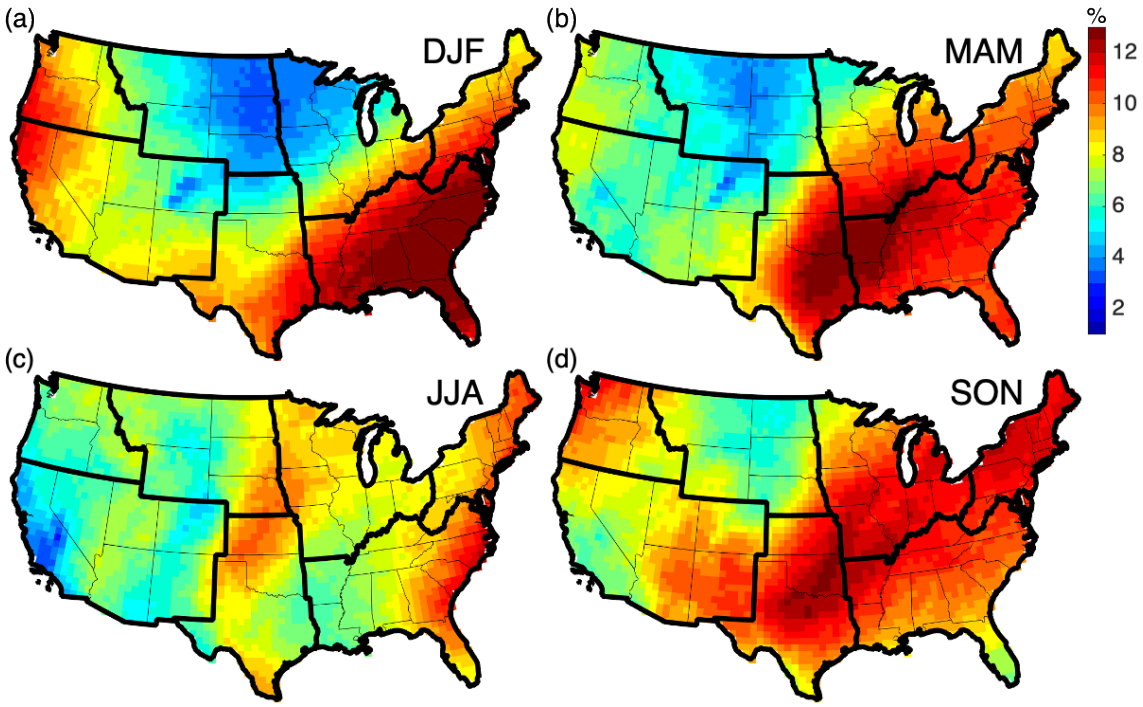

Figure 3.1 AR frequency (% of days) between 1981-2016 at each grid cell. Results are for (a) December, January, and February; (b) March, April, and May; (c) June, July, and August; and (d) September, October, and November.

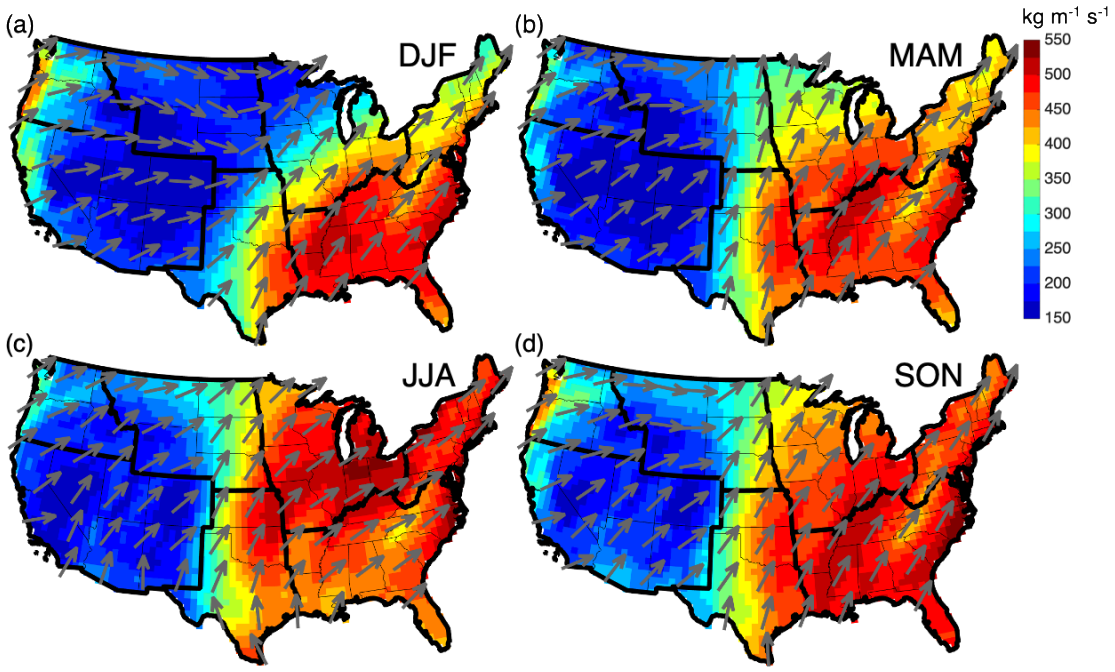

Figure 3.2 Mean IVT (kg m-1 s-1; shading) and mean IVT direction (arrows) for AR days between 1981-2016 at each grid cell. Results are for (a) December, January, and February; (b) March, April, and May; (c) June, July, and August; and (d) September, October, and November.

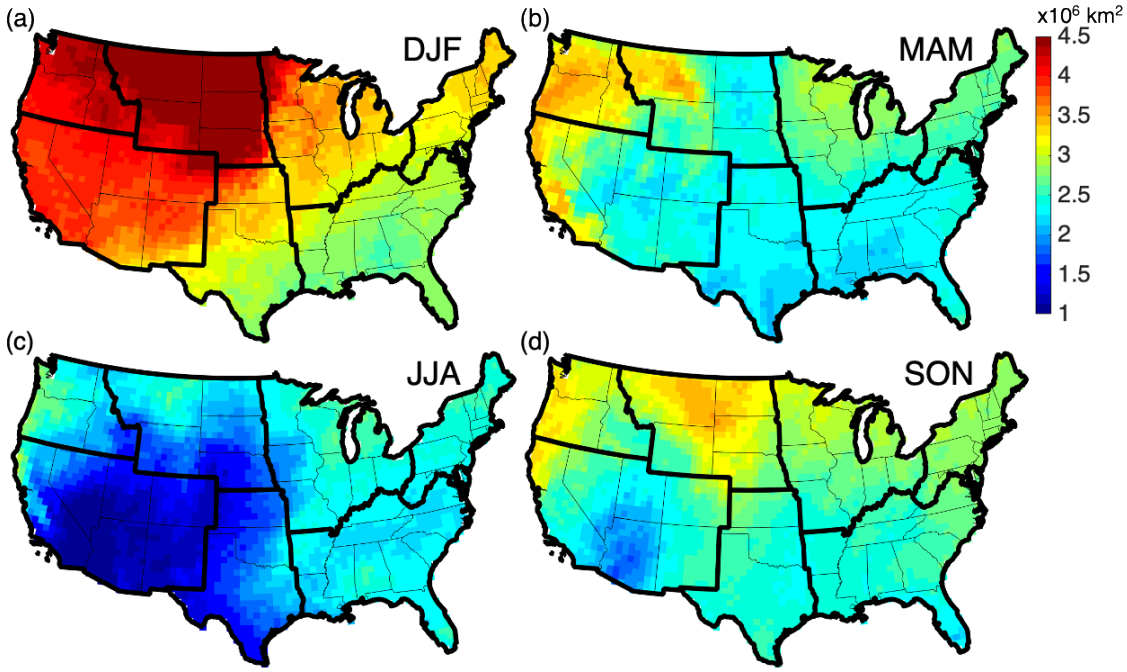

Figure 3.3 Median AR area (x10^6 km^2) between 1981-2016 at each grid cell. Results are for (a) December, January, and February; (b) March, April, and May; (c) June, July, and August; and (d) September, October, and November.

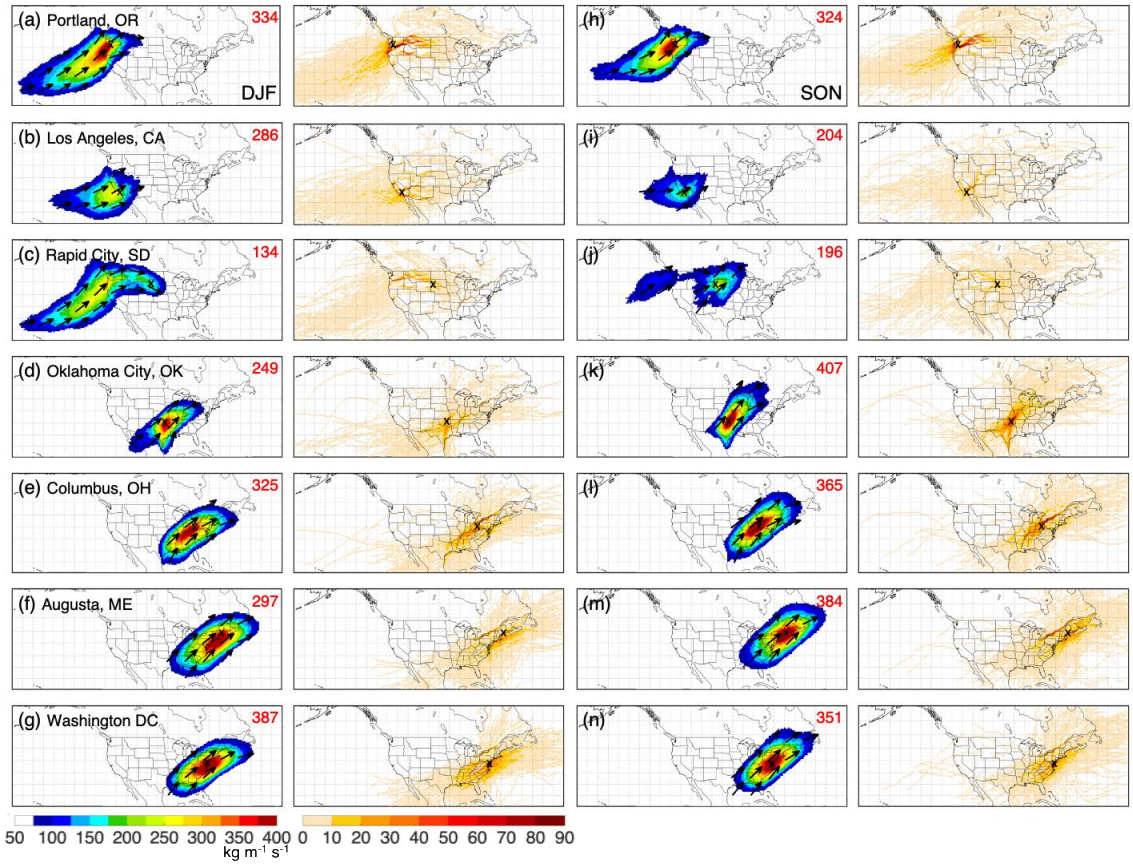

Figure 3.4 AR composites for cities, denoted by black 'x', in each of the 7 NCA regions. Composite IVT (kg m-1 s-1) and mean IVT direction (vectors) for all AR days between 1981-2016 at each grid cell (columns 1&3). AR day count per season is denoted in red in the top right corner in each city composite panel. AR axis density for all AR days 1981-2016 at each grid cell (columns 2&4). Results are for December, January, and February (columns 1&2); and September, October, and November (columns 3&4).

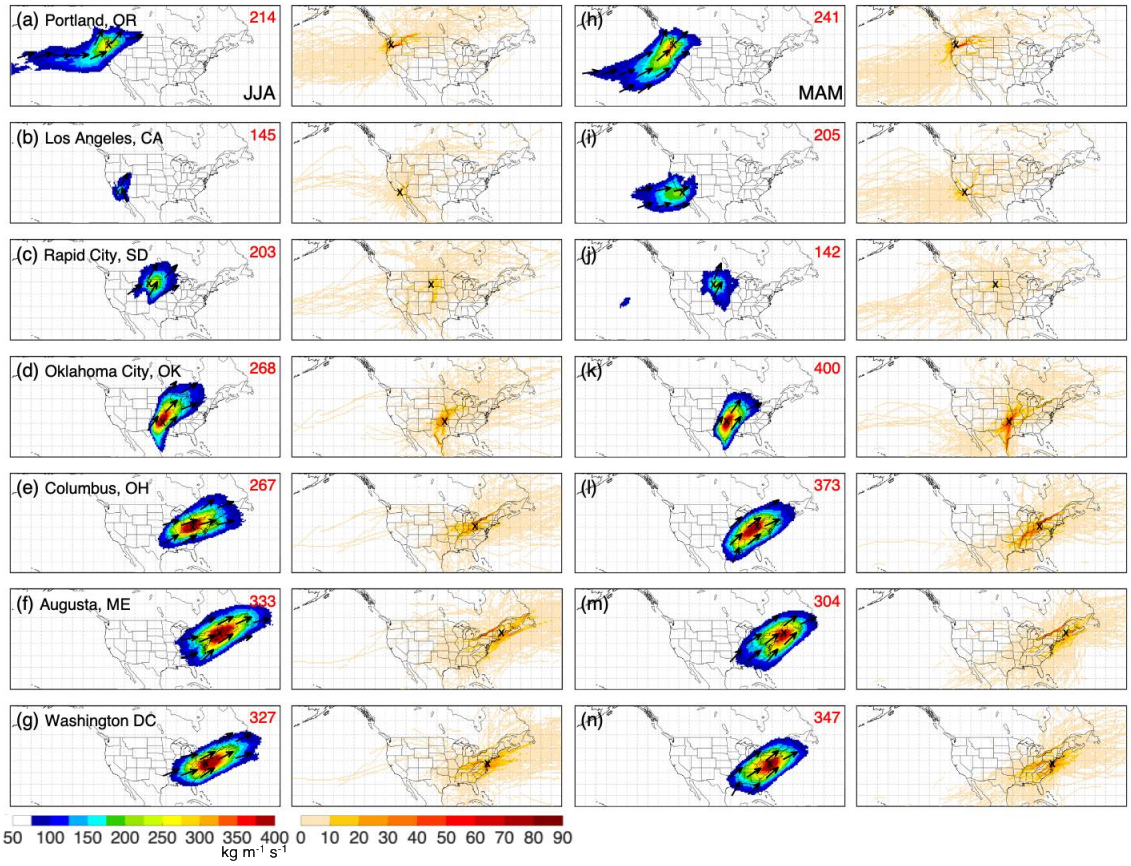

Figure 3.5 Same as in Figure 3.4 except results are for June, July, and August (columns 1&2); and March, April, and May (columns 3&4).

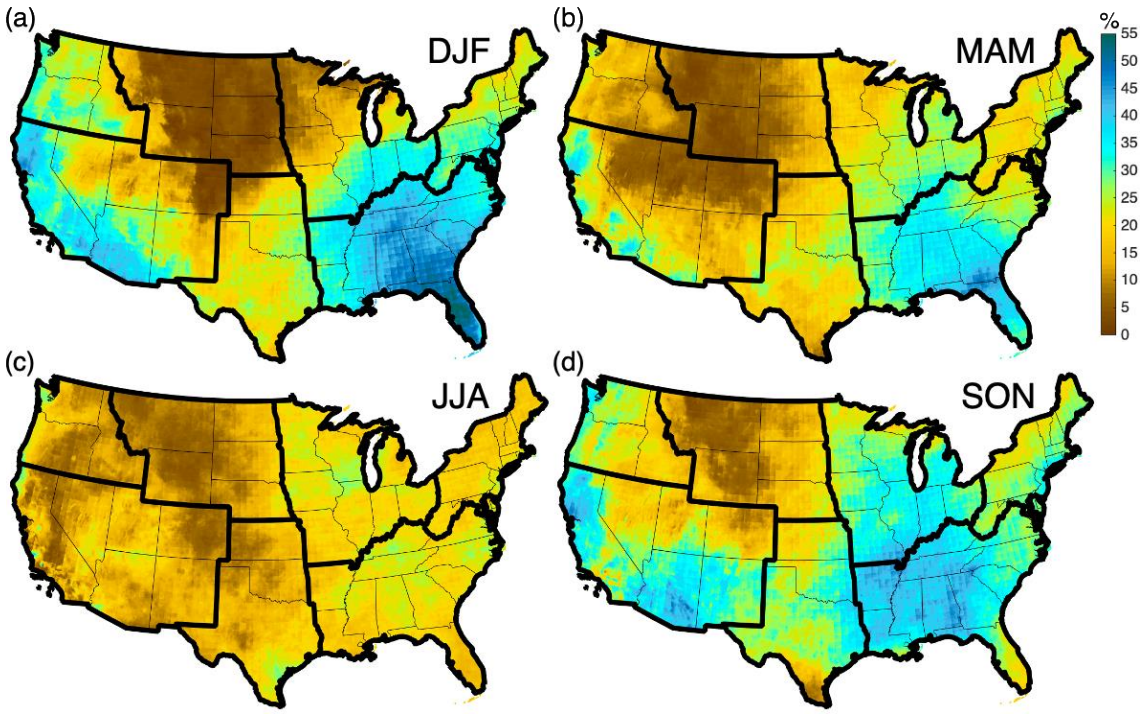

Figure 3.6 AR precipitation fraction calculated as the percent of AR-driven precipitation relative to the total precipitation between 1981-2016 at each grid cell. Results are for (a) December, January, and February; (b) March, April, and May; (c) June, July, and August; and (d) September, October, and November.

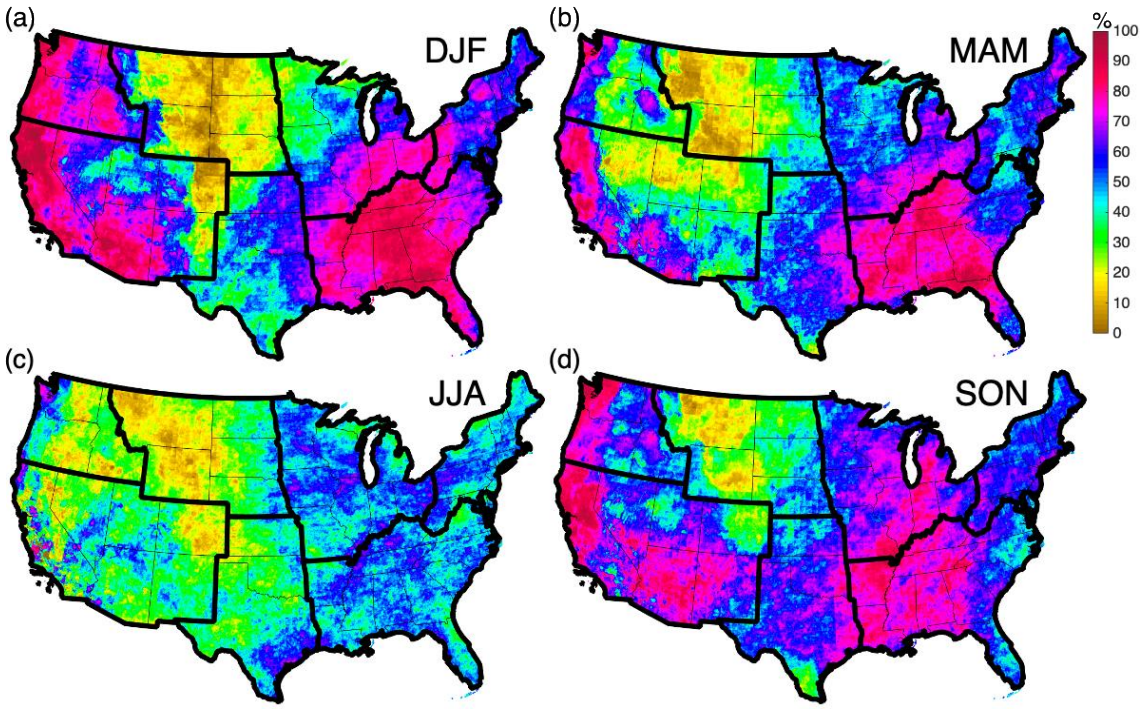

Figure 3.7 AR extreme precipitation fraction (% of days) calculated as the number of linked 95th percentile extreme precipitation AR days relative to the total number of 95th percentile extreme precipitation days between 1981-2016 at each grid cell. Results are for (a) December, January, and February; (b) March, April, and May; (c) June, July, and August; and (d) September, October, and November.

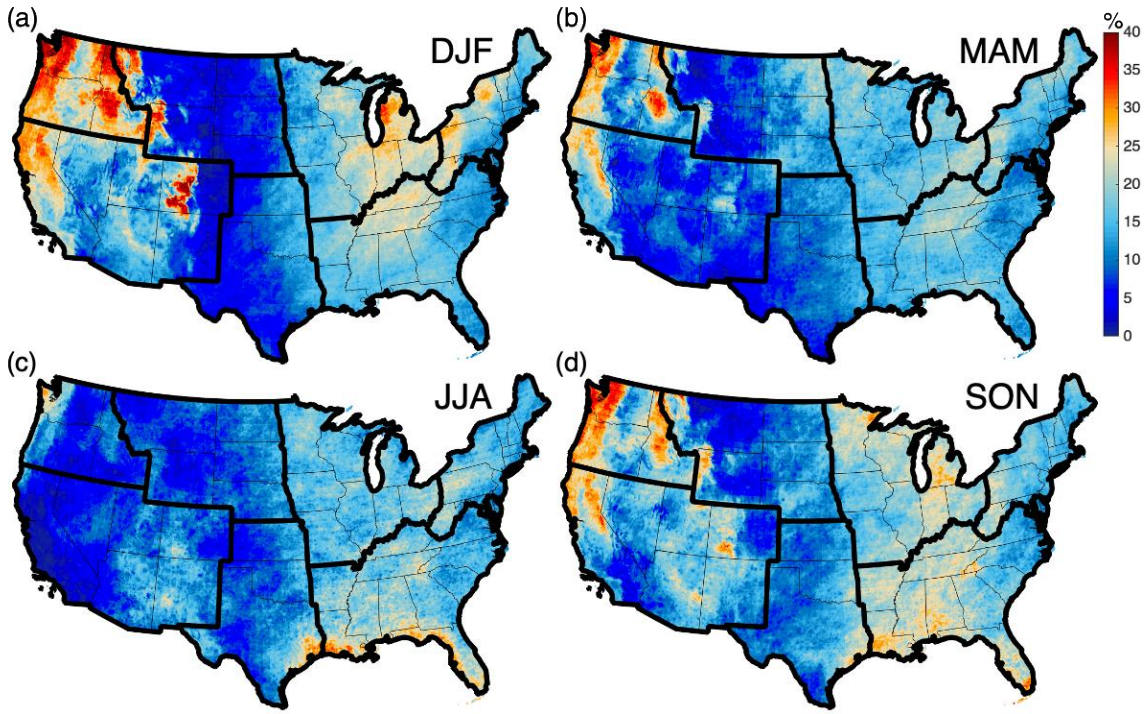

Figure 3.8 AR fraction (% of days) calculated as the number of linked AR 95th percentile extreme precipitation days relative to the total number of AR days between 1981-2016 at each grid cell. Results are for (a) December, January, and February; (b) March, April, and May; (c) June, July, and August; and (d) September, October, and November.

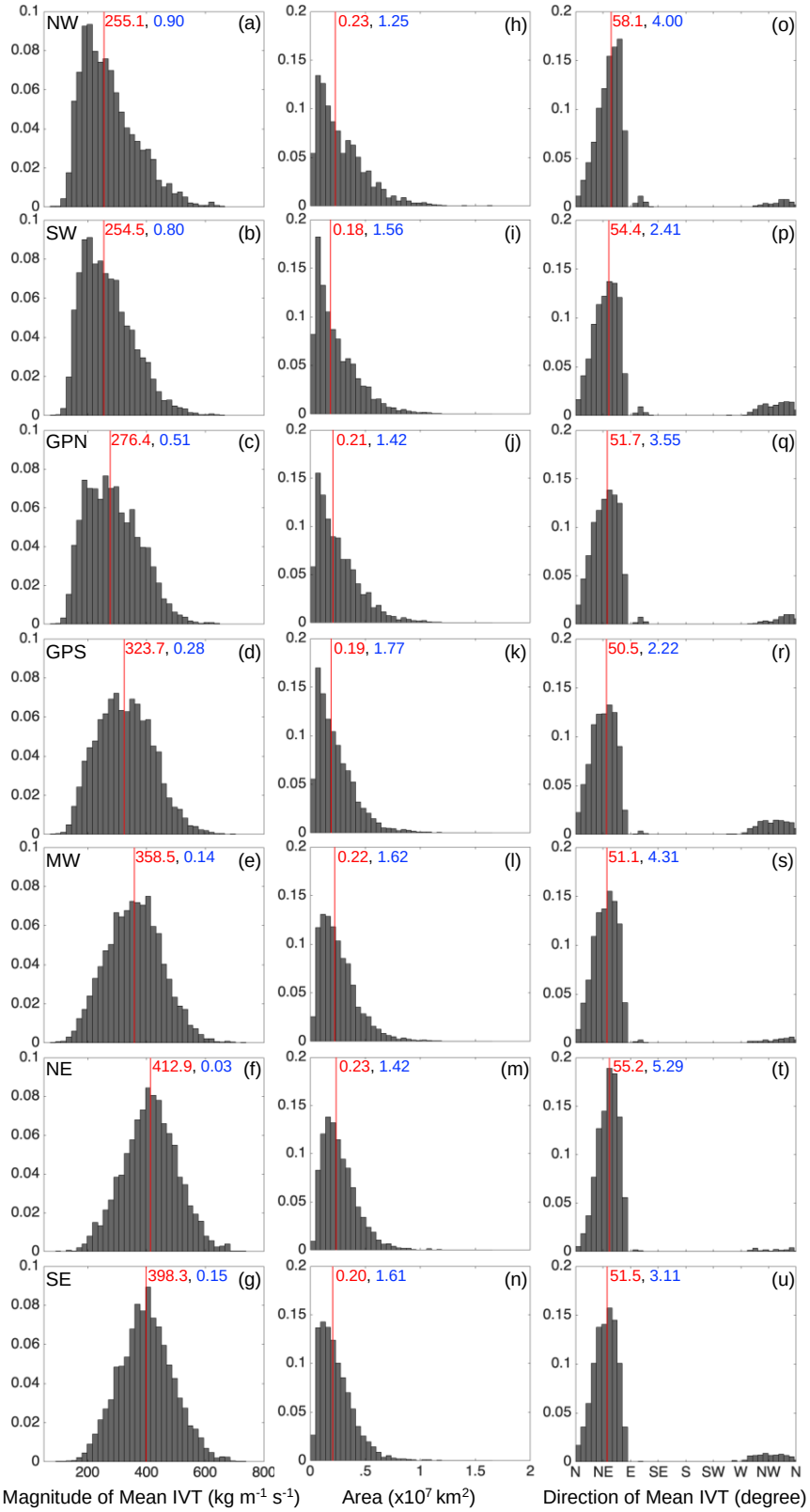
NW 255.1, 0.90 (a)
SW 254.5, 0.80 (b)
GPN 276.4, 0.51 (c)
GPS 323.7, 0.28 (d)
MW 358.5, 0.14 (e)
NE 412.9, 0.03 (f)
SE 398.3, 0.15 (g)
0.23, 1.25 (h)
0.18, 1.56 (i)
0.21, 1.42 (j)
0.19, 1.77 (k)
0.22, 1.62 (l)
0.23, 1.42 (m)
0.20, 1.61 (n)
58.1, 4.00 (o)
54.4, 2.41 (p)
51.7, 3.55 (q)
50.5, 2.22 (r)
51.1, 4.31 (s)
55.2, 5.29 (t)
51.5, 3.11 (u)
200 400 600 800
0 .5 1 1.5 2
N NE E SE S SW W NW N
Magnitude of Mean IVT (kg m-1 s-1)
Area (x10^7 km^2)
Direction of Mean IVT (degree)

Figure 3.9 Histograms of basic characteristics of ARs detected over all months between 1981–2016. The red lines in each panel indicate the median. Results are for the magnitude of mean IVT (kg m^{-1} s^{-1}; column 1); AR area (x10^7 km^2; column 2); and direction of mean IVT (degree; column 3) for each of the seven NCA regions (rows).

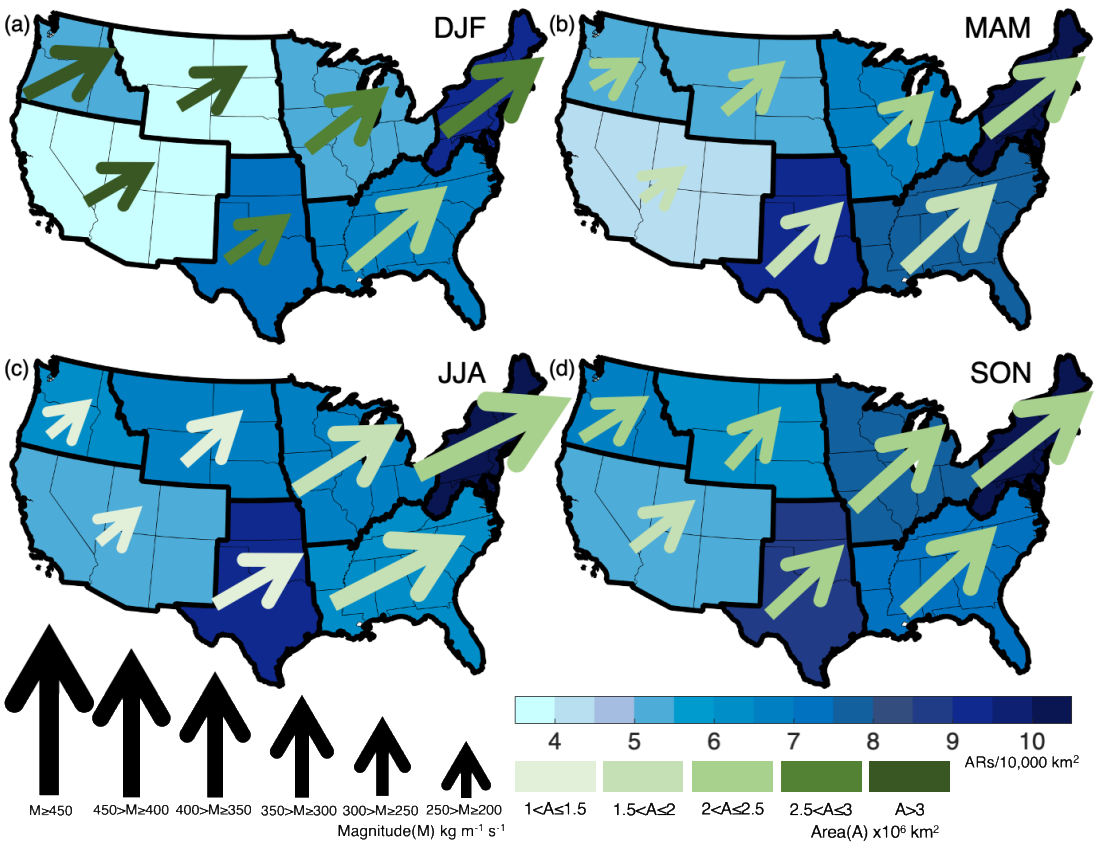

Figure 3.10 Summarized AR characteristics for each NCA region. AR occurrences per unit area (shading; number of AR days per season per 10,000 km2). Arrows represent median AR IVT direction (degree), IVT magnitude (arrow size; kg m-1 s-1), and median AR area (x106 km2; arrow shading). ARs in each region are identified under the condition that at least 10% of the grid cells of the AR shape are within the region boundaries. Results are for (a) December, January, and February; (b) March, April, and May; (c) June, July, and August; and (d) September, October, and November.

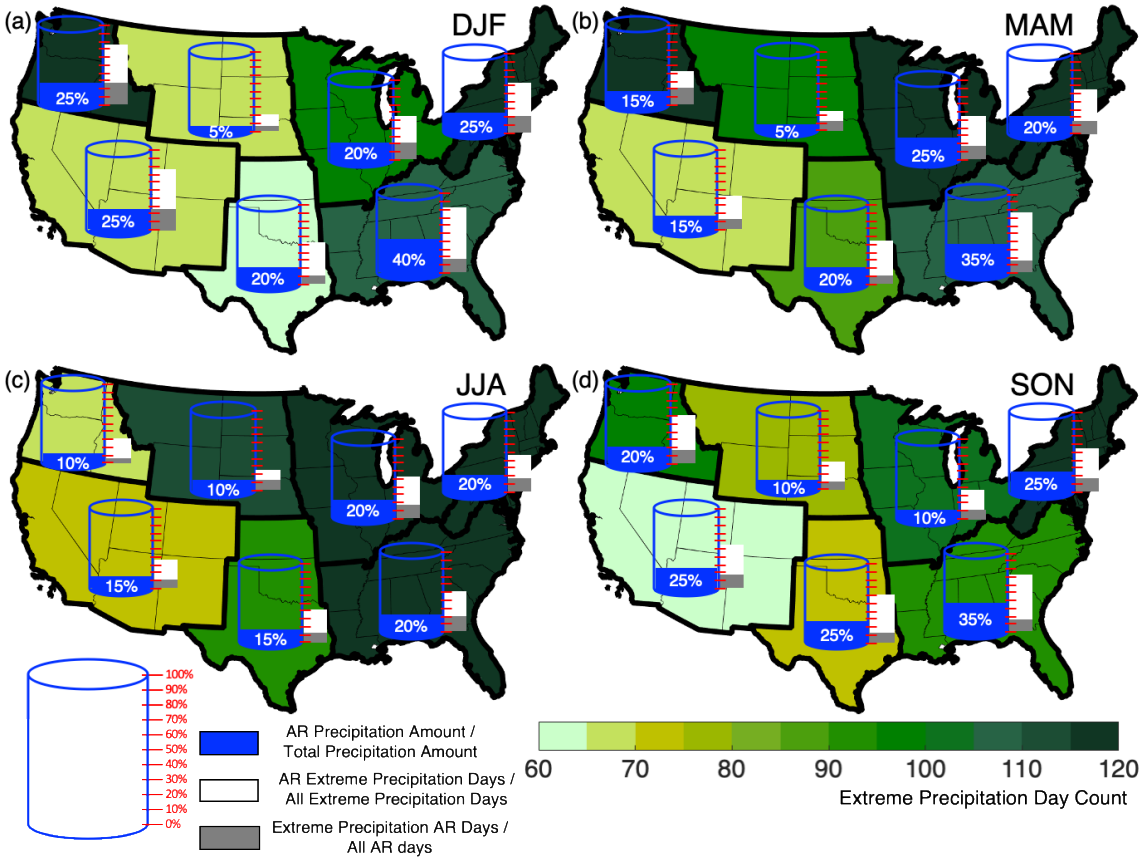
(a)
DJF
25%
5%
25%
20%
25%
40%
20%
(b)
MAM
15%
5%
25%
20%
15%
35%
20%
(c)
JJA
10%
10%
20%
20%
15%
20%
15%
(d)
SON
20%
10%
25%
10%
25%
35%
25%
100%
90%
80%
70%
60%
50%
40%
30%
20%
10%
0%
AR Precipitation Amount / Total Precipitation Amount
AR Extreme Precipitation Days / All Extreme Precipitation Days
Extreme Precipitation AR Days / All AR days
60
70
80
90
100
110
120
Extreme Precipitation Day Count

Figure 3.11 Summarized AR precipitation characteristics for each NCA region. Extreme precipitation day frequency calculated as the spatial median of the total number of qualifying days that occurred during each season at each grid cell across each region. AR precipitation fraction, calculated as the percent of AR-driven precipitation relative to the total precipitation is illustrated as the water level in a bucket. AR extreme precipitation fraction (% of days) calculated as the number of linked 95th percentile extreme precipitation AR days relative to the total number of 95th percentile extreme precipitation (white bar) and AR fraction (% of days) calculated as the number of linked AR 95th percentile extreme precipitation days relative to the total number of AR days (gray bar) between 1981-2016 at each grid cell. Results are for (a) December, January, and February; (b) March, April, and May; (c) June, July, and August; and (d) September, October, and November.

Chapter 4 Figures

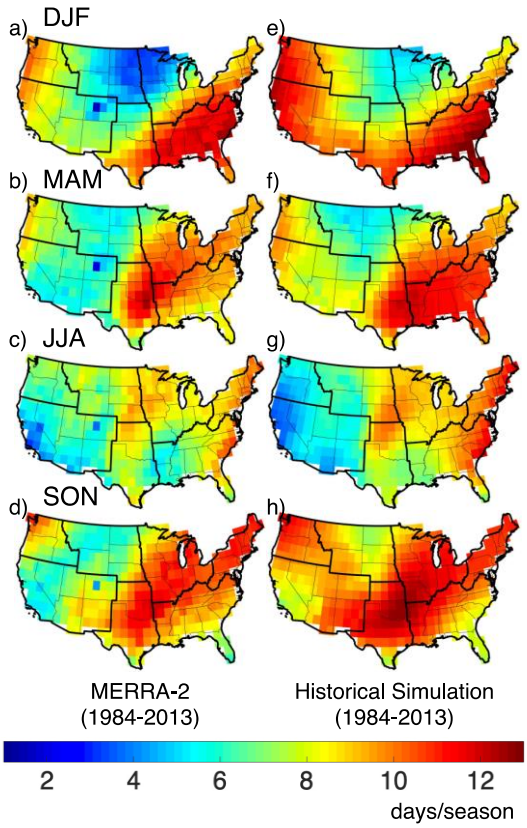

Figure 4.1 AR day frequency (days/season) calculated at each grid cell for (a-d) MERRA-2 and (e-h) the multi-model mean for the 5 CMIP6 models analyzed in this study for the historical period (1984-2013).

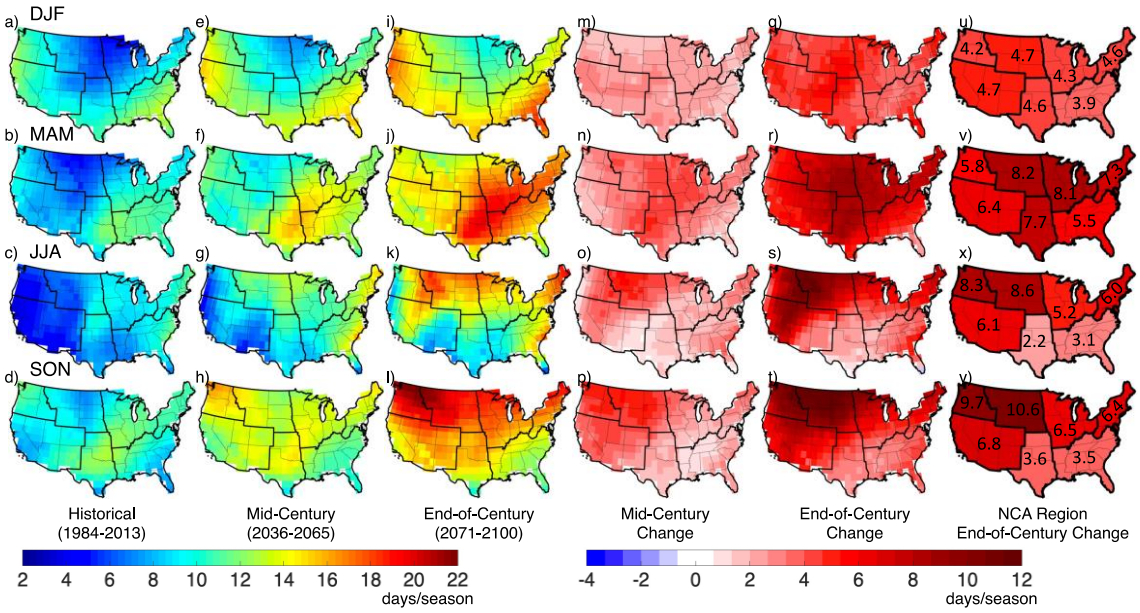

Figure 4.2 Multi-model mean AR day frequency (days/season) at each grid point for the (a-d) historical period (1984-2013); (e-h) mid-century (2071-2100) SSP 585 warming scenario; (i-l) end-of-century (2071-2100) SSP 585 warming scenario; (m-p) mid-century change (col. 2 minus col. 1); (q-t) end-of-century change (col. 3 minus col. 1); and (u-y) regional mean end-of-century change. Results are for December, January, and February (DJF); March, April, and May (MAM); (c) June, July, and August (JJA); and September, October, and November (SON).

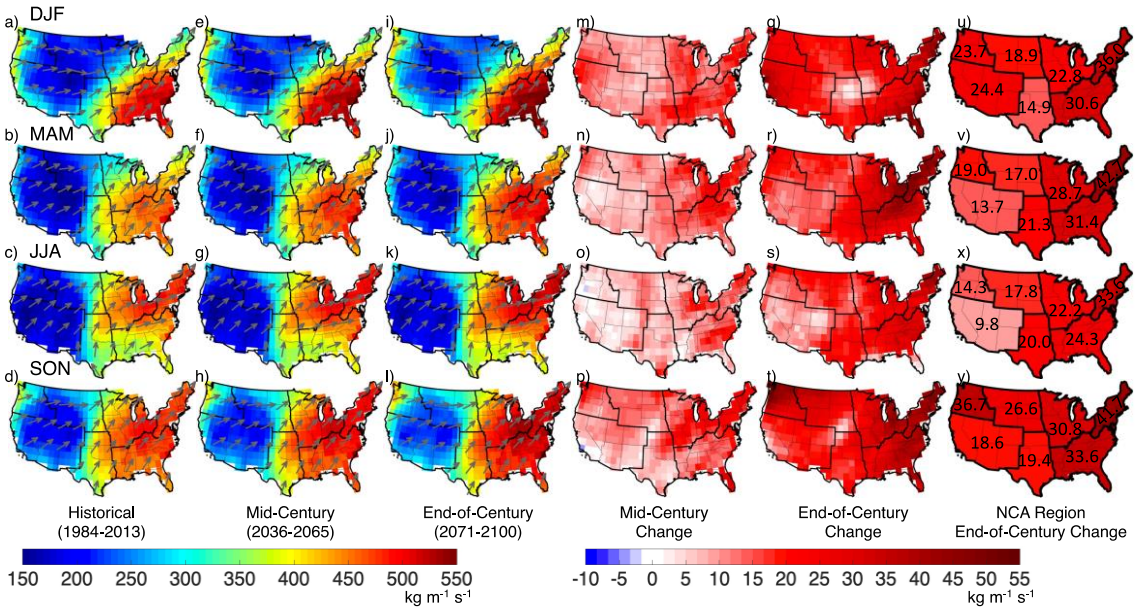

Figure 4.3 Multi-model mean AR IVT magnitude (kg m^{-1} s^{-1}) and direction (arrows) at each grid point for the (a-d) historical period (1984-2013); (e-h) mid-century (2071-2100) SSP 585 warming scenario; (i-l) end-of-century (2071-2100) SSP 585 warming scenario; (m-p) mid-century change (col. 2 minus col. 1); (q-t) end-of-century change (col. 3 minus col. 1); and (u-y) regional mean end-of-century change. Results are for December, January, and February (DJF); March, April, and May (MAM); (c) June, July, and August (JJA); and September, October, and November (SON).

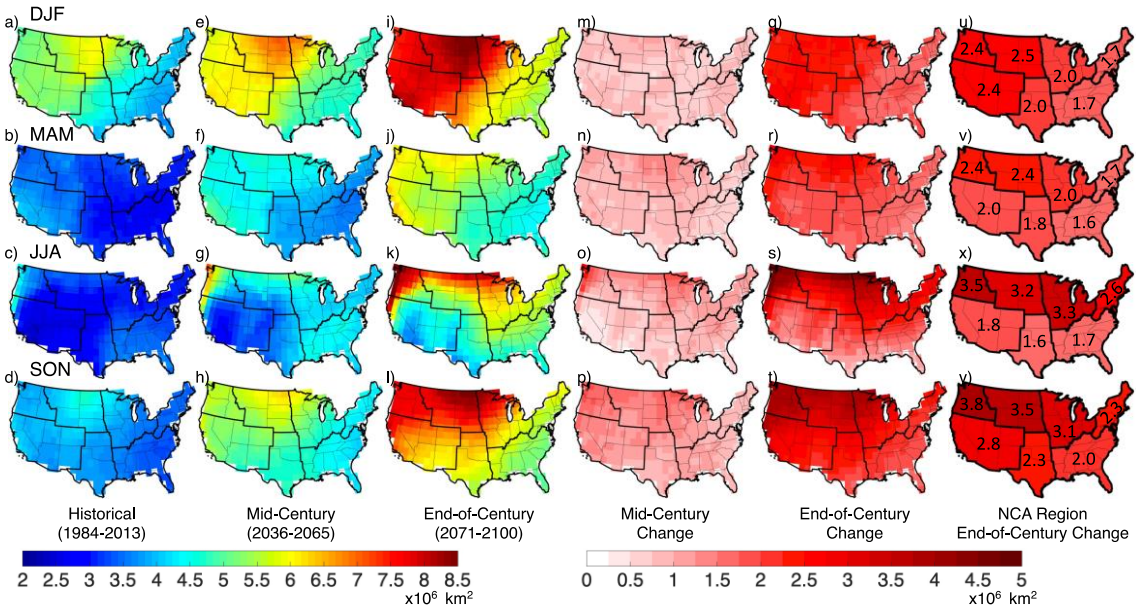

Figure 4.4 Multi-model mean median AR area ($x10^6$ km^2) at each grid point for the (a-d) historical period (1984-2013); (e-h) mid-century (2071-2100) SSP 585 warming scenario; (i-l) end-of-century (2071-2100) SSP 585 warming scenario; (m-p) mid-century change (col. 2 minus col. 1); (q-t) end-of-century change (col. 3 minus col. 1); and (u-y) regional mean end-of-century change. Results are for December, January, and February (DJF); March, April, and May (MAM); (c) June, July, and August (JJA); and September, October, and November (SON).

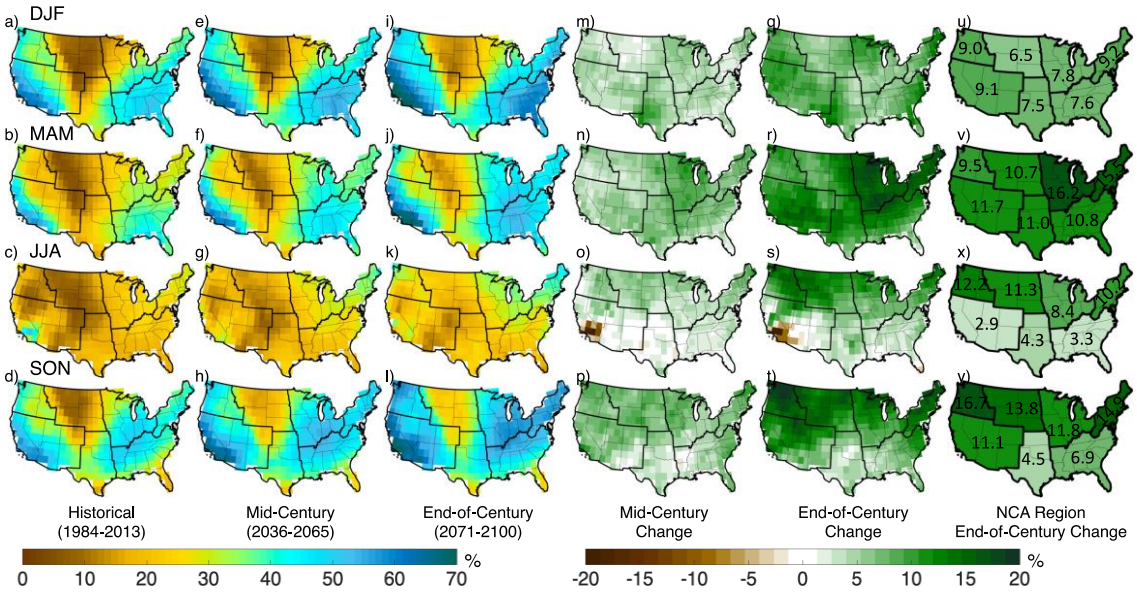

Figure 4.5 Multi-model mean AR precipitation fraction (%) calculated as the percent of AR-driven precipitation relative to the total precipitation at each grid point for the (a-d) historical period (1984-2013); (e-h) mid-century (2071-2100) SSP 585 warming scenario; (i-l) end-of-century (2071-2100) SSP 585 warming scenario; (m-p) mid-century change (col. 2 minus col. 1); (q-t) end-of-change (col. 3 minus col. 1); and (u-y) regional mean end-of-century change. Results are for December, January, and February (DJF); March, April, and May (MAM); (c) June, July, and August (JJA); and September, October, and November (SON).

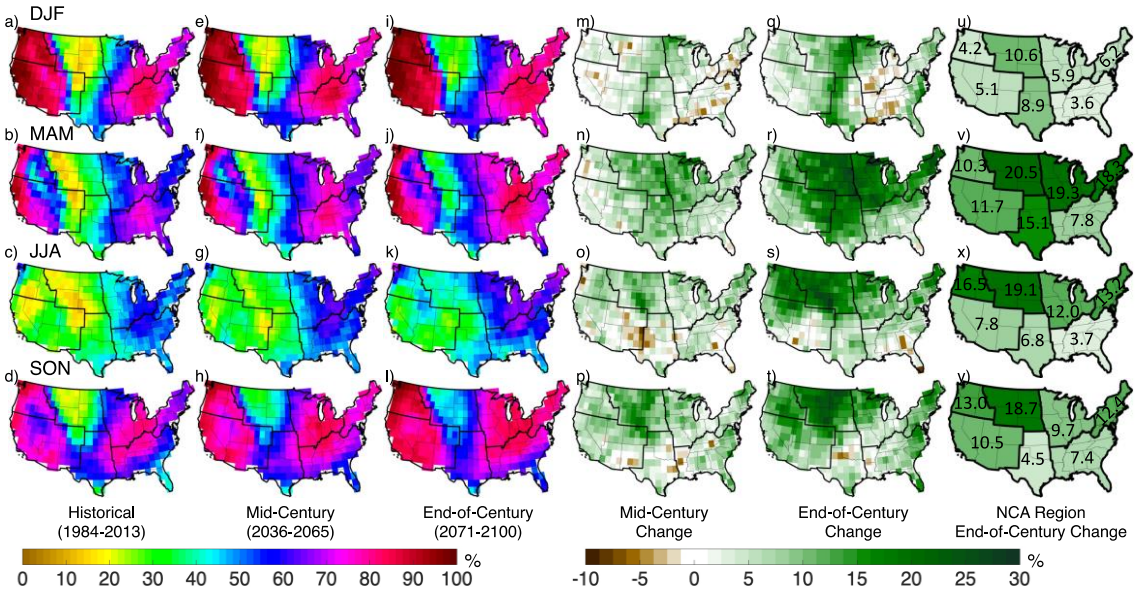

Figure 4.6 Multi-model mean AR extreme precipitation fraction (% of days) calculated as the number of linked AR 95th percentile extreme precipitation days relative to the total number of extreme precipitation days for the (a-d) historical period (1984-2013); (e-h) mid-century (2071-2100) SSP 585 warming scenario; (i-l) end-of-century (2071-2100) SSP 585 warming scenario; (m-p) mid-century change (col. 2 minus col. 1); (q-t) end-of-century change (col. 3 minus col. 1); and (u-y) regional mean end-of-century change. Results are for December, January, and February (DJF); March, April, and May (MAM); (c) June, July, and August (JJA); and September, October, and November (SON).

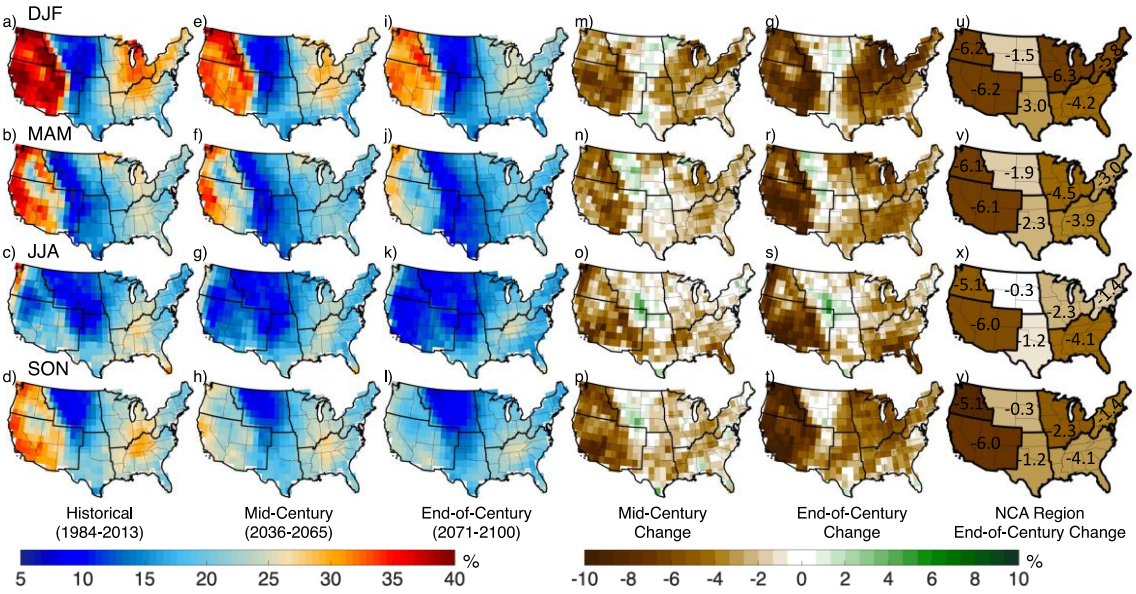

Figure 4.7 Multi-model mean AR fraction (% of days) calculated as the number of linked AR 95th percentile extreme precipitation days relative to the total number of AR days for the (a-d) historical period (1984-2013); (e-h) mid-century (2071-2100) SSP 585 warming scenario; (i-l) end-of-century (2071-2100) SSP 585 warming scenario; (m-p) mid-century change (col. 2 minus col. 1); (q-t) end-of-century change (col. 3 minus col. 1); and (u-y) regional mean end-of-century change. Results are for December, January, and February (DJF); March, April, and May (MAM); (c) June, July, and August (JJA); and September, October, and November (SON).

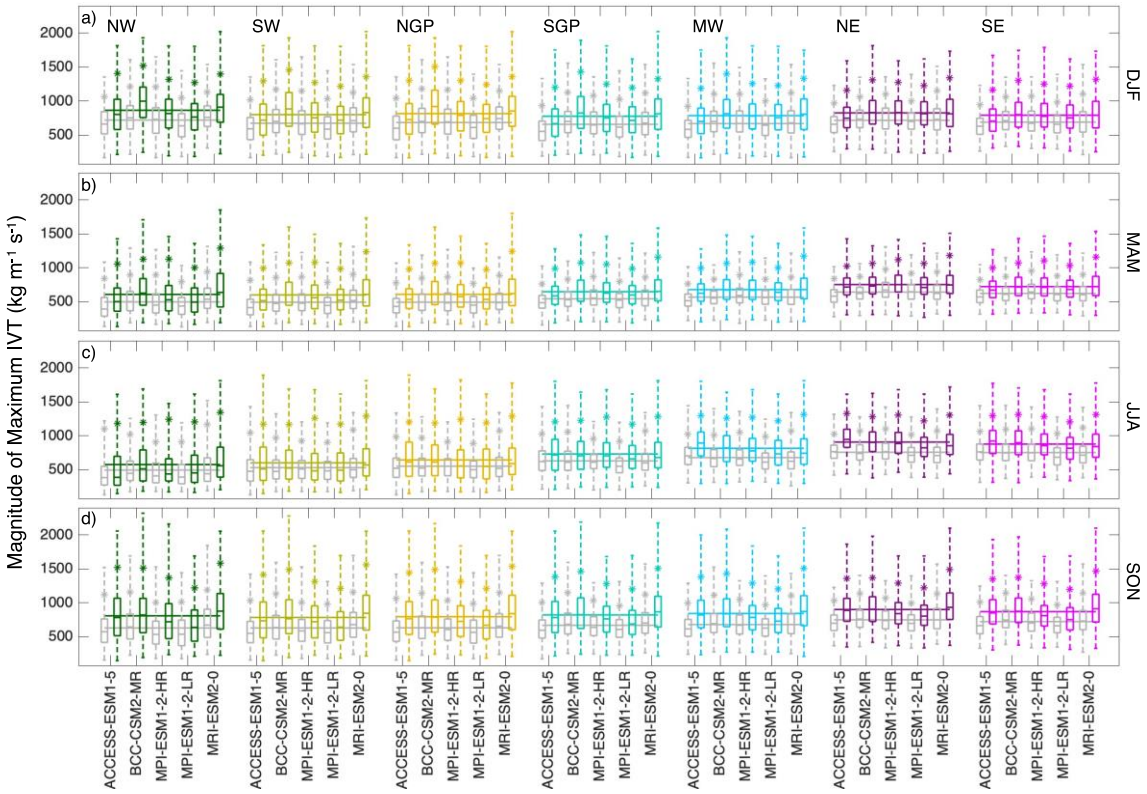

Figure 4.8 Boxplots representing the distribution of the magnitude of maximum IVT (kg m^{-1} s^{-1}) for ARs that had at least 10% of their grid points in a given NCA region for 5 CMIP6 models. Each model's end-of-century (2071-2100) distribution is illustrated in varying colors to distinguish between NCA region. The historical simulation distribution for a given model is depicted by a gray boxplot. The 95th percentile value for each model is denoted by an asterisk (*). The end-of-century (colored) and historical simulation (gray) multi-model mean is represented by a continuous line for each region. Results are for December, January, and February (DJF); March, April, and May (MAM); (c) June, July, and August (JJA); and September, October, and November (SON).

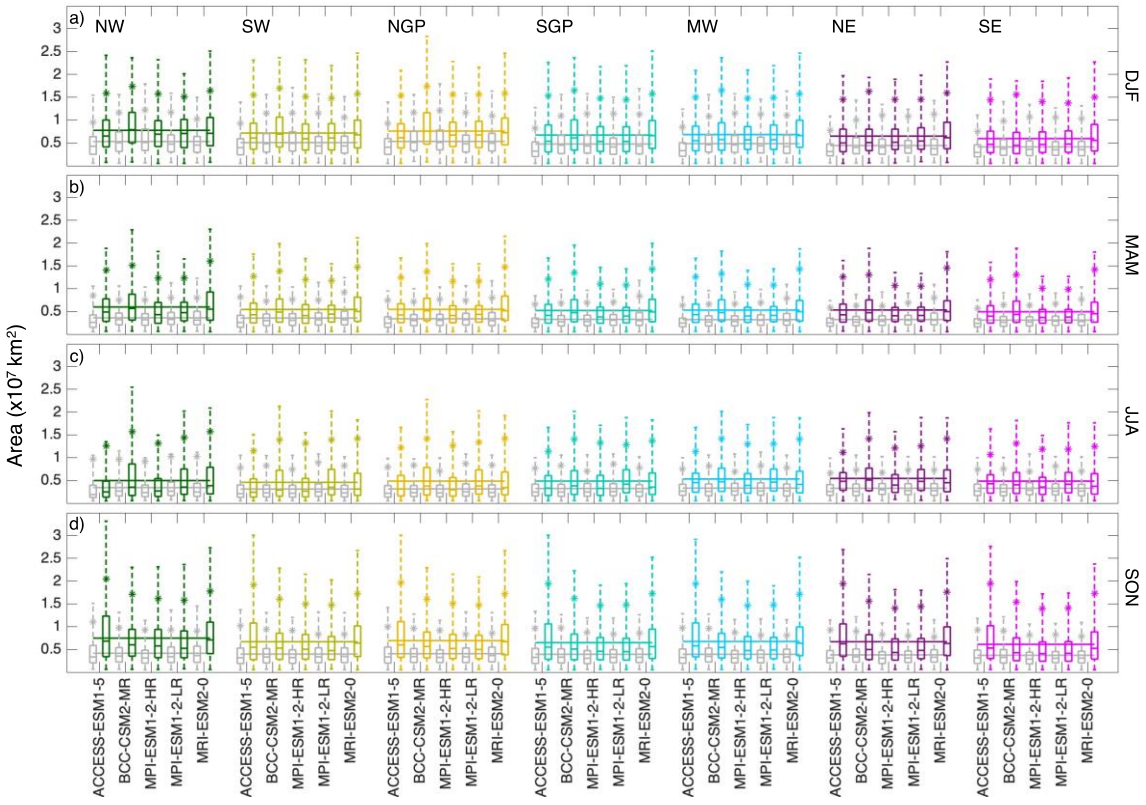

Figure 4.9 Same as in Figure 4.8 except results are for median AR area (x10^7 km^2).

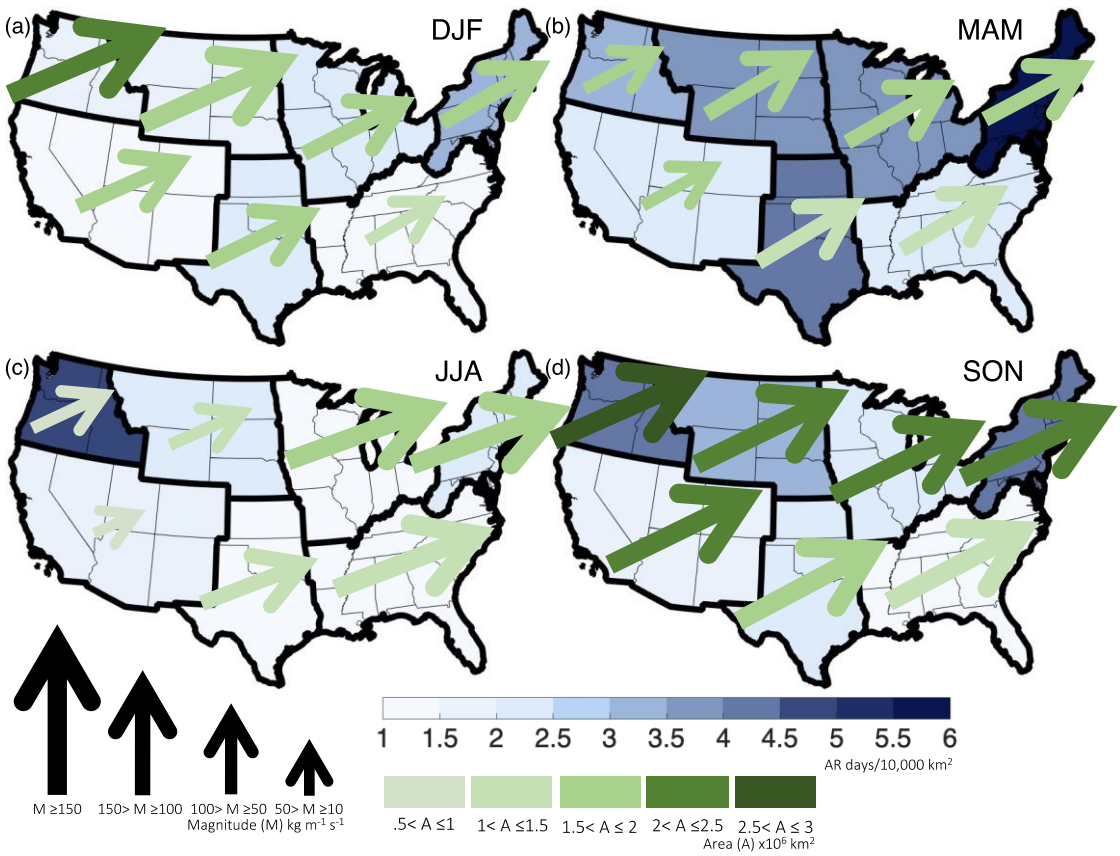

Figure 4.10 Summarized end-of-century change in multi-model mean AR characteristics by NCA region. Change in AR day count per unit area (shading; ARs/10,000 km^2) for ARs that had at least 10% of their grid points in a given region. Arrows represent end-of-century median AR IVT direction (degree), change in the magnitude of maximum IVT (arrow size; kg m^{-1} s^{-1}), and change in AR area (x10^6 km^2; arrow shading) by the end-of-century period (2071-2100). Results are for (a) December, January, and February; (b) March, April, and May; (c) June, July, and August; and (d) September, October, and November.

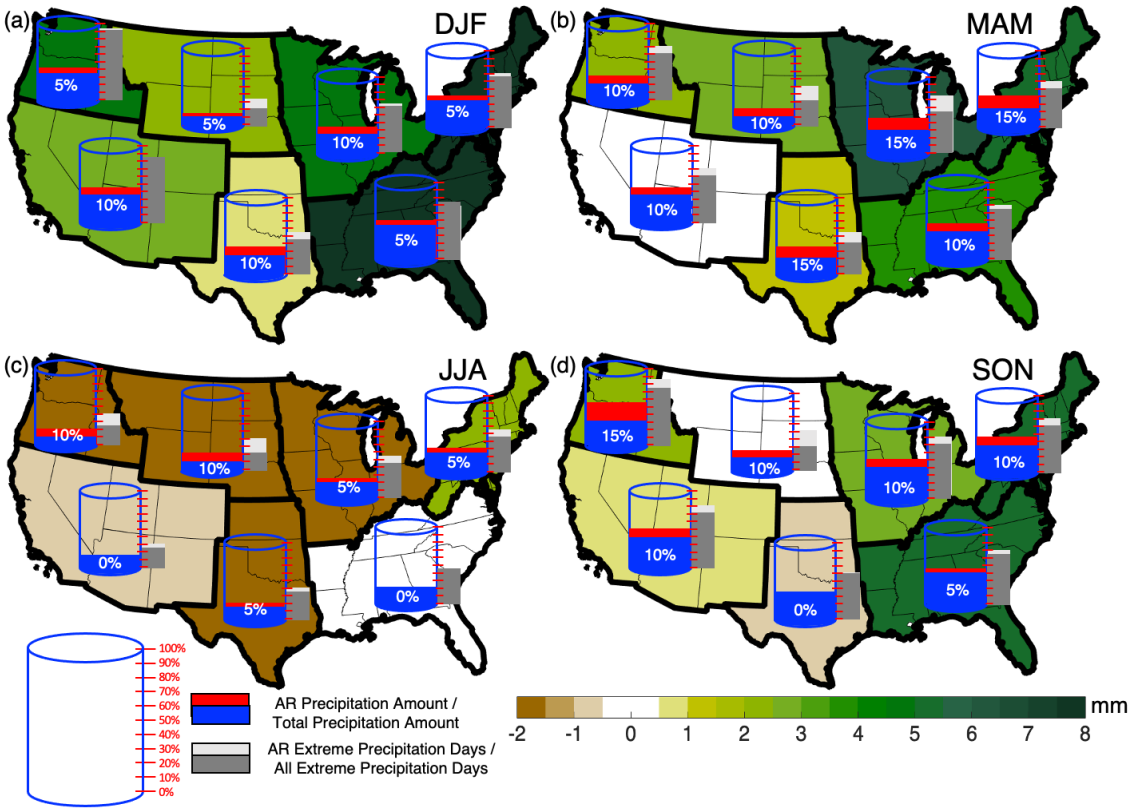

Figure 4.11 Summarized end-of-century change in multi-model mean AR characteristics by NCA region. Change in 95th percentile three-day precipitation totals by the end-of-century (shading; mm). The AR precipitation fraction, calculated as the percent of AR-driven precipitation relative to the total precipitation, is illustrated as the bucket water level and is shown for the historical period (1984-2013; blue), end-of-century SSP 585 warming scenario (2071-2100; red), and difference (labeled). The AR extreme precipitation fraction (% of days), calculated as the number of linked AR 95th percentile extreme precipitation days relative to the total number of extreme precipitation days, is shown for the historical period (1984-2013; dark gray bar) and end-of-century SSP 585 warming scenario (2071-2100; light gray bar).

References

Adler, R.F., C. Kidd, G. Petty, M. Morissey, and H.M. Goodman, 2001: Intercomparison of Global Precipitation Products: The Third Precipitation Intercomparison Project (PIP-3). *Bull. Amer. Meteor. Soc.*, **82**, 1377–1396, https://doi.org/10.1175/1520-0477(2001)082<1377:IOGPPT>2.3.CO;2.

Alexander, L. V., and Coauthors, 2006: Global observed changes in daily climate extremes of temperature and precipitation. *J. Geophys. Res.*, **111**, D05109, doi:10.1029/2005JD006290.

Allen, M. R., and W. J. Ingram, 2002: Constraints on future changes in climate and the hydrological cycle. *Nature*, **419**, 224-232.

AMS, 2017: Atmospheric river, Glossary of Meteorology. [Available online at http://glossary.ametsoc.org/wiki/Atmospheric_river.]

Anderson, C.J. and R.W. Arritt, 2001: Mesoscale Convective Systems over the United States during the 1997–98 El Niño. *Mon. Wea. Rev.*, **129**, 2443–2457, https://doi.org/10.1175/1520-0493(2001)129<2443:MCSOTU>2.0.CO;2.

Behrangi, A., M. Lebsock, S. Wong, and B. Lambrigtsen, 2012: On the quantification of oceanic rainfall using spaceborne sensors, *J. Geophys. Res.*, **117**, doi:10.1029/2012JD017979.

Behrangi, A., K. Andreadis, J. B. Fisher, F. J. Turk, S. Granger, T. Painter, and N. Das, 2014a: Satellite-based precipitation estimation and its application for streamflow prediction over mountainous western U.S. basins. *J. Appl. Meteor. Climatol.*, **53**, 2823–2842, https://doi.org/10.1175/JAMC-D-14-0056.1.

Behrangi, A., Y. Tian, B. H. Lambrigtsen, and G. L. Stephens, 2014b: What does CloudSat reveal about global land precipitation detection by other spaceborne sensors?, *Water Resour. Res.*, **50**, 4893–4905, doi:10.1002/2013WR014566.

Behrangi, A., B. Guan, P. J. Neiman, M. Schreier, and B. Lambrigtsen, 2016: On the Quantification of Atmospheric Rivers Precipitation from Space: Composite Assessments and Case Studies over the Eastern North Pacific Ocean and the Western United States. *J. Hydrometeor.*, **17**, 369–382, https://doi.org/10.1175/JHM-D-15-0061.1.

Bharti, V., and C. Singh, 2015: Evaluation of error in TRMM 3B42V7 precipitation estimates over the Himalayan region. *J. Geophys. Res. Atmos.*, **120**, 12458–12473, https://doi.org/10.1002/2015JD023779.

Bolton, D. 1980. The computation of equivalent potential temperature. *Mon. Wea. Rev.*, **108**. 1046–1053.

Bosilovich, M. G., J. Chen, F. R. Robertson, and R. F. Adler, 2008: Evaluation of global precipitation in reanalyses. *J. Appl. Meteor. Climatol.*, **47**, 2279–2299.

Bosilovich, M. G., R. Lucchesi, and M. Suarez, 2016: MERRA-2: File specification. GMAO Office Note 9, 73 pp. [Available online at https://gmao.gsfc.nasa.gov/pubs/docs/Bosilovich785.pdf.]

Budikova, D., J.S.M. Coleman, S.A. Strope, and A. Austin, 2010: Hydroclimatology of the 2008 Midwest floods. *Water Resour. Res.*, **46**, W12524, https://doi.org/10.1029/2010WR009206.

Bukovsky, M. S. and D. J. Karoly, 2007: A Brief Evaluation of Precipitation from the North American Regional Reanalysis. *J. Hydrometeor.*, **8**, 837–846, https://doi.org/10.1175/JHM595.1.

Businger, S., D.I. Knapp, and G.F. Watson, 1990: Storm Following Climatology of Precipitation Associated with Winter Cyclones Originating Over the Gulf of Mexico. *Wea. Forecasting*, **5**, 378–403, https://doi.org/10.1175/1520-0434(1990)005<0378:SFCOPA>2.0.CO;2.

Catalano, A. J., P. C. Loikith, and C. M. Aragon, 2019: Spatiotemporal variability of twenty-first-century changes in site-specific snowfall frequency over the Northwest United States. *Geophysical Research Letters*, **46**(16), 10122-10131, https://doi.org/10.1029/2019GL084401.

Catto, J. L., and S. Pfahl, 2013: The importance of fronts for extreme precipitation. *J. Geophys.*
Res., **19**, 10,791-10,801.

Chen, C.-T., and T. Knutson, 2008: On the verification and comparison of extreme rainfall indices from climate models. *J. Climate*, **21**, 1605–1621.

Chen, S., Y. Hong, J. J. Gourley, G. J. Huffman, Y. Tian, Q. Cao, B. Yong, P. E. Kirstetter, J. Hu, J. Hardy, Z. Li, S. I. Khan, and X. Xue, 2013: Evaluation of the successive V6 and V7 TRMM Multisatellite Precipitation Analysis over the continental United States. *Water Resour. Res.*, **49**, 8174–8186, doi:10.1002/2012WR012795.

Christensen, J.H. and O. B. Christensen, 2003: Climate modelling: Severe summertime flooding in Europe. *Nature*, **421**, 805–806.

Collow, A. B. M., H. Mersiovsky, H., and M. G. Bosilovich, 2020: Large-Scale Influences on Atmospheric River–Induced Extreme Precipitation Events along the Coast of Washington State. *Journal of Hydrometeorology*, **21**(9), 2139-2156.

Corringham, T.W., F.M. Ralph, A. Gershunov, D.R. Cayan, and C.A. Talbot, 2019: Atmospheric rivers drive flood damages in the western United States. *Science Advances*, **5(12)**, eaax4631, https://doi.org/10.1126/sciadv.aax4631.

Curry, C. L., S. U. Islam, F. W. Zwiers, and S. J. Déry, 2019: Atmospheric rivers increase future flood risk in Western Canada's largest pacific river. *Geophys. Res. Lett.*, **46**, 1651–1661.

Dacre, H. F., P. A. Clark, O. Martinez-Alvarado, M. A. Stringer, and D. A. Lavers, 2015: How Do Atmospheric Rivers Form? *Bull. Amer. Meteor. Soc.*, **96**, 1243-1255.

Daly, C., R. P. Neilson, and D. L. Phillips, 1994: A statistical–topographic model for mapping climatological precipitation over mountainous terrain. *J. Appl. Meteor.*, **33**, 140–158.

Daly, C., W. P. Gibson, G. H. Taylor, G.L. Johnson, and P. Pasteris, 2002: A knowledge-based approach to the statistical mapping of climate. *Climate Res.*, **22**, 99-113, doi:10.3354/cr022099.

Daly, C., 2006: Guidelines for assessing the suitability of spatial climate data sets. *Int. J. Climatol.*, **26**, 707–721.

Daly, C., W.P. Gibson, G.H. Taylor, M.K. Doggett, and J.I. Smith, 2007: Observer Bias in Daily Precipitation Measurements at United States Cooperative Network Stations. *Bull. Amer. Meteor. Soc.*, **88**, 899–912, https://doi.org/10.1175/BAMS-88-6-899.

Daly, C., M. Halbleib, J. I. Smith, W. P. Gibson, M. K. Doggett, G. H. Taylor, J. Curtis, ad P. P. Pasteris, 2008: Physiographically sensitive mapping of climatological temperature and precipitation across the conterminous United States. *Int. J. Climatol.*, **28**, 2031-2064, doi:10.1002/joc.1688.

Debbage, N., P. Miller, S. Poore, K. Morano, T. Mote, and J. Marshall Shepherd, 2017: A climatology of atmospheric river interactions with the southeastern United States coastline. *Int. J. Climatol.*, **37**, 4077–4091, https://doi.org/10.1002/joc.5000.

Demaria, E. M. C., F. Dominguez, H. Hu, G. von Glinski, M. Robles, J. Skindlov, and J. Walter, 2017: Observed hydrologic impacts of landfalling atmospheric rivers in the Salt and Verde River basins of Arizona, United States. *Water Resour. Res.*, **53**, 10 025–10 042, https://doi.org/10.1002/2017WR020778.

Dettinger, M.D., 2011: Climate change, atmospheric rivers and floods in California—A multimodel analysis of storm frequency and magnitude changes. *J. Amer. Water Resour. Assoc.*, **47**, 514–523, doi:10.1111/j.1752-1688.2011.00546.x.

Dettinger, M.D., F. M. Ralph, T. Das, P.J. Neiman, and D.R. Cayan, 2011: Atmospheric rivers, floods, and the water resources of California, *Water*, **3**, 445–478, doi:10.3390/w3020445.

Dettinger, M.D., 2013: Atmospheric Rivers as Drought Busters on the U.S. West Coast. *J. Hydrometeor.*, **14**, 1721–1732, https://doi.org/10.1175/JHM-D-13-02.1.

Dettinger, M. D., F. M. Ralph, and J. J. Rutz, 2018: Empirical Return Periods of the Most Intense Vapor Transports during Historical Atmospheric River Landfalls on the U.S. West Coast. *J. Hydrometeor.*, **19**, 1363–1377, https://doi.org/10.1175/JHM-D-17-0247.1.

Diaconescu, E. P., P. Gachon, and R. Laprise, 2015: On the remapping procedure of daily precipitation statistics and indices used in regional climate model evaluation. *J. Hydrometeor.*, **16**, 2301–2310.

Dirmeyer, P.A., and J.L. Kinter, 2009: The "Maya Express": Floods in the U.S. Midwest. *Eos, Trans. Amer. Geophys. Union*, **90**, 101–102, doi:10.1029/2009EO120001.

Dirmeyer, P.A. and J.L. Kinter, 2010: Floods over the U.S. Midwest: A Regional Water Cycle Perspective. *J. Hydrometeor.*, **11**, 1172–1181, https://doi.org/10.1175/2010JHM1196.1.

Donat, M. G., L. V. Alexander, H. Yang, I. Durre, R. Vose, and J. Caesar, 2013: Global Land-Based Datasets for Monitoring Climate Extremes. *Bull. of the Amer. Met. Soc.*, **94**, 997-1006.

Donat, M.G., A. L. Lowry, L.V. Alexander, P. A. O'Gorman, and N. Maher, 2016: More extreme precipitation in the world's dry and wet regions. *Nat. Clim. Chang.*, **6**, 508–513.

Durre, I., M. J. Menne, B. E. Gleason, T. G. Houston, and R. S. Vose, 2010: Robust automated quality control of daily surface observations. *J. Appl. Meteor. Climatol.*, **49**, 1615–1633.

Easterling, D. R., J. L. Evans, P. Ya Groisman, T. R. Karl, K. E. Kunkel, and P. Ambenje, 2000: Observed variability and trends in extreme climate events: A brief review. *Bull. Amer. Meteor. Soc.*, **81**, 417–425.

Easterling, D. R., K. E. Kunkel, J. R. Arnold, T. Knutson, A. N. LeGrande, L. R. Leung, R. S. Vose, D. E. Waliser, and M. F. Wehner, 2017: Precipitation change in the United States. In: Climate Science Special Report: Fourth National Climate Assessment, Volume I [Wuebbles, D.J., D.W. Fahey, K.A. Hibbard, D.J. Dokken, B.C. Stewart, and T.K. Maycock (eds.)]. U.S. Global Change Research Program, Washington, DC, USA, pp. 207-230, doi:10.7930/J0H993CC.

Espinoza, V., D.E. Waliser, B. Guan, D.A. Lavers, and F.M. Ralph, 2018: Global analysis of climate change projection effects on atmospheric rivers. *Geophys. Res. Lett.*, **45**, 4299-4308, https://doi.org/10.1029/2017GL076968.

Eyring, V., S. Bony, G. A. Meehl, C. A. Senior, B. Stevens, R. J. Stouffer, and K. E. Taylor, 2016: Overview of the Coupled Model Intercomparison Project Phase 6 (CMIP6) experimental design and organization, *Geosci. Model Dev.*, **9**, 1937-1958, doi:10.5194/gmd-9-1937-2016.

Florsheim, J., and M. Dettinger, 2015: Promoting atmospheric-river and snowmelt-fueled biogeomorphic processes by restoring river-floodplain connectivity in California's Central Valley. *Geomorphic Approaches to Integrated Floodplain Management of Lowland Fluvial Systems in North America and Europe*, P. Hudson and H. Middelkoop, Eds., Springer, 119–141, https://doi.org/10.1007/978-1-4939-2380-9_6.

Frich, P., L. V. Alexander, P. Della-Marta, B. Gleason, M. Haylock, A. M. G. K. Tank, and T. Peterson, 2002: Observed coherent changes in climatic extremes during the second half of the twentieth century. *Climate Res.*, **19**, 193-212.

Fritsch, J. M., R. J. Kane, and C. R. Chelius, 1986: The Contribution of Mesoscale Convective
Weather Systems to the Warm-Season Precipitation in the United States. *Journal of Climate and Applied Meteorology*, **25**, 1333-1345.

Gao, Y., J. Lu, L. R. Leung, Q. Yang, S. Hagos, and Y. Qian, 2015: Dynamical and thermodynamical modulations on future changes of landfalling atmospheric rivers over western North America. *Geophys. Res. Lett.*, **42**, doi:10.1002/2015GL065435.

Gao, Y., Lu, J. and Leung, L. R, 2016: Uncertainties in projecting future changes in atmospheric rivers and their impacts on heavy precipitation over Europe. *J. Clim.*, **29**, 6711–6726.

Gelaro, R., W., and Coauthors, 2017: The Modern-Era Retrospective Analysis for Research and Applications, Version 2 (MERRA-2). *J. Climate*, **30**, 5419–5454, https://doi.org/10.1175/JCLI-D-16-0758.1.

Gershunov, A., and Coauthors, 2019: Precipitation regime change in Western North America: the role of atmospheric rivers. *Sci. Rep.*, **9**, 9944.

Giorgi, F., F. Raffaele, E. Coppola, 2019: The response of precipitation characteristics to global warming from climate projections. *Earth Syst. Dyn.*, **10**, 73–89.

Gleason, K. L., J. H. Lawrimore, D. H. Levinson, and T. R. Karl, 2008: A Revised U.S. Climate Extremes Index. *J. Climate*, **21**, 2124-2137.

Gershunov, A., T.Shulgina, F. M.Ralph, D. A.Lavers, and J. J.Rutz, 2017: Assessing the climate-scale variability of atmospheric rivers affecting western North America. *Geophys. Res. Lett.*, **44**, 7900–7908, https://doi.org/10.1002/2017GL074175.

Gershunov, A., and Coauthors, 2019: Precipitation regime change in western North America: The role of atmospheric rivers. *Nat. Sci. Rep.*, **9**, 9944, https://doi.org/10.1038/s41598-019-46169-w.

Guan, B., N. P. Molotch, D. E. Waliser, E. J. Fetzer, and P. J. Neiman, 2010: Extreme snowfall events linked to atmospheric rivers and surface air temperature via satellite measurements. *Geophys. Res. Lett.*, **37**, L20401, doi:20410.21029/22010GL044696.

Guan, B., N. P. Molotch, D. E. Waliser, E. J. Fetzer, and P. J. Neiman , 2013: The 2010/2011 snow season in California's Sierra Nevada: Role of atmospheric rivers and modes of large-scale variability. *Water Resources Research*, **49**, 6731-6743.

Guan, B., and D.E. Waliser, 2015: Detection of atmospheric rivers: Evaluation and application of an algorithm for global studies. *J. Geophys. Res. Atmos.*, **120**, 12 514–12 535, https://doi.org/10.1002/2015JD024257.

Guan, B., D. E.Waliser, F. M.Ralph, E. J.Fetzer, and P. J.Neiman, 2016: Hydrometeorological characteristics of rain-on-snow events associated with atmospheric rivers. *Geophys. Res. Lett.*, **43**, 2964–2973, https://doi.org/10.1002/2016GL067978.

Guan, B., and D.E. Waliser, 2017: Atmospheric rivers in 20 year weather and climate simulations: A multimodel, global evaluation. *J. Geophys. Res. Atmos.*, **122**, 5556–5581, https://doi.org/10.1002/2016JD026174.

Guan, B., D.E. Waliser, and F.M. Ralph, 2018: An Intercomparison between Reanalysis and Dropsonde Observations of the Total Water Vapor Transport in Individual Atmospheric Rivers. *J. Hydrometeor.*, **19**, 321–337, https://doi.org/10.1175/JHM-D-17-0114.1.

Guan, B., and D.E. Waliser, 2019: Tracking Atmospheric Rivers Globally: Spatial Distributions and Temporal Evolution of Life Cycle Characteristics. *J. Geophys. Res. Atmos.*, **124**, 12523 – 12552, https://doi.org/10.1029/2019JD031205.

Guirguis, K. J., and R. Avissar, 2008: A precipitation climatology and dataset intercomparison for the western United States. *J. Hydrometeor.*, **9**, 825–841.

Groisman, P. Y., R. W. Knight, T. R. Karl, D. R. Easterling, B. Sun, and J. H. Lawrimore, 2004: Contemporary Changes of the Hydrological Cycle over the Contiguous United States: Trends Derived from In Situ Observations, *Journal of Hydrometeorology*, **5**(1), 64-85.

Groisman, P. Y., R. W. Knight, D. R. Easterling, T. R. Karl, G. C. Hegerl and V. N. Razuvaev, 2005: Trends in intense precipitation in the climate record. *J. Climate*, **18**, 1326–1350.

Groisman, P. Y., R. W. Knight and T. R. Karl, 2012: Changes in intense precipitation over the central United States. *J. Hydrometeor.*, **13**, 47–66.

Hagos, S.M., L.R. Leung, J.-H. Yoon, J. Lu, and Y. Gao, 2016: A projection of changes in landfalling atmospheric river frequency and extreme precipitation over western North America from the Large Ensemble CESM simulations. *Geophys. Res. Lett.*, **43**, 1357–1363, https://doi.org/10.1002/2015GL067392.

Halverson, J.B., and T.D. Rabenhorst, 2010: Mega-snow in the Megalopolis: The Mid-Atlantic's blockbuster winter of 2009–2010. *Weatherwise*, **63**, 16–23.

Hatchett, B.J., S. Burak, J.J. Rutz, N.S. Oakley, E.H. Bair,
and M.L. Kaplan, 2017: Avalanche fatalities during atmospheric river events in the western United States. *J. Hydrometeor.*, **18**, 1359–1374, https://doi.org/10.1175/JHM-D-16-0219.1.

Hecht, C.W., and J.M. Cordeira, 2017: Characterizing the influence of atmospheric river orientation and intensity on precipitation distributions over north coastal California. *Geophys. Res. Lett.*, **44**, 9048–9058, https://doi.org/10.1002/2017GL074179.

Herold, N., A. Behrangi, and L. V. Alexander, 2017: Large uncertainties in observed daily precipitation extremes over land, *J. Geophys. Res. Atmos.*, **122**, 668–681, doi:10.1002/2016JD025842.

Higgins, R. W., Y. Yao, and X. L. Wang, 1997: Influence of the North American Monsoon System on the U.S. Summer Precipitation Regime, *Journal of Climate*, **10**(10), 2600-2622, https://doi.org/10.1175/1520-0442(1997)010<2600:IOTNAM>2.0.CO;2.

Gonzalez-Hirshfeld, I., E. A. Slinskey, P. C. Loikith, A. Goodman, D. E. Waliser, and B. Guan, 2021: Climate Model Evaluation of Atmospheric Rivers over the Continental United States, *In prep.*

Hou, A. Y., and Coauthors, 2014: The Global Precipitation Measurement mission. *Bull. Amer. Meteor. Soc.*, **95**, 701–722, https://doi.org/10.1175/BAMS-D-13-00164.1.

Howarth, M. E., C. D. Thorncroft, and L. F. Bosart, 2019: Changes in extreme precipitation in the northeast United States: 1979–2014. *Journal of Hydrometeorology*, **20**(4), 673-689.

Hu, H., F. Dominguez, Z. Wang, D. A. Lavers, G. Zhang, and F. M. Ralph, 2017: Linking Atmospheric River Hydrological Impacts on the U.S. West Coast to Rossby Wave Breaking, *Journal of Climate*, **30**(9), 3381-3399.

Hughes, M., P. J. Neiman, E. Sukovich, and F. M. Ralph, 2012: Representation of the Sierra Barrier Jet in 11 years of a high-resolution dynamical reanalysis downscaling compared with long-term wind profiler observations. *J. Geophys. Res.*, **117**, D18116, doi:10.1029/2012JD017869.

Hsu, H., and Y. Chen, 2020: Simulation and Projection of Circulations Associated with Atmospheric Rivers along the North American Northeast Coast. J. Climate, 33, 5673–5695, https://doi.org/10.1175/JCLI-D-19-0104.1.

Huffman, G.J., D.T. Bolvin, E.J. Nelkin, D.B. Wolff, R.F. Adler, G. Gu, Y. Hong, K.P. Bowman, and E.F. Stocker, 2007: The TRMM Multisatellite Precipitation Analysis (TMPA): Quasi-Global, Multiyear, Combined-Sensor Precipitation Estimates at Fine Scales. *J. Hydrometeor.*, **8**, 38–55, https://doi.org/10.1175/JHM560.1

Huffman, G. J., R. F. Adler, D. T. Bolvin, and G. Gu, 2010: The TRMM Multisatellite

Precipitation Analysis (TMPA). *Satellite Applications for Surface Hydrology*, F. Hossain and M. Gebremichael, Eds., Springer, 3-22.

Huffman, G. J., and D. T. Bolvin, 2015: TRMM and other data precipitation data set documentation. NASA TRMM Doc., 44 pp. [Available online at http://pmm.nasa.gov/sites/default/files/imce/3B42_3B43_doc_V7.pdf.]

Huffman, G. J., D. T. Bolvin, D. Braithwaite, K. Hsu, R. Joyce, C. Kidd, E. J. Nelkin, S. Sorooshian, J. Tan, and P. Xie, 2017: NASA Global Precipitation Measurement (GPM) Integrated Multi-satellitE Retrievals for GPM (IMERG). Algorithm Theoretical Basis Doc., version 4.6, NASA, 32 pp. [Available online at https://pmm.nasa.gov/sites/default/files/document_files/IMERG_ATBD_V4.6.pdf.]

Hughes, M., K.M. Mahoney, P.J. Neiman, B.J. Moore, M. Alexander, and F.M. Ralph, 2014: The Landfall and Inland Penetration of a Flood-Producing Atmospheric River in Arizona. Part II: Sensitivity of Modeled Precipitation to Terrain Height and Atmospheric River Orientation. *J. Hydrometeor.,* **15**, 1954–1974, https://doi.org/10.1175/JHM-D-13-0176.1.

Iribarne, J. V., and W. L. Godson 1981. Atmospheric Thermodynamics. D. Reidel, . p. 65.

Ivancic, T. J., and S. B. Shaw, 2016: A US-based analysis of the ability of the Clausius-Clapeyron relationship to explain changes in extreme rainfall with changing temperature. *Journal of Geophysical Research: Atmospheres*, **121**(7), 3066-3078.

Janssen, E., D. J. Wuebbles, K. E. Kunkel, S. C. Olsen, and A. Goodman, 2014: Observational- and model-based trends and projections of extreme precipitation over the contiguous United States. *Earth's Future*, **2**, 99–113, doi:10.1002/2013EF000185.

Janssen, E., R. L. Sriver, D. J. Wuebbles, and K. E. Kunkel, 2016: Seasonal and regional variations in extreme precipitation event frequency using CMIP5. *Geophysical Research Letters*, **43**, 5385–5393, doi:10.1002/2016GL069151.

Jones, P. W., 1999: First- and second-order conservative remapping schemes for grids in spherical coordinates. *Mon. Wea. Rev.*, **127**, 2204–2210.

Kalognomou, E., C. Lennard, M. Shongwe, I. Pinto, A. Favre, M. Kent, B. Hewitson, A. Dosio, G. Nikulin, H. Panitz, and M. Büchner, 2013: A Diagnostic Evaluation of Precipitation in CORDEX Models over Southern Africa. *J. Climate*, **26**, 9477–9506, https://doi.org/10.1175/JCLI-D-12-00703.1

Karl, T. R., and R. W. Knight, 1998: Secular Trends of Precipitation Amount, Frequency, and Intensity in the United States, *Bulletin of the American Meteorological Society*, **79**(2), 231-242.

Kharin, V. V., F. W. Zwiers, X. Zhang, and M. Wehner, 2013: Changes in temperature and precipitation extremes in the CMIP5 ensemble. *Climatic Change*, **119**, 345–357, https://doi.org/10.1007/s10584-013-0705-8.

Khouakhi, A., and G. Villarini, 2016: On the relationship between atmospheric rivers and high sea water levels along the U.S. West Coast. *Geophys. Res. Lett.*, **43**, 8815–8822, https://doi.org/10.1002/2016GL070086.

Kidd, C., A. Becker, G.J. Huffman, C.L. Muller, P. Joe, G. Skofronick-Jackson, and D.B. Kirschbaum, 2017: So, How Much of the Earth's Surface Is Covered by Rain Gauges? *Bull. Amer. Meteor. Soc.*, **98**, 69–78, https://doi.org/10.1175/BAMS-D-14-00283.1

Kim, J., B. Guan, D.E. Waliser, R.D. Ferraro, J. L. Case, T. Iguchi, E. Kemp, W. Putman, W. Wang, D. Wu, & B. Tian, 2018: Winter precipitation characteristics in western US related to atmospheric river landfalls: Observations and model evaluations. *Climate Dynamics*, **50**(1-2), 231– 248, https://doi.org/10.1007/s00382-017-3601-5.

Knight, D. B., and R. E. Davis, 2009: Contribution of tropical cyclones to extreme rainfall events in the southeastern United States. *J. Geophys. Res.*, **114**, D23102, doi:10.1029/2009JD012511.

Knutson, T. R., J. L. McBride, J. Chan, K. Emanuel, G. Holland, C. Landsea, I. Held, J. P. Kossin, A. K. Srivastava, and M. Sugi, 2010: Tropical cyclones and climate change. *Nature Geoscience*, **3**, 157-163, http://dx.doi.org/10.1038/ngeo779.

Knippertz, P. and H. Wernli, 2010: A Lagrangian Climatology of Tropical Moisture Exports to the Northern Hemispheric Extratropics. *J. Climate*, **23**, 987–1003, https://doi.org/10.1175/2009JCLI3333.1.

Konrad, C.P., and M.D. Dettinger, 2017: Flood runoff in relation to water vapor transport by atmospheric rivers over the western United States, 1949–2015. *Geophys. Res. Lett.*, **44**, 11 456–11 462, https://doi.org/10.1002/2017GL075399.

Kossin, J.P., T. Hall, T. Knutson, K.E. Kunkel, R.J. Trapp, D.E. Waliser, and M.F. Wehner, 2017: Extreme storms. *Climate Science Special Report: Fourth National Climate Assessment*, D. J. Wuebbles, D.W. Fahey, K.A. Hibbard, D.J. Dokken, B.C.

Stewart, and T.K. Maycock, Eds., Vol. I, U.S. Global Change Research Program, 257-276, 10.7930/J07S7KXX.

Kummerow, C. D., S. Ringerud, J. Crook, D. Randel, and W. Berg, 2011: An observationally generated a priori database for microwave rainfall retrievals, *J. Atmos. Oceanic Technol.*, **28**, 113–130, doi:10.1175/2010JTECHA1468.1.

Kunkel, K. E., D. R. Easterling, K. Redmond and K. Hubbard, 2003: Temporal variations of extreme precipitation events in the United States: 1895–2000. *Geophys. Res. Lett.*, **30**, 1900, doi:10.1029/2003GL018052.

Kunkel, K. E., T. R. Karl and D. R. Easterling, 2007: A Monte Carlo assessment of uncertainties in heavy precipitation frequency variations. *J. Hydrometeor.*, **8**, 1152–1160.

Kunkel, K. E., D. R. Easterling, D. A. R. Kristovich, B. Gleason, L. Stoecker, and R. Smith, 2010: Recent increases in U.S. heavy precipitation associated with tropical cyclones. *Geophys. Res. Lett.*, **37**, L24706, http://dx.doi.org/10.1029/2010GL045164.

Kunkel, K.E., D.R. Easterling, D.A. Kristovich, B. Gleason, L. Stoecker, and R. Smith, 2012: Meteorological Causes of the Secular Variations in Observed Extreme Precipitation Events for the Conterminous United States. *J. Hydrometeor.*, **13**, 1131–1141, https://doi.org/10.1175/JHM-D-11-0108.1.

Kunkel, K. E., and Coauthors, 2013a: Monitoring and Understanding Trends in Extreme Storms: State of Knowledge. *Bull. Amer. Meteor. Soc.*, **94**, 499–514, https://doi.org/10.1175/BAMS-D-11-00262.1.

Kunkel, K. E., T. R. Karl, D. R. Easterling, K. Redmond, J. Young, X. Yin, and P. Hennon, 2013b: Probable maximum precipitation and climate change. *Geophysical Research Letters*, **40**, 1402–1408, doi:10.1002/grl.50334.

Lackmann, G.M., and J.R. Gyakum, 1999: Heavy cold-season precipitation in the northwestern United States: Synoptic climatology and an analysis of the flood of 17–18 January 1986. *Wea. Forecasting*, **14,** 687–700.

Lackmann, G.M., 2013: The South-Central U.S. Flood of May 2010: Present and Future. *J. Climate*, **26**, 4688–4709, https://doi.org/10.1175/JCLI-D-12-00392.1.

Lamjiri, M. A., Dettinger, M. D., Ralph, F. M., and B. Guan, 2017: Hourly storm characteristics along the US West Coast: Role of atmospheric rivers in extreme precipitation. *Geophys. Res. Lett.*, **44**, 7020-7028, doi:10.1002/2017GL074193.

Lavers, D. A., R. P. Allen, E. F. Wood, G. Villarini, D. J. Brayshaw, and A. J. Wade, 2011: Winter floods in Britain are connected to atmospheric rivers. *Geophys. Res. Lett.*, **38**, L23803, doi:10.1029/2011GL049783.

Lavers, D.A. and G. Villarini, 2013: Atmospheric Rivers and Flooding over the Central United States. *J. Climate,* **26**, 7829–7836, https://doi.org/10.1175/JCLI-D-13-00212.1.

Lavers, D.A., R.P. Allan, G. Villarini, B. Lloyd-Hughes, D.J. Brayshaw, and A.J. Wade, 2013: Future changes in atmospheric rivers and their implications for winter flooding in Britain, Environ. Res. Lett., 8, 034010, doi:10.1088/1748-9326/8/3/034010.

Lavers, D.A., and G. Villarini, 2015: The contribution of atmospheric rivers to precipitation in Europe and the United States. *J. Hydrol.*, **522**, 382–390, https://doi.org/10.1016/j.jhydrol.2014.12.010.

Lepore, C., D. Veneziano, and A. Molini, 2014: Temperature and CAPE dependence of rainfall extremes in the eastern United States, *Geophys. Res. Lett.*, **42**, 74–83, doi:10.1002/2014GL062247.

Letkewicz, C.E. and M.D. Parker, 2010: Forecasting the Maintenance of Mesoscale Convective Systems Crossing the Appalachian Mountains. *Wea. Forecasting,* **25**, 1179–1195, https://doi.org/10.1175/2010WAF2222379.1.

Lin, Y., K. E. Mitchell, E. Rogers, M. E. Baldwin, and G. I. DiMego, 1999: Test assimilations of the real-time, multi-sensor hourly precipitation analysis into the NCEP Eta model. Preprints, *Eighth Conf. on Mesoscale Meteorology,* Boulder, CO, Amer. Meteor. Soc., 341–344.

Liu, Z., D. Ostrenga, W. Teng, and S. Kempler, 2012: Tropical Rainfall Measuring Mission (TRMM) Precipitation Data and Services for Research and Applications. *Bull. Amer. Meteor. Soc.*, **93**, 1317-1325

Liu, Z., 2016: Comparison of Integrated Multisatellite Retrievals for GPM (IMERG) and TRMM Multisatellite Precipitation Analysis (TMPA) monthly precipitation products: Initial results. *J. Hydrometeor.*, **17**, 777–790, doi:10.1175/ JHM-D-15-0068.1.

Lora, J. M., J.L. Mitchell, C. Risi, and A.E. Tripati, 2017: North Pacific atmospheric rivers and their influence on western North America at the Last Glacial Maximum. *Geophys. Res. Lett.*, **44**, 1051–1059, https://doi.org/10.1002/2016GL071541.

Lu, J.; D. Xue, Y. Gao, G. Chen, L. R. Leung, P. Staten, 2018: Enhanced hydrological extremes in the western United States under global warming through the lens of water vapor wave activity. *NPJ Clim. Atmos. Sci.*, **1**, 1–9.

Mahoney, K., D. L. Jackson, P. Neiman, M. Hughes, L. Darby, G. Wick, A. White, E. Sukovich, and R. Cifelli, 2016: Understanding the Role of Atmospheric Rivers in Heavy Precipitation in the Southeast United States. *Mon. Wea. Rev.*, **144**, 1617–1632, https://doi.org/10.1175/MWR-D-15-0279.1.

Mahoney, K., and Coauthors, 2018: An examination of an inland penetrating atmospheric river flood event under potential future thermodynamic conditions. *J. Clim.*, **31**, 6281–6297.

Menne, M. J., I. Durre, B. G. Gleason, T. G. Houston, and R. S. Vose, 2012: An overview of the Global Historical Climatology Network-Daily database. *J. Atmos. Oceanic Technol.*, **29**, 897–910.

Mesinger, F., G. DiMego, E. Kalnay, K. Mitchell, P. C. Shafran, W. Ebisuzaki, D. Jović, J. Woollen, E. Rogers, E. H. Berbery, M. B. Ek, Y. Fan, R. Grumbine, W. Higgins, H. Li, Y. Lin, G. Manikin, D. Parrish, and W. Shi, 2006: North American Regional Reanalysis. *Bull. Amer. Meteor. Soc.*, **87**, 343–360, https://doi.org/10.1175/BAMS-87-3-343.

Mestas-Nuñez, A.M., D.B. Enfield, and C. Zhang, 2007: Water Vapor Fluxes over the Intra-Americas Sea: Seasonal and Interannual Variability and Associations with Rainfall. *J. Climate*, **20**, 1910–1922, https://doi.org/10.1175/JCLI4096.1.

Miller, D.K., D. Hotz, J. Winton, and L. Stewart, 2018: Investigation of Atmospheric Rivers Impacting the Pigeon River Basin of the Southern Appalachian Mountains. *Wea. Forecasting*, **33**, 283–299, https://doi.org/10.1175/WAF-D-17-0060.1.

Min, S.-K., X. Zhang, F. W. Zwiers, and G. C. Hegerl, 2011: Human contribution to more-intense precipitation extremes, *Nature*, **470**, 378–381.

Mishra, V., J. M. Wallace, and D. P. Lettenmaier, 2012: Relationship between hourly extreme precipitation and local air temperature in the United States, *Geophys. Res. Lett.*, **39**, L16403, doi:10.1029/2012GL052790.

Molod, A., L. Takacs, M. Suárez, and J. Bacmeister, 2015: Development of the GEOS-5 atmospheric general circulation model: Evolution from MERRA to MERRA2. *Geosci. Model Dev.*, **8**, 1339–1356, https://doi.org/10.5194/gmd-8-1339-2015.

Moore, B.J., P.J. Neiman, F.M. Ralph, and F.E. Barthold, 2012: Physical Processes Associated with Heavy Flooding Rainfall in Nashville, Tennessee, and Vicinity during 1–2 May 2010: The Role of an Atmospheric River and Mesoscale Convective Systems. *Mon. Wea. Rev.,* **140**, 358–378, https://doi.org/10.1175/MWR-D-11-00126.1.

Morrison, A. G. Villarini, W. Zhang, E. Scoccimarro, 2019: Projected changes in extreme precipitation at sub-daily and daily time scales. *Glob. Planet. Change*, **182**, 103004.

Mueller, M.J., K.M. Mahoney, and M. Hughes, 2017: High-Resolution Model-Based Investigation of Moisture Transport into the Pacific Northwest during a Strong Atmospheric River Event. *Mon. Wea. Rev.*, **145**, 3861–3879, https://doi.org/10.1175/MWR-D-16-0466.1.

Mundhenk, B.D., E.A. Barnes, E.D. Maloney, and C.F. Baggett, 2018: Skillful empirical subseasonal prediction of landfalling atmospheric river activity using the Madden-Julian oscillation and quasi-biennial oscillation. *npj Climate Atmos. Sci.*, **1**, 20177, https://doi.org/10.1038/s41612-017-0008-2.

Nayak, S., K. Dairaku, I. Takayabu, A. Suzuki-Parker, N. N. Ishizaki, 2018: Extreme precipitation linked to temperature over Japan: Current evaluation and projected changes with multi-model ensemble downscaling. *Clim. Dyn.*, **51**, 4385–4401.

Nakamura, J., U. Lall, Y. Kushnir, A.W. Robertson, and R. Seager, 2013: Dynamical Structure of Extreme Floods in the U.S. Midwest and the United Kingdom. *J. Hydrometeor.*, **14**, 485–504, https://doi.org/10.1175/JHM-D-12-059.1.

Neiman, P., F. M. Ralph, G. A. Wick, J. D. Lundquist, and M. D. Dettinger, 2008a: Meteorological Characteristics and Overland Precipitation Impacts of Atmospheric Rivers Affecting the West Coast of North America Based on Eight Years of SSM/I Satellite Observations. *J. Hydrometeor.*, **9**, 22-47.

Neiman, P., F. M. Ralph, G. A. Wick, Y. H. Kuo, T. K. Wee, and Z. Ma, 2008b: Diagnosis of an Intense Atmospheric River Impacting the Pacific Northwest: Storm Summary and Offshore Vertical Structure Observed with COSMIC Satellite Retrievals. *Mon. Wea. Rev.*, **136**, 4398- 4420.

Neiman, P.J., L.J. Schick, F.M. Ralph, M. Hughes, and G.A. Wick, 2011: Flooding in Western Washington: The Connection to Atmospheric Rivers. *J. Hydrometeor.*, **12**, 1337–1358, https://doi.org/10.1175/2011JHM1358.1.

Neiman, P.J., F.M. Ralph, B.J. Moore, M. Hughes, K.M. Mahoney, J.M. Cordeira, and M.D. Dettinger, 2013: The Landfall and Inland Penetration of a Flood-Producing

Atmospheric River in Arizona. Part I: Observed Synoptic-Scale, Orographic, and Hydrometeorological Characteristics. *J. Hydrometeor.*, **14**, 460–484, https://doi.org/10.1175/JHM-D-12-0101.1.

Newell, R. E., N. E. Newell, Y. Zhu, and C. Scott, 1992: Tropospheric rivers?–A pilot study. *Geophysical research letters*, **19**(24), 2401-2404.

Newman, M., G. N. Kiladis, K. M. Weickmann, F. M. Ralph, and P. D. Sardeshmukh, 2012: Relative contributions of synoptic and low- frequency eddies to time- mean atmospheric moisture transport, including the role of atmospheric rivers. *J. Clim.*, **25**, 7341–7361.

Nikulin, G., C. Jones, F. Giorgi, G. Asrar, M. Büchner, R. Cerezo-Mota, O. B. Christensen, M. Déqué, J. Fernandez, A. Hänsler, E. van Meijgaard, P. Samuelsson, M. B. Sylla, and L.
Norris, J., A. Hall, D. Chen, C. W. Thackeray, and G. D. Madakumbura, 2021: Assessing the Representation of Synoptic Variability Associated with California Extreme Precipitation in CMIP6 Models. *Journal of Geophysical Research: Atmospheres*, **126**(6), e2020JD033938.

Sushama, 2012: Precipitation Climatology in an Ensemble of CORDEX-Africa Regional Climate Simulations. *J. Climate*, **25**, 6057–6078, https://doi.org/10.1175/JCLI-D-11-00375.1.

Oakley, N.S., J.T. Lancaster, M.L. Kaplan, and F.M. Ralph, 2017: Synoptic conditions associated with cool season post-fire debris flows in the Transverse Ranges of southern California. *Nat. Hazards*, **88**, 327–354, https://doi.org/10.1007/s11069-017-2867-6.

O'Gorman, P. A., and T. Schneider, 2009: The physical basis for increases in precipitation extremes in simulations of 21st-century climate change. *Proc. Natl. Acad. Sci.*, **106**, 14773–14777.

Oh, S.G. and L. Sushama, 2020: Short-duration precipitation extremes over Canada in a warmer climate. *Clim. Dyn.*, **54**, 2493–2509.

O'Neill, B. C., and Coauthors, 2016: The Scenario Model Intercomparison Project (ScenarioMIP) for CMIP6. *Geoscientific Model Development*, **9**(9), 3461–3482. https://doi.org/10.5194/gmd-9-3461-2016.

Pall, P., M. R. Allen, and D. A. Stone, 2007: Testing the Clausius-Clapeyron constraint on changes in extreme precipitation under CO_2 warming. *Climate Dyn.*, **28**, 351–363, doi:10.1007/s00382-006-0180-2.

Pall, P., C. M. Patricola, M. F. Wehner, D. A. Stone, C. J. Paciorek, and W. D. Collins, 2017: Diagnosing conditional anthropogenic contributions to heavy Colorado rainfall in September 2013. *Weather and Climate Extremes*, **17**, 1-6, http://dx.doi.org/10.1016/j.wace.2017.03.004.

Paltan, H., D. Waliser, W.H. Lim, B. Guan, D. Yamazaki, R. Pant, and S. Dadson, 2017: Global floods and water availability driven by atmospheric rivers. *Geophys. Res. Lett.*, **44**, 10 387–10 395, https://doi.org/10.1002/2017GL074882.

Payne, A.E., and G. Magnusdottir, 2015: An evaluation of atmospheric rivers over the North Pacific in CMIP5 and their response to warming under RCP 8.5. *J. Geophys. Res. Atmos.*, **120**, 11 173–11 190, https://doi.org/10.1002/2015JD023586.

Payne, A. E., and Coauthors, 2020: Responses and impacts of atmospheric rivers to climate change. *Nature Reviews Earth & Environment*, **1**(3), 143-157.

Pendergrass, A. G., 2018: What precipitation is extreme? *Science*, **360**, 1072.

Pfahl, S., and H. Wernli, 2012: Quantifying the relevance of cyclones for precipitation extremes. *Journal of Climate*, **25**(19), 6770-6780.

Pfahl, S., E. Madonna, M. Boettcher, H. Joos, and H. Wernli, 2014: Warm Conveyor Belts in the ERA-Interim Dataset (1979–2010). Part II: Moisture Origin and Relevance for Precipitation. *J. Climate*, **27**, 27–40, https://doi.org/10.1175/JCLI-D-13-00223.1.

Pierce, D. W., and Coauthors, 2013: The key role of heavy precipitation events in climate model disagreements of future annual precipitation changes in California. *Journal of Climate*, **26**(16), 5879– 5896. https://doi.org/10.1175/JCLI-D-12-00766.1

Prat, O., and B. Nelson, 2013: Precipitation contribution of tropical cyclones in the southeastern United States from 1998 to 2009 using TRMM satellite data. *J. Climate*, **26**, 1047–1062.

Rabinowitz, J.L., A.R. Lupo, and P.E. Guinan, 2018: Evaluating linkages between atmospheric blocking patterns and heavy rainfall events across the north-central Mississippi River valley for different ENSO phases. *Advances in Meteorology*, **2018**, https://doi.org/10.1155/2018/1217830.

Rabinowitz, J. L., A. R. Lupo, P. S. Market, and P. E. Guinan, 2019: An investigation of atmospheric rivers impacting heavy rainfall events in the North-Central Mississippi River Valley. *International Journal of Climatology*, **39**(10), 4091-4106.

Radić, V., A. J. Cannon, B. Menounos, and N. Gi, 2015: Future changes in autumn atmospheric river events in British Columbia, Canada, as projected by CMIP5 global climate models. *Journal of Geophysical Research: Atmospheres*, **120**, 9279–9302, https://doi.org/10.1002/2015JD023279.

Ralph, F.M., P.J. Neiman, D.E. Kingsmill, P.O. Persson, A.B. White, E.T. Strem, E.D. Andrews, and R.C. Antweiler, 2003: The Impact of a Prominent Rain Shadow on Flooding in California's Santa Cruz Mountains: A CALJET Case Study and Sensitivity to the ENSO Cycle. *J. Hydrometeor.*, **4**, 1243–1264, https://doi.org/10.1175/1525-7541(2003)004<1243:TIOAPR>2.0.CO;2.

Ralph, F.M., P.J. Neiman, and G.A. Wick, 2004: Satellite and CALJET Aircraft Observations of Atmospheric Rivers over the Eastern North Pacific Ocean during the Winter of 1997/98. *Mon. Wea. Rev.*, **132**, 1721–1745, https://doi.org/10.1175/1520-0493(2004)132<1721:SACAOO>2.0.CO;2.

Ralph, F.M., P.J. Neiman, and R. Rotunno, 2005: Dropsonde Observations in Low-Level Jets over the Northeastern Pacific Ocean from CALJET-1998 and PACJET-2001: Mean Vertical-Profile and Atmospheric-River Characteristics. *Mon. Wea. Rev.*, **133**, 889–910, https://doi.org/10.1175/MWR2896.1.

Ralph, F.M., P.J. Neiman, G. Wick, S. Gutman, M. Dettinger, D. Cayan, and A.B. White, 2006: Flooding on California's Russian River: Role of atmospheric rivers. *Geophys. Res. Lett.*, **33,** L13801, doi:10.1029/2006GL026689.

Ralph, F. M., and M. D. Dettinger, 2011: Storms, Floods, and the Science of Atmospheric Rivers. *EOS*, **92**, 265-266.

Ralph, F. M., and M. D. Dettinger, 2012: Historical and national perspectives on extreme West Coast precipitation associated with atmospheric rivers during December 2010. *Bull. Amer. Meteor. Soc.*, **93**, 783–790.

Ralph, F. M., T. Coleman, P. J. Neiman, R. J. Zamora, and M. D. Dettinger, 2013: Observed impacts of duration and seasonality of atmospheric-river landfalls on soil moisture and runoff in coastal northern California, *J. Hydrometeorol.*, **14**, 443–459, doi:10.1175/JHM-D-12-076.1.

Ralph, F. M., M. D. Dettinger, J. J. Rutz, D. E. Waliser, 2020: *Atmospheric Rivers*. Springer, 252 pp.

Ramos, A. M., R. Tomé, R. M. Trigo, M. L. Liberato, and J. G. Pinto, 2016: Projected changes in atmospheric rivers affecting Europe in CMIP5 models. *Geophys. Res. Lett*, **43**, 9315-9323.

Reichle, R. H., C. S. Draper, Q. Liu, M. Girotto, S. P. P. Mahanama, R. D. Koster, and G. J. M. De Lannoy, 2017: Assessment of MERRA-2 land surface hydrology estimates. *J. Climate*, **30**, 2937–2960, https://doi.org/10.1175/JCLI-D-16-0720.1.

Rienecker, M. M. and Coauthors, 2011: MERRA: NASA's Modern-Era Retrospective Analysis for Research and Applications. *J. Climate*, **24**, 3624–3648, https://doi.org/10.1175/JCLI-D-11-00015.1.

Risser, M. D., and M. F. Wehner, 2017: Attributable Human-Induced Changes in the Likelihood and Magnitude of the Observed Extreme Precipitation during Hurricane Harvey. *Geophys. Res. Lett.*, **44**, 12457-12464.

Rivera, E.R., F. Dominguez, and C.L. Castro, 2014: Atmospheric Rivers and Cool Season Extreme Precipitation Events in the Verde River Basin of Arizona. J. Hydrometeor., 15, 813–829, https://doi.org/10.1175/JHM-D-12-0189.1.

Rupp, D. E., and S. Li, 2017: Less warming projected during heavy winter precipitation in the Cascades and Sierra Nevada. *International Journal of Climatology*, **37**(10), 3984-3990.

Rutz, J.J., and W.J. Steenburgh, 2012: Quantifying the role of atmospheric rivers in the interior western United States. *Atmos. Sci. Lett.*, **13**, 257–261, doi:10.1002/asl.392.

Rutz, J.J., W.J. Steenburgh, and F.M. Ralph, 2014: Climatological Characteristics of Atmospheric Rivers and Their Inland Penetration over the Western United States. *Mon. Wea. Rev.*, **142**, 905–921, https://doi.org/10.1175/MWR-D-13-00168.1.

Rutz, J. J., W. J . Steenburgh, W. J., and F. M. Ralph, 2015: The inland penetration of atmospheric rivers over western North America: A Lagrangian analysis. *Monthly Weather Review*, **143**(5), 1924-1944.

Rutz, J. J., and Coauthors, 2019: The atmospheric river tracking method intercomparison project (ARTMIP): quantifying uncertainties in atmospheric river climatology. *J. Geophys. Res. Atmos.*, **124**, 13777-13802, https://doi.org/10.1029/2019JD030936.

Sapiano, M. R., and P. A. Arkin, 2009: An intercomparison and validation of high-resolution satellite precipitation estimates with 3-hourly gauge data. *J. Hydrometeor.*, **10**, 149–166, https://doi.org/10.1175/2008JHM1052.1.

Shaw, S. B., A. A. Royem, and S. J. Riha, 2011: The relationship between extreme hourly precipitation and surface temperature in different hydroclimatic regions of the United States, *J. Hydrometeorol.*, **12**, 319–325, doi:10.1175/2011jhm1364.1.

Sherwood, S.C., W. Ingram, Y. Tsushima, M. Satoh, M. Roberts, P. L. Vidale, P. A. O'Gorman, 2010: Relative humidity changes in a warmer climate. *J. Geophys. Res. Atmos.*, **115**, D09104.

Shi, X. and D. Durran, 2016: Sensitivities of extreme precipitation to global warming are lower over mountains than over oceans and plains. *J. Clim*, **29**, 4779–4791.

Shields, C.A., and J.T. Kiehl, 2016a: Atmospheric river landfall-latitude changes in future climate simulations. *Geophys. Res. Lett.*, **43**, 8775–8782, https://doi.org/10.1002/2016GL070470.

Shields, C. A., and J. T. Kiehl, 2016b: Simulating the pineapple express in the half degree Community Climate System Model, CCSM4. *Geophysical Research Letters*, **43**, 7767– 7773. https://doi.org/10.1002/2016GL069476

Shields, C. A., J. T. Kiehl, and G. A. Meehl, 2016: Future changes in regional precipitation
simulated by a half-degree coupled climate model: Sensitivity to horizontal resolution. *J. Advances in Modeling Earth Systems*, **8**, 863-884.

Shields, C.A., and Coauthors, 2018: Atmospheric River Tracking Method Intercomparison Project (ARTMIP): Project goals and experimental design. *Geosci. Model Dev.*, **11**, 2455–2474, https://doi.org/10.5194/gmd-11-2455-2018.

Siler, N., and G. Roe, 2014: How will orographic precipitation respond to surface warming? An idealized thermodynamic perspective. *Geophys. Res. Lett.*, **41**, 2606–2613.

Singh, I., F. Dominguez, E. Demaria, and J. Walter, 2018: Extreme landfalling atmospheric river events in Arizona: Possible future changes. *J. Geophys. Res. Atmos.*, **123**, 7076–7097.

Smith, J.A.S., M.L. Baeck, A.A. Ntelekos, G. Villarini, and M. Steiner, 2011: Extreme rainfall and flooding from orographic thunderstorms in the central Appalachians. *Water Resour. Res.*, **47**, W04514, https://doi.org/10.1029/2010WR010190.

Smith, J.A., M.L. Baeck, G. Villarini, D.B. Wright, and W. Krajewski, 2013: Extreme Flood Response: The June 2008 Flooding in Iowa. *J. Hydrometeor.*, **14**, 1810–1825, https://doi.org/10.1175/JHM-D-12-0191.1.

Sousa, P.M., A. M. Ramos, C. C. Raible, M. Messmer, R. Tomé, J. G. Pinto, R. M. Trigo, 2020: North Atlantic Integrated Water Vapor Transport—From 850 to 2100 CE: Impacts on Western European Rainfall. *J. Clim.*, **33**, 263–279.

Tabari, H., P. Hosseinzadehtalaei, A. AghaKouchak, and P. Willems, 2019: Latitudinal heterogeneity and hotspots of uncertainty in projected extreme precipitation. *Environmental Research Letters*, **14**(12), 124032.

Tan, J., W. A. Petersen, and A. Tokay, 2016: A novel approach to identify sources of errors in IMERG for GPM ground validation. *J. Hydrometeor.*, **17**, 2477–2491, https://doi.org/10.1175/JHM-D-16-0079.1.

Tang, Y., J. Winkler, S. Zhong, X. Bian, D. Doubler, L. Yu, and C. Walters, 2017: Future changes in the climatology of the Great Plains low-level jet derived from fine resolution multi-model simulations. *Scientific reports*, **7**(1), 1-10.

Taylor, K. E., 2001: Summarizing multiple aspects of model performance in a single diagram, *J. Geophys. Res.*, **106**, 7183–7192, http://dx.doi.org/10.1029/2000JD900719.

Teale, N., and D. A. Robinson, 2020: Patterns of water vapor transport in the Eastern United States. *Journal of Hydrometeorology*, **21**(9), 2123-2138.

Trenberth, K. E., A. Dai, R. M. Rasmussen, and D. B. Parsons, 2003: The changing character of precipitation. *Bull. Amer. Meteor. Soc.*, **84**, 1205–1217.

U.S. Environmental Protection Agency (EPA), 2016: Climate change indicators in the United States, 2016. Fourth edition. EPA 430-R-16-004. www.epa.gov/climate-indicators.

USGCRP, 2017: *Climate Science Special Report: Fourth National Climate Assessment, Volume I*, D. J. Wuebbles, D.W. Fahey, K.A. Hibbard, D.J. Dokken, B.C. Stewart, and T.K. Maycock, Eds., U.S. Global Change Research Program, Washington, DC, USA, 470 pp, 10.7930/J0J964J6.

Viale, M., and M. N. Nuñez, 2011: Climatology of winter orographic precipitation over the subtropical central Andes and associated synoptic and regional characteristics. *J. Hydrometeor.*, **12**, 481–507.

Villarini, G., J.A. Smith, M.L. Baeck, and W.F. Krajewski, 2011a: Examining flood frequency distributions in the Midwest U.S. *J. Amer. Water Resour. Assoc.*, **47**, 447–463.

Villarini, G., J.A. Smith, M.L. Baeck, R. Vitolo, D.B. Stephenson, and W. Krajewski, 2011b: On the frequency of heavy rainfall for the Midwest of the United States. *J. Hydrol.*, **400**, 103–120.

Waliser, D.E., and B. Guan, 2017: Extreme winds and precipitation during landfall of atmospheric rivers. *Nat. Geosci.*, **10**, 179–183, https://doi.org/10.1038/ngeo2894.

Waliser, D.E., and J.M. Cordeira, 2020: Chapter 6: AR Modeling: Forecasts, Climate Simulations, and Climate Projections. *Atmospheric Rivers*, F. M. Ralph, M. D. Dettinger, J. J. Rutz and D. E. Waliser, Eds., Springer, 189-213.

Wang, S.-Y. S., L. Zhao, and R. R. Gillies, 2016: Synoptic and quantitative attributions of the extreme precipitation leading to the August 2016 Louisiana flood, *Geophys. Res. Lett.*, **43**, 805-814, doi:10.1002/2016GL071460.

Warner, M.D., C.F. Mass, and E.P. Salathé, 2012: Wintertime Extreme Precipitation Events along the Pacific Northwest Coast: Climatology and Synoptic Evolution. *Mon. Wea. Rev.*, **140**, 2021–2043, https://doi.org/10.1175/MWR-D-11-00197.1.

Warner, M.D., C.F. Mass, and E.P. Salathé, 2015: Changes in Winter Atmospheric Rivers along the North American West Coast in CMIP5 Climate Models. *J. Hydrometeor.*, **16**, 118–128, https://doi.org/10.1175/JHM-D-14-0080.1.

Wehner, M. F., 2013: Very extreme seasonal precipitation in the NARCCAP ensemble: Model performance and projections. *Climate Dynamics*, **40**, 59–80, doi:10.1007/s00382-012-1393-1.

Wick, G. A., P. J. Neiman, F. M. Ralph, and T. M. Hamill, 2013: Evaluation of forecasts of the water vapor signature of atmospheric rivers in operational numerical weather prediction models. *Weather and Forecasting*, **28**(6), 1337-1352.

Young, A.M., K.T. Skelly, and J.M. Cordeira, 2017: High-impact hydrologic events and atmospheric rivers in California: An investigation using the NCEI Storm Events Database. *Geophys. Res. Lett.*, **44**, 3393–3401, https://doi.org/10.1002/2017GL073077.

Zhang, X. , L. Alexander, G. C. Hegerl, P. Jones , A. K. Tank, T. C. Peterson, B. Trewin, and F. W. Zwiers, 2011: Indices for monitoring changes in extremes based on daily temperature and precipitation data. *WIREs Climate Change*, **2**, 851-870, doi:10.1002/wcc.147.

Zhang, W., and Villarini, G., 2018: Uncovering the role of the East Asian jet stream and heterogeneities in atmospheric rivers affecting the western United States. *Proceedings of the National Academy of Sciences*, **115**(5), 891-896.

Zhou, Y., K. Nelson, K. I. Mohr, G. J. Huffman, R. Levy, and M. Grecu, 2019: A spatial-temporal extreme precipitation database from GPM IMERG. *Journal of Geophysical Research: Atmospheres*, **124**(19), 10344-10363, https://doi.org/10.1029/2019JD030449.

Zhu, Y., and R.E. Newell, 1994: Atmospheric rivers and bombs. *Geophys. Res. Lett.*,**21,** 1999–2002.

Zhu, Y. and R.E. Newell, 1998: A Proposed Algorithm for Moisture Fluxes from Atmospheric Rivers. *Mon. Wea. Rev.*, **126**, 725–735, https://doi.org/10.1175/1520-0493(1998)126<0725:APAFMF>2.0.CO;2.

Appendix A: Supplementary Material for Chapter 2

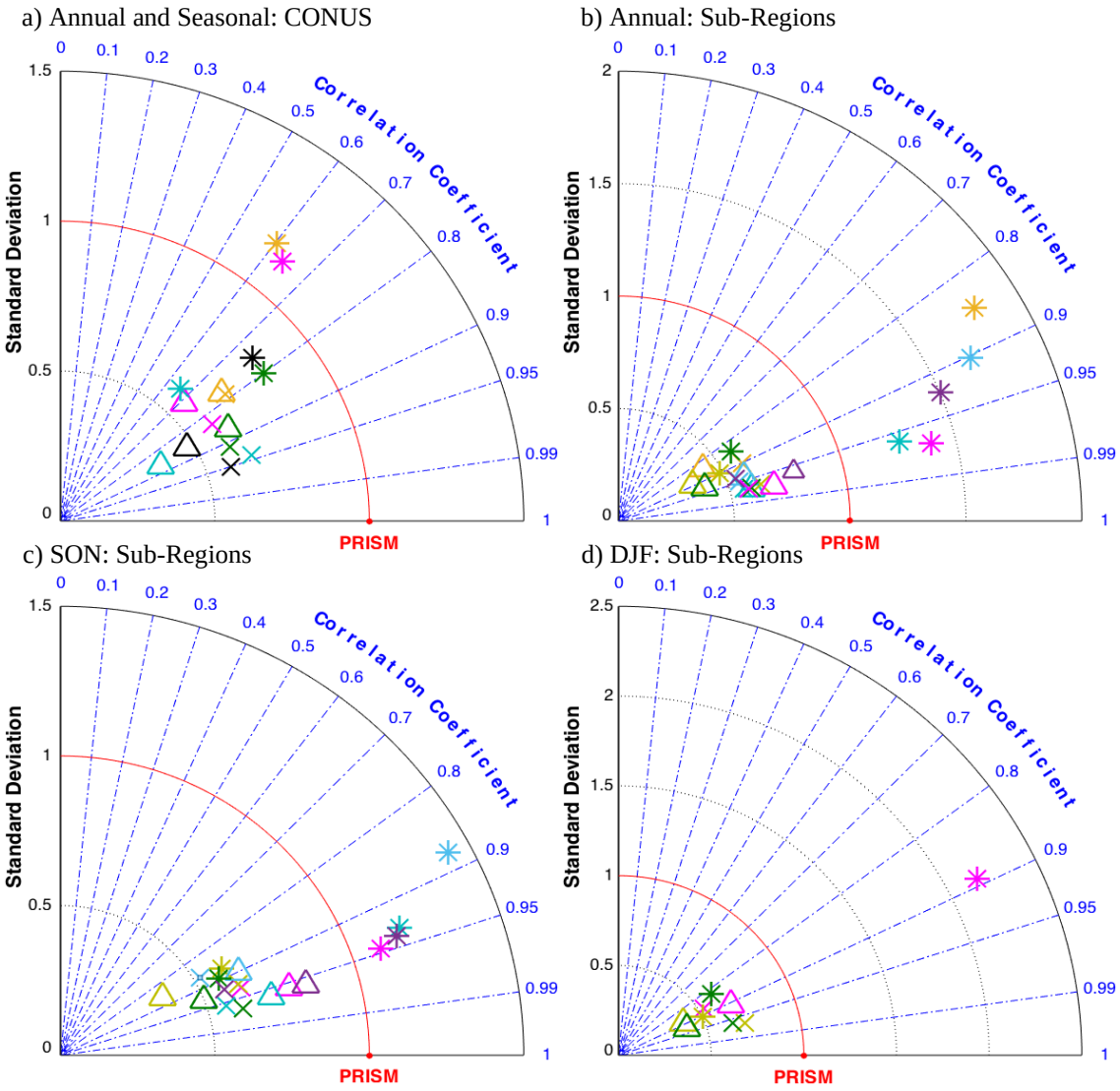

Figure S1.1 Taylor diagrams quantifying the spatial correspondence of the mean frequency of P-Cat occurrence patterns for TMPA, MERRA-2, and NARR relative to PRISM. Results are for (a) the CONUS annually and seasonally, (b) relevant NCA sub-regions annually, (c) September, October, November for the NCA sub-regions, and (d) December, January, February for the NCA sub-regions. Each dataset is labeled by a

symbol with each season and sub-region assigned a color as defined in the legends in the top two panels. The x and y axes correspond to the standard deviation ratio between the indicated dataset and PRISM. The radial axis is the pattern correlation, and the distance between the symbol and the PRISM location is proportional to the centered root mean squared difference between the spatial field of the maximum P-Cats of the indicated dataset and PRISM, normalized by the spatial standard deviation of the PRISM field.

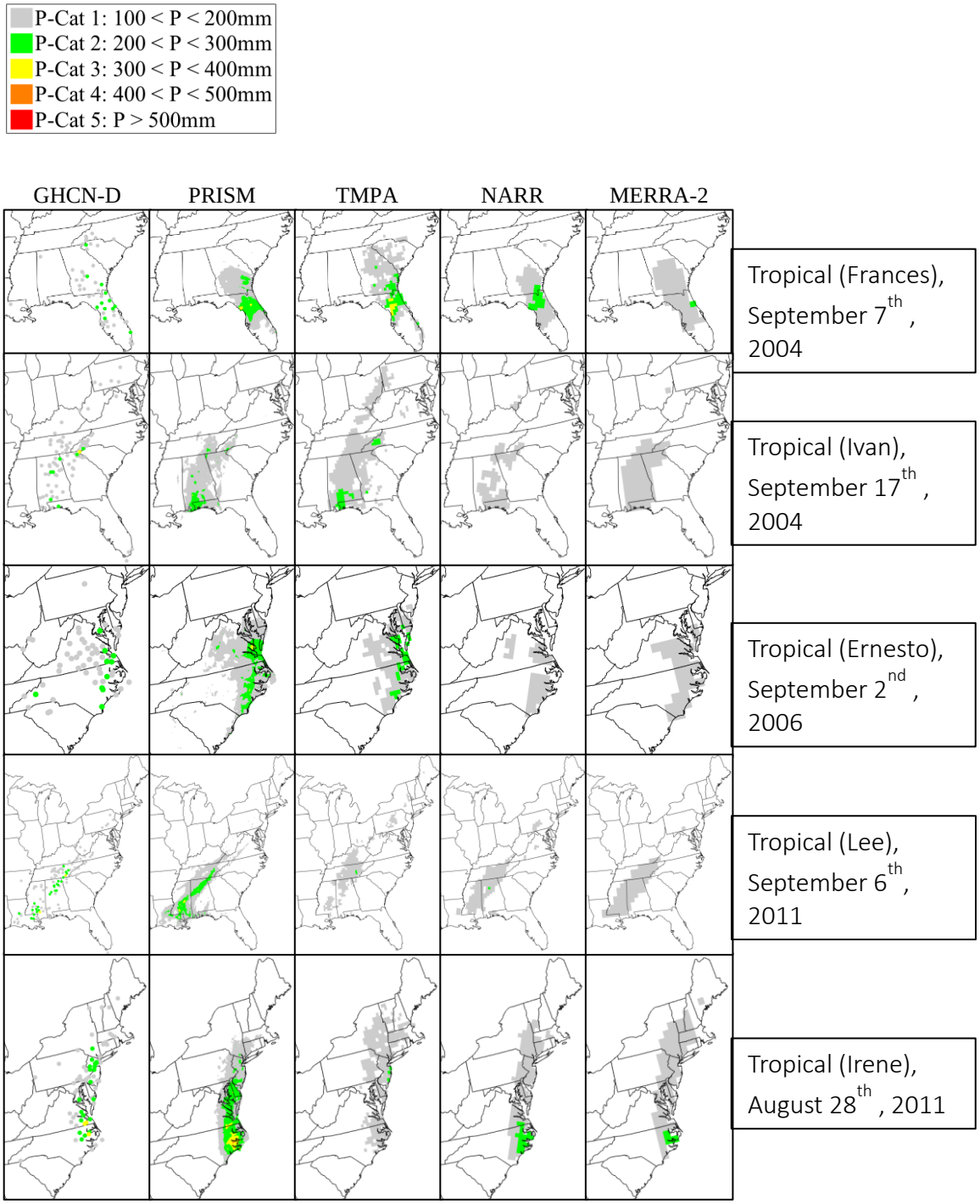

Figure S1.2 Comparison of P-Cat values for five individual tropical cyclones. P-Cat values are for the three day total ending on the day indicated on the right. The datasets are (from left to right) GHCN-D, PRISM, TMPA, NARR, and MERRA2.

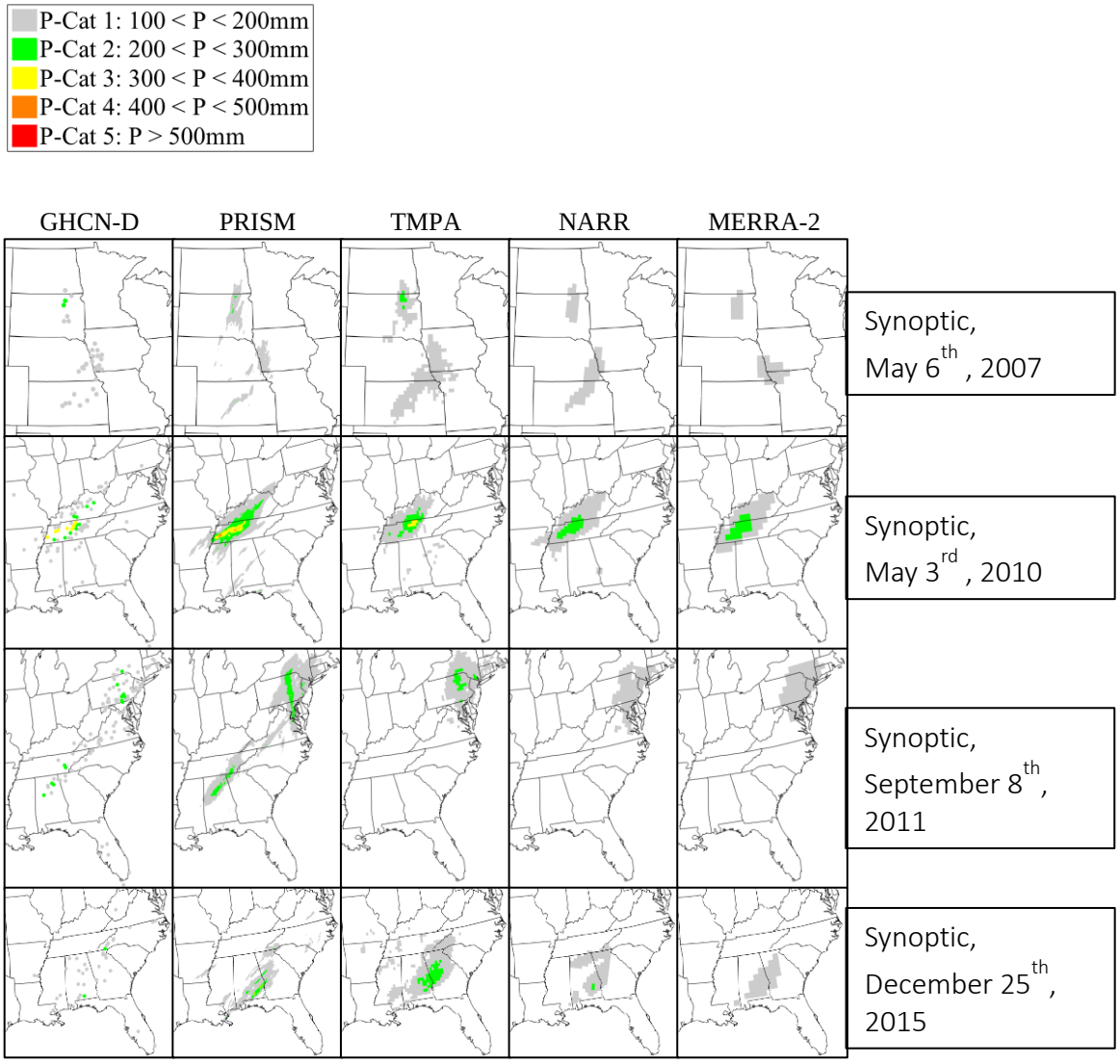

Figure S1.3 Same as for Figure S1.2 except for four synoptic scale mid-latitude cyclones.

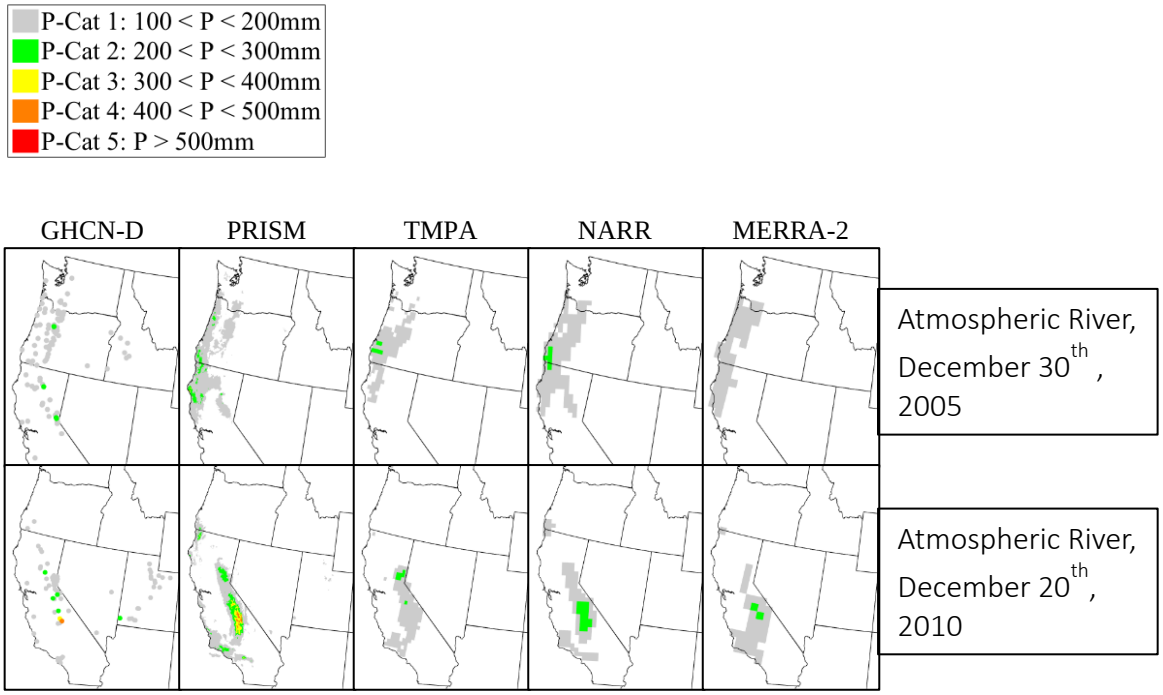

Figure S1.4 Same as for Figure S1.2 except for two atmospheric river events.

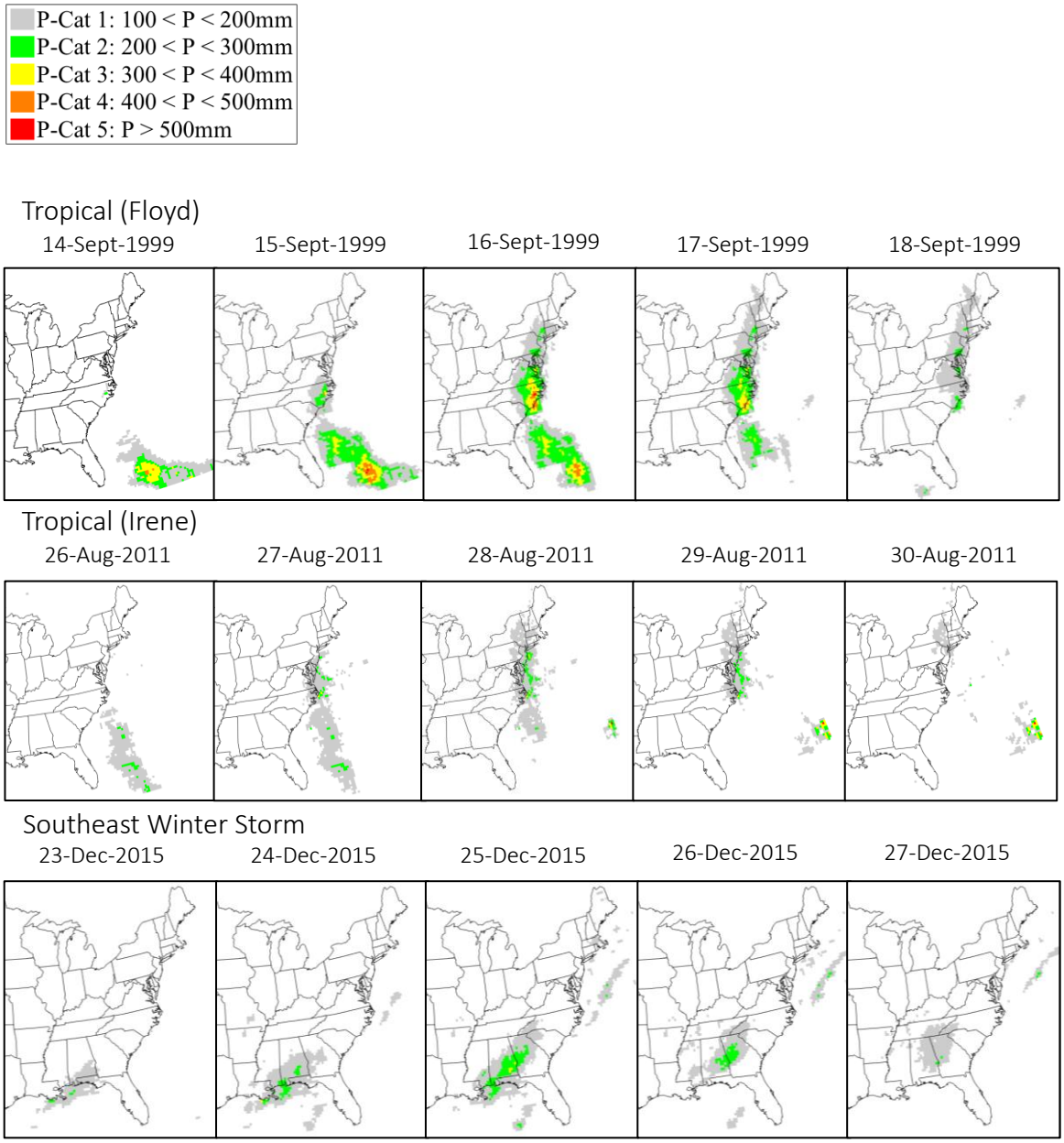

Figure S1.5 Maps depicting storm propagation across five days of three notable heavy rainfall events.

Appendix B: Supplementary Material for Chapter 3

Region	>90%				>95%				100%			
	DJF	MAM	JJA	SON	DJF	MAM	JJA	SON	DJF	MAM	JJA	SON
CONUS	3.161%	0.141%	0.031%	0.758%	0.522%	0.004%	0.031%	0.058%	0.003%	0	0.031%	0
Northwest	2.188%	0	0	1.606%	0	0	0	0.019%	0	0	0	0
Southwest	8.419%	0.065%	0.137%	2.173%	2.037%	0	0.137%	0.234%	0.014%	0	0.137%	0.001%
Great Plains North	0	0	0	0	0	0	0	0	0	0	0	0
Great Plains South	0	0	0	0	0	0	0	0	0	0	0	0
Midwest	0.003%	0.003%	0	0.294%	0	0	0	0.004%	0	0	0	0
Northeast	0	0	0	0	0	0	0	0	0	0	0	0
Southeast	6.777%	0.791%	0	0.523%	0.416%	0.025%	0	0.024%	0.	0	0	0

Table S2.1 The percentage of grid cells across the CONUS and within each NCA region that have an extreme precipitation fraction (or percent of linked AR extreme precipitation days relative to the total number of extreme precipitation days) of >90%, >95%, and 100% for the period of 1981–2016.

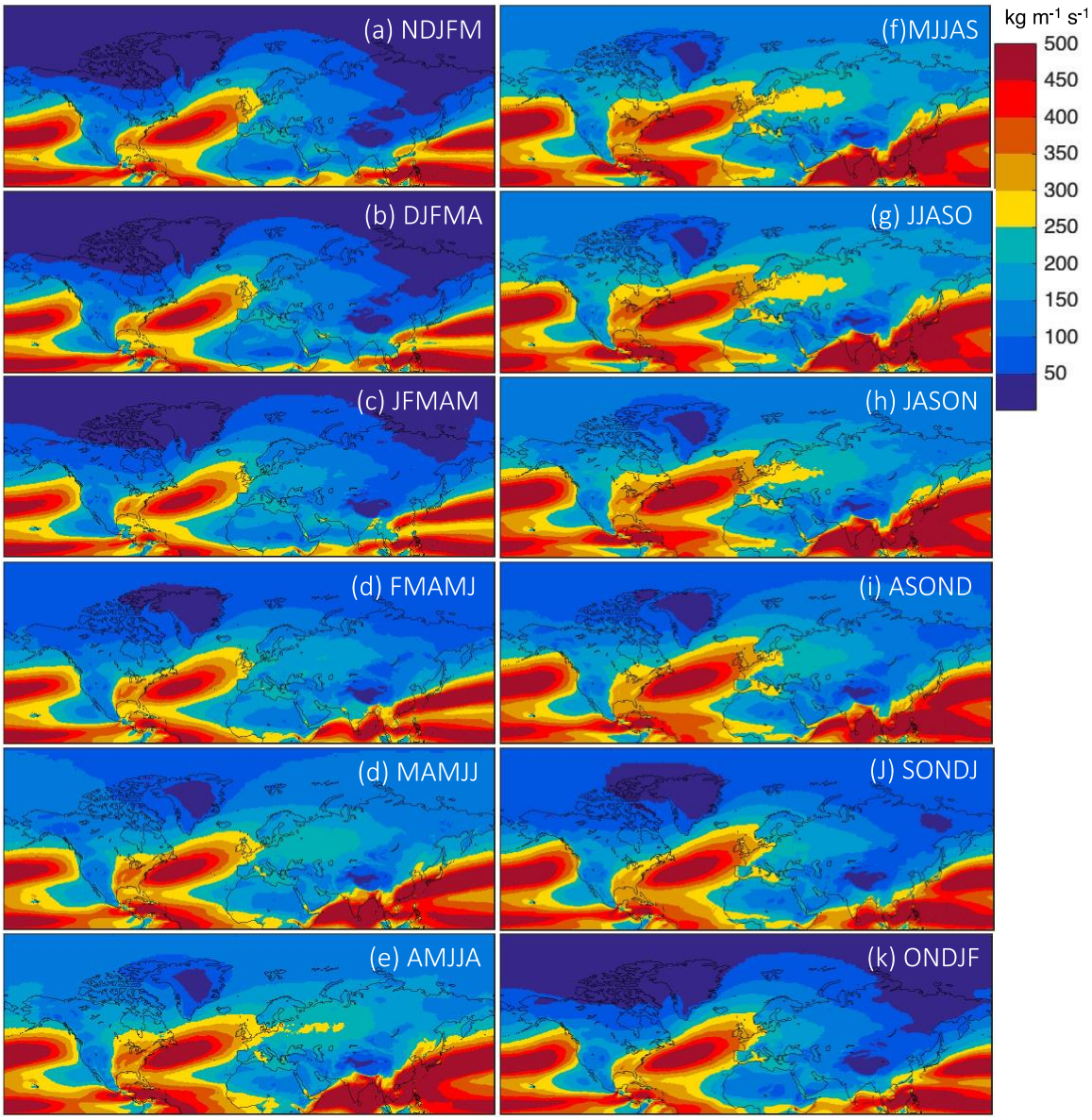

Figure S2.1 The 85th percentile of IVT magnitude (kg m^{-1} s^{-1}) at each grid cell for the period of 1981–2016. A total of 12 maps, for 12 overlapping 5-month seasons, are used to threshold daily IVT in the detection of ARs. The 85th percentile (and 100 kg m^{-1} s^{-1}, whichever is greater) is the lower limit for the multiple, sequentially higher IVT percentile thresholds (i.e., 85th - 95th) used for AR detection.

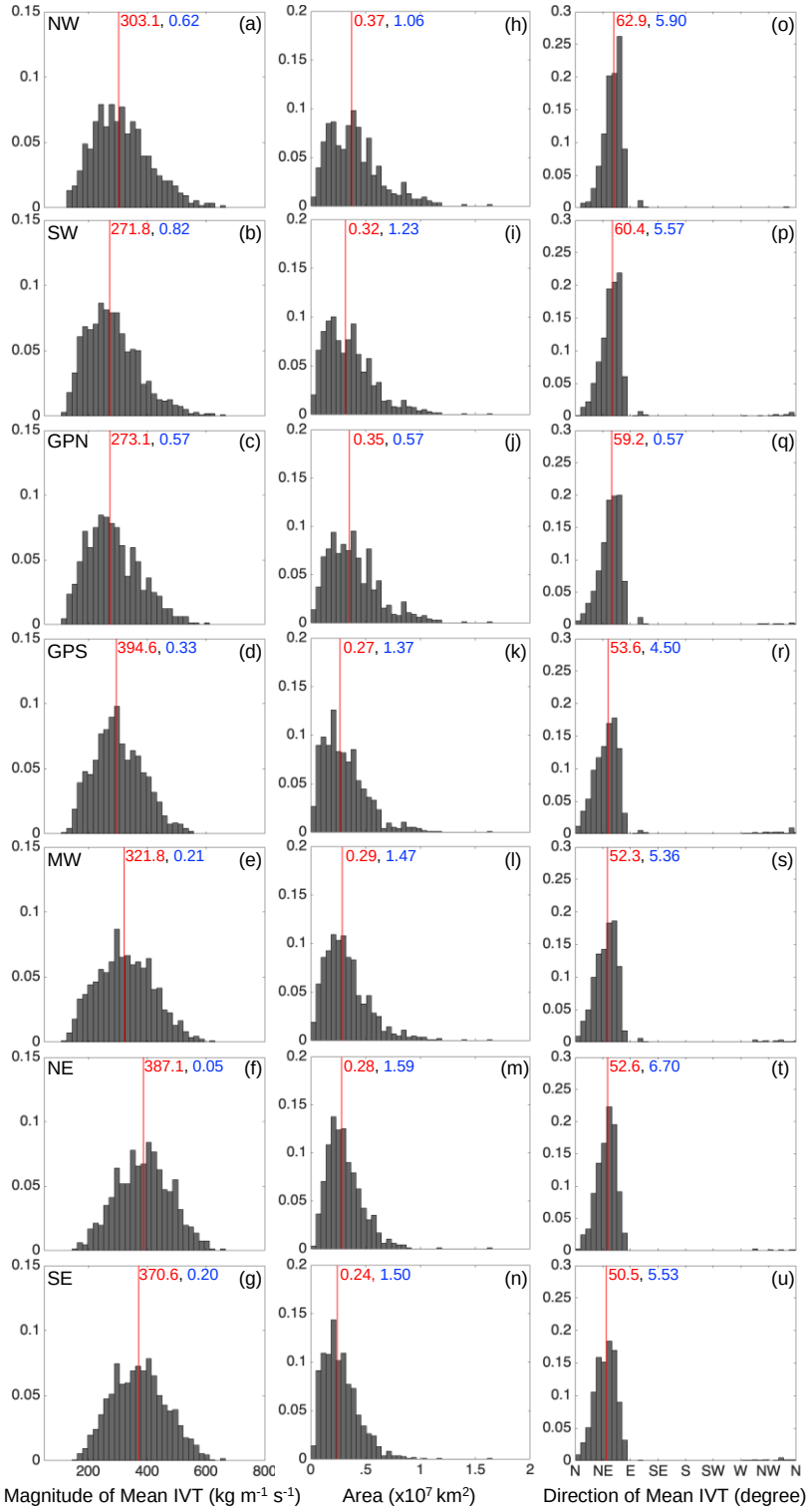

Figure S2.2 Histograms of basic characteristics of ARs detected during December,

January, and February between 1981–2016. In each panel, red lines indicate the median

while the value in blue represents skewness. Results are for the magnitude of mean IVT (kg m^{-1} s^{-1}; column 1); AR area (x10^7 km^2; column 2); and direction of mean IVT (degree; column 3) for each of the 7 NCA regions (rows).

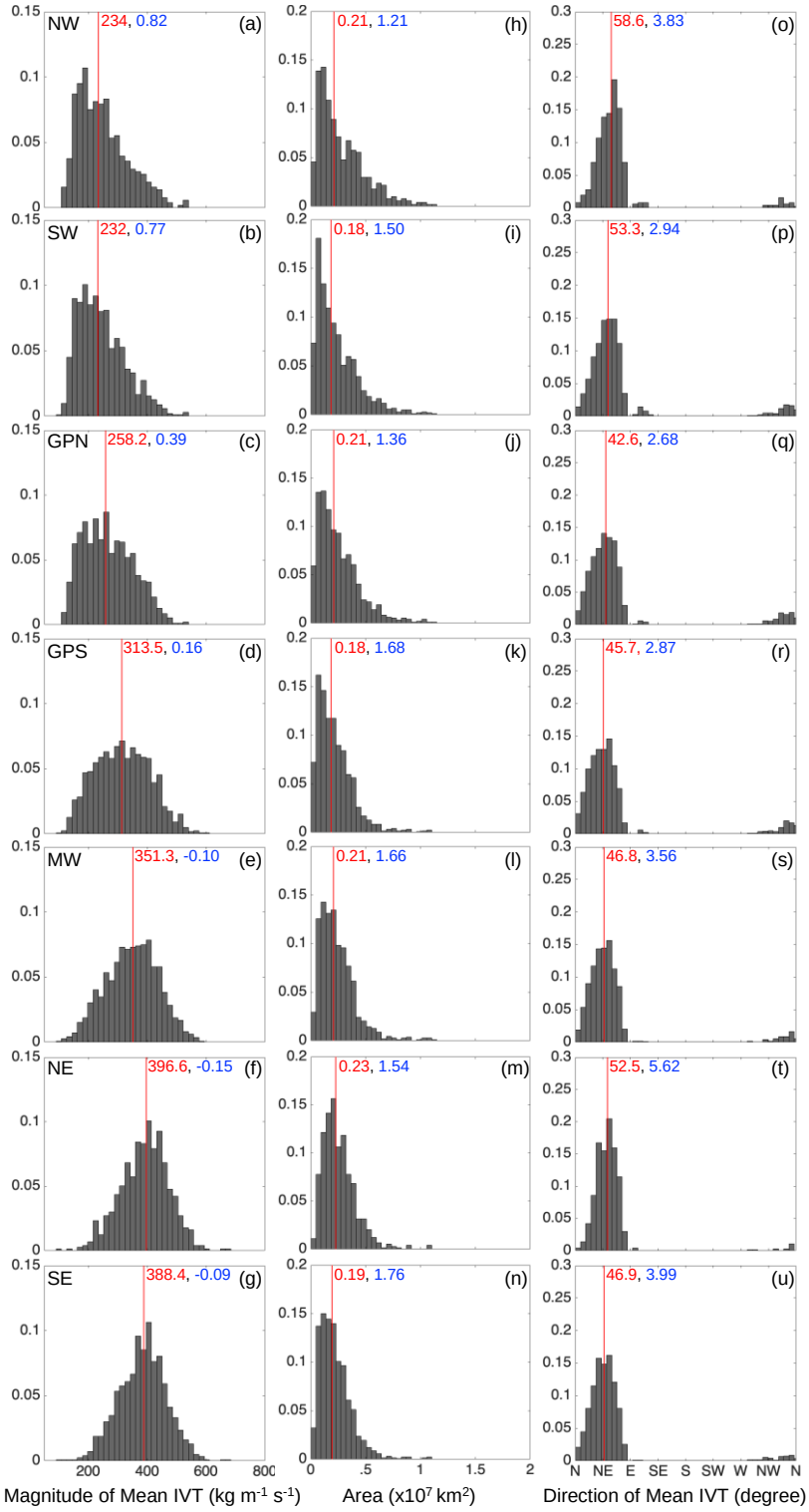

Figure S2.3 Same as in Figure S2.2 except results are for March, April, and May.

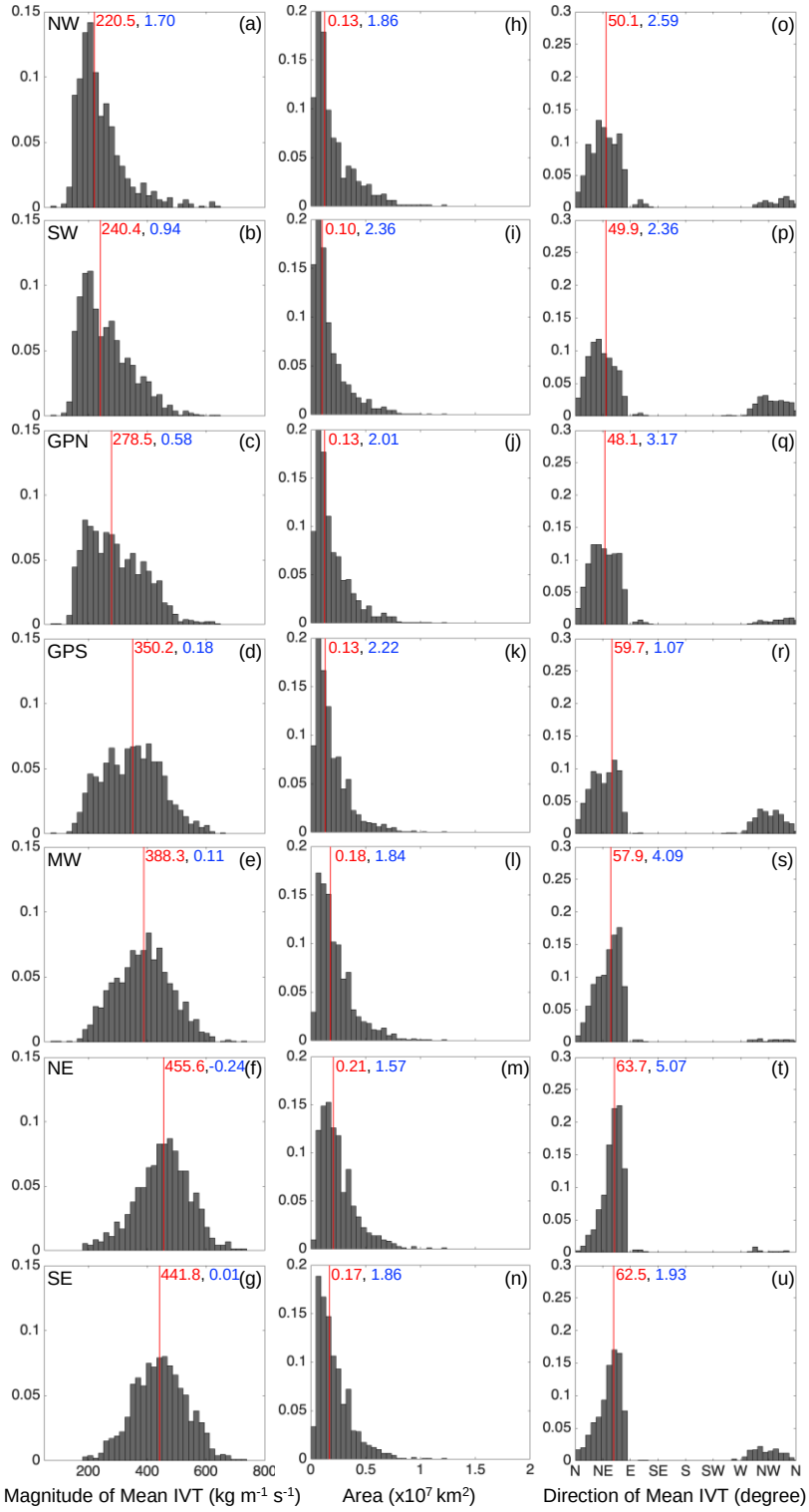

Figure S2.4 Same as in Figure S2.2 except results are for June, July, and August.

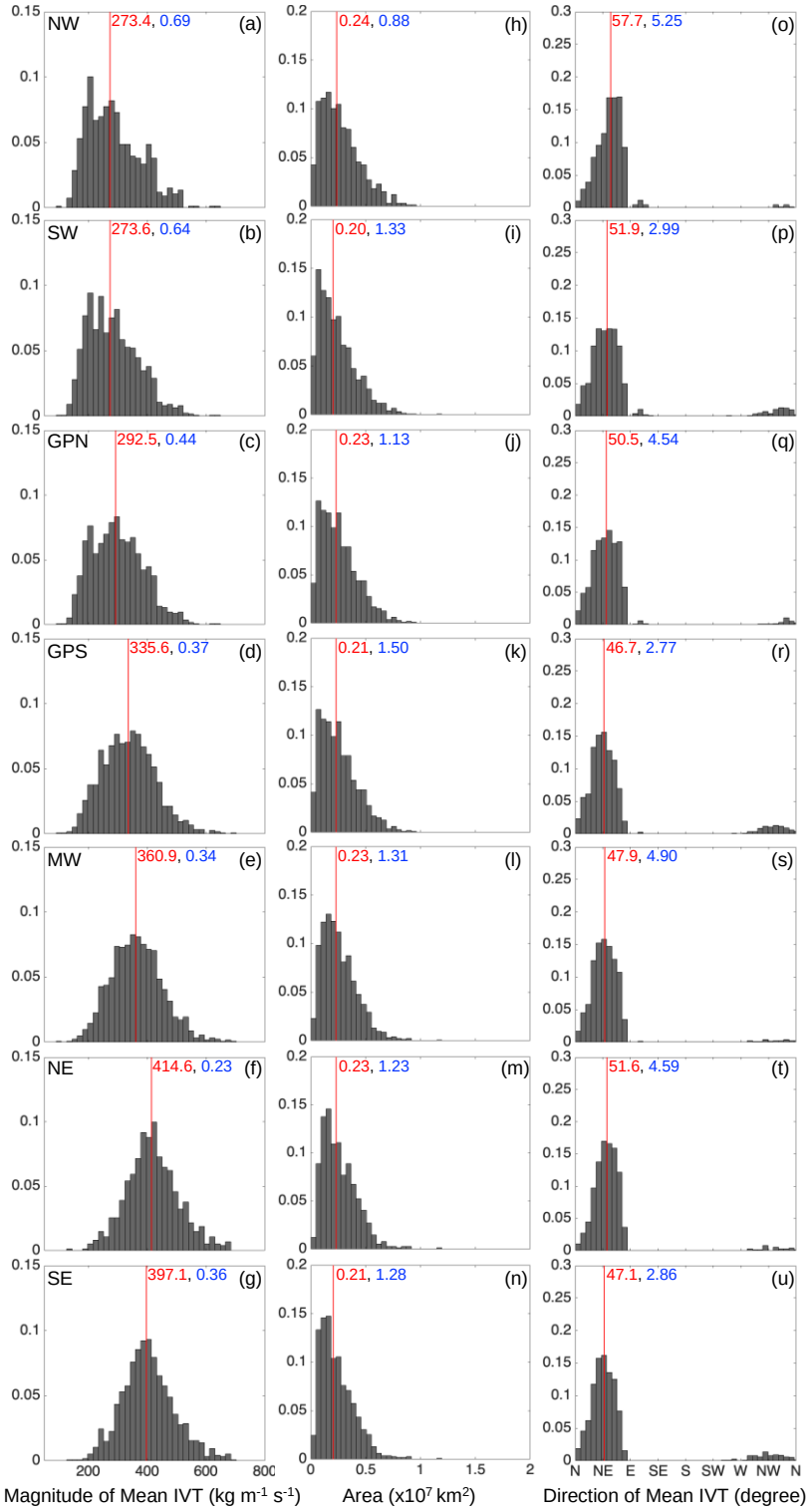

Figure S2.5 Same as in Figure S2.2 except results are for September, October, November.